THE UNIVERSITY *of* LIVERPOOL

Advanced Control of Variable Speed Wind Turbine based on Doubly-Fed Induction Generator

Thesis submitted in accordance with the
requirements of the University of Liverpool
for the degree of Doctor of Philosophy

in

Electrical Engineering and Electronics

by

Lei Wang, B.Sc.(Eng.), M.Sc.(Eng.)

September 2012

Advanced Control of Variable Speed Wind Turbine based on Doubly-Fed Induction Generator

by

Lei Wang

Acknowledgements

I would like to give my sincerely thanks to my supervisor, Dr. L. Jiang, for his help, inspiration, and encouragement. The research skill, writing skill and presenting skill he taught me will benefit me throughout my life. Without his consistent and illuminating instruction, my research work could not proceed to this stage.

I would like to show my gratitude to Professor Q.H. Wu, my second supervisor, for his kind guidance with his knowledge of power system.

I offer my regards and blessings to all of the members of Electrical Drives, Power and Control Research Group, the University of Liverpool, especially to Dr. W.H. Tang, Dr. H.L. Liao, Dr. D.Y. Shi, Mr. J. Chen, Mr. C.K. Zhang and Mr. L. Zhu. Special thanks also go to my friends, Alpha, Y. Dong, S. Lin and Y.Q. Pei, for their support and friendship. My thanks also go to the Department of Electrical Engineering and Electronics at the University of Liverpool, for providing the research facilities that made it possible for me to carry out this research.

Last but not least, my thanks go to my beloved family for their loving considerations and great confidence in me through these years.

Abstract

This thesis deals with the modeling, control and analysis of doubly fed induction generators (DFIG) based wind turbines (DFIG-WT). The DFIG-WT is one of the mostly employed wind power generation systems (WPGS), due to its merits including variable speed operation for achieving the maximum power conversion, smaller capacity requirement for power electronic devices, and full controllability of active and reactive powers of the DFIG.

The dynamic modeling of DFIG-WT has been carried out at first in Chapter 2, with the conventional vector control (VC) strategies for both rotor-side and grid-side converters. The vector control strategy works in a synchronous reference frame, aligned with the stator-flux vector, became very popular for control of the DFIG. Although the conventional VC strategy is simple and reliable, it is not capable of providing a satisfactory transient response for DFIG-WT under grid faults. As the VC is usually designed and optimized based on one operation point, thus the overall energy conversion efficiency cannot be maintained at the optimal point when the WPGS operation point moves away from that designed point due to the time-varying wind power inputs.

Compared with VC methods which are designed based on linear model obtained from one operation point, nonlinear control methods can provide consistent optimal performance across the operation envelope rather than at one operation point. To improve the asymptotical regulation provided by the VC, which can't provide satisfactory performance under voltage sags caused by grid faults or load disturbance of the grid, input-output feedback linearization control (IOFLC) has been applied to develop a fully decoupled controller of the active $\&$ reactive powers of the DFIG in Chapter 3. Furthermore, a cascade control strategy is proposed for power regulation

of DFIG-WT, which can provide better performance against the varying operation points and grid disturbance.

Moreover, to improve the overall energy conversion efficiency of the DFIG-WT, FLC-based maximum power point tracking (MPPT) has been investigated. The main objective of the FLC-based MPPT in Chapter 4 is to design a global optimal controller to deal with the time-varying operation points and nonlinear characteristic of the DFIG-WT. Modal analysis and simulation studies have been used to verify the effectiveness of the FLC-based MPPT, compared with the VC. The system mode trajectory, including the internal zero-dynamic of the FLC-MPPT are carefully examined in the face of varied operation ranges and parameter uncertainties.

In a realistic DFIG-WT, the parameter variability, the uncertain and time-varying wind power inputs are existed. To enhance the robustness of the controller, a nonlinear adaptive controller (NAC) via state and perturbation observer for feedback linearizable nonlinear systems is applied for MPPT control of DFIG-WT in Chapter 5. In the design of the controller, a perturbation term is defined to describe the combined effect of the system nonlinearities and uncertainties, and represented by introducing a fictitious state in the state equations. As follows, a state and perturbation observer is designed to estimate the system states and perturbation, leading to an adaptive output-feedback linearizing controller which uses the estimated perturbation to cancel system perturbations and the estimated states to implement a linear output feedback control law for the equivalent linear system. Case studies including with and without wind speed measurement are carried out and proved that the proposed NAC for MPPT of DFIG-WT can provide better robustness performance against the parameter uncertainties.

Simulation studies for demonstrating the performance of the proposed control methods in each chapter, are carried out based on MATLAB/SIMULINK.

Declaration

The author hereby declares that this thesis is a record of work carried out in the Department of Electrical Engineering and Electronics at the University of Liverpool during the period from October 2008 to September 2012. The thesis is original in content except where otherwise indicated.

Contents

List of Figures

List of Tables

Chapter 1

Introduction

1.1 Background

Wind power, as a clean and sustainable energy, has obtained highly concentrations during the past decade [1], [2]. Research and development of renewable energy has gained tremendous momentum in the past decade as the cost of conventional electrical power generation continuously escalate due to the limited fuel resources, and the general public becomes increasingly concerned of the environmental impacts caused by the thermal and nuclear generation. Among many technologies promising green power, the utilization of wind energy via wind power generation system (WPGS) is one of the most mature and well developed. Across the world, the total capacity of wind generation has already exceeded giga-watt (GW) rating and larger wind farms are constantly being planned and commissioned [3], [4], [5].

The main components of a WPGS includes the turbine rotor, gearbox, generator, transformer, and possible power electronics. The turbine rotor converts the fluctuating wind energy into mechanical energy, which is converted into electrical power through the generator, and then transferred into the grid through a transformer and transmission line. Wind turbines capture the power from the wind by means of aerodynamically designed blades and convert it to rotating mechanical power. The number of blades is normally three and the rotational speed decreases as the radius of the blade increases. For meag-watt range wind turbines the rotational speed will

be 10-15 rpm. The weight-efficient way to convert the low-speed, high-torque power to electrical power is to use a gearbox and a generator with standard speed. The gearbox adapts the low speed of the turbine rotor to the high speed of the generator. The gearbox may be not necessary for multi-pole generator systems.

The generator converts the mechanical power into electrical energy, which is fed into a grid through a power electronic converter, and a transformer with circuit breakers and electricity meters. The connection of wind turbines to the grid is possible at low voltage, medium voltage, high voltage, and even at the extra high voltage system since the transmittable power of an electricity system usually increases with increasing the voltage level. While most of the turbines are nowadays connected to the medium voltage system, large offshore wind farms are connected to the high and extra high voltage level.

Doubly fed induction generators (DFIG) based wind turbines (DFIG-WT), a typical employed WPGS, have be widely used to achieve the maximum power conversion, smaller capacity of power electronic devices and full controllability of active and reactive power of the DFIG [6], due to their characteristics such as varying speed operation. The stator circuit of the DFIG is connected to the grid directly, while the rotor circuit is fed via a back-to-back power converter. The back-to-back converter consists of two converters, i.e., rotor-side converter and grid-side converter, which are connected ”back-to-back”. Between the two converters a dc-link capacitor is placed, as energy storage, in order to keep the voltage variations (or ripple) in the dc-link small.

1.2 Challenges & Problems

1.2.1 Nonlinear dynamics of DFIG-WT

The DFIG-WT is a dynamic system with strong nonlinear coupled characteristics and time varying uncertain inputs. The aerodynamic of wind turbine introduces strong nonlinearities and uncertainties [28]. Objectives of the wind-turbine controller depend upon the operating area defined via wind speed [29]. For low wind speeds, it is more important to maximize wind power capture while it is recommend-

ed to limit power production and rotor speed above the rated wind speed to protect the mechanical part of the WPGS. The power regulation of the wind turbine is a highly nonlinear system as the plant, actuation and control objectives are all strong nonlinear [30].

As an induction machine, the DFIG is also a typical nonlinear system as induction motor, which has been used widely as a test benchmark for nonlinear control system design. With the time-varying and intermittent wind power input, DFIG-WT is required to operate at an operation envelope with a wide range rather than one operation point. Moreover, during voltage sags due to grid load disturbances or grid faults, DFIG-WT will operate far away from its normal operation point. During the grid fault period and post-fault period, terminal voltage normally dropped close to the ground and cause the strong dynamics in the stator and rotor currents, and such that stator-flux will not be remained as constant as well. This will destroy the condition of the mostly used VC schemes for DFIG-WTs and dynamic of the active and reactive power of the DFIG are still coupled during the transient period of stator-flux or stator-voltage. As all vector control schemes depend upon the assumptions of constant voltage and flux to realize asymptotical decoupling control of the active and the reactive power, it can expect that their performance will be degraded during voltage sags and grid faults. On the other side, unlike the vector control of induction motor in which the rotor flux is controlled directly, stator-flux of the DFIG normally is not one of the controlled variables and thus not controlled directly.

The control function within the vector control scheme has commonly been performed by using PI controllers. One challenge is how to tune the parameters of the PI loops to provide optimal performance around one special operation point and cope with the time-varying operation points. For examples, many results have been done to automatically tune the PI controller's parameters, such as using genetic algorithm [42] and particle swarm optimization [43]. Automatic tuning based on artificial intelligence and gain schedule technique have been proposed to provide optimal performance for a varying operation condition. Input/output linearization have been proposed to fully decoupling control of induction motor [50, 85]. When the wind turbine operates at varying speed to achieve the maximum wind power con-

version, rotor speed will travel between the sub-synchronous to super-synchronous speed and other state variables of the DFIG, including stator and rotor currents and the rotor voltages, are dynamic variables so as to inject different value of active power. However, because the system is highly nonlinear, it is difficult to find one set of parameters, which can provide a consistent optimal response when the operation point changes. Moreover, in some worst cases, unstable mode may exist because of one set of PI parameters [45]. Other linear control strategies, such as LQG, which are designed based a linearized model around a special operation point, may face difficulties to find approximate gains to maintain optimal efficiency for a wide range of operation points changing with the varying wind speed, and guaranteeing the overall system stability when the system operates from sub-synchronous mode to super-synchronous mode [35].

Compared with linear methods, which are designed based on a linear model obtained from one operation point, nonlinear control methods can provide consistent optimal performance across the operation envelope rather than at an operation point and have already attracted lots of research efforts, such as gain schedule control [31, 32], sliding mode control [14], multi-variables LQG control [33], feedback linearization control (FLC) which assuming exact knowledge of the power conversion coefficient of the wind turbine C_p [34] and nonlinear adaptive control with estimation of the input wind torque by assuming it as an unknown constant value [35]. Assume the exact knowledge of the wind-turbine power conversion C_p function, it is shown that FLC method outperforms gain schedule and LQG methods with less control efforts and better overall performance.

A fuzzy logic controller can overcome this problem by varying its parameters according to the operating point; however, it cannot guarantee an optimal response [46]. An adaptive controller based on estimation of the uncertain plant parameters, allowing the controller parameters for an optimal response to be adjusted to deal with account for changing plant dynamics. Thus so far, only a few applications of adaptive control applied to variable-speed wind turbines have appeared in literature. Adaptive control algorithms proposed in [47] uses a doubly fed induction generator to adjust the turbine speed. In [48] a Static Kramer drive lies between the rotor

circuit and the grid. Using this configuration the generator torque and hence the turbine speed is changed by adjusting the firing angle of the inverter. A similar scheme was used in [35], where the excitation voltage across the rotor circuit was also adjusted.

1.2.2 Uncertain wind power inputs

Variable speed operation of DFIG-WT operates under time-varying uncertain wind power input, due to time-varying wind speed. Besides the wind turbulence, tower shadow effect of the horizontal axis wind turbine will also cause periodical variation on the input wind power, even with constant average wind speed. Most works do not consider the time-varying characteristics of the wind power at the designing stage, while validate the effect of the controller to reject the time-varying wind power via simulation. The wind speed is assuming to be constant such that the input torque is treated as a constant. A few works are treating it as a time-varying input. Most adaptive control of WT assumes the input torque as an unknown constant or slow time-varying and updates it via an estimator, because there is not an effective method in the control filed to estimate the fast and time-varying unknown parameters and dynamics. Sliding mode methods treats the time-varying input as parts of the uncertainties [49].

1.2.3 Fault ride through requirement

With the penetration level of wind energy increased in the current power grid, fault ride through (FRT) capability has been introduced into most grid codes as one of the important requirements for the WPGS [15]. The FRT capability, or known as low voltage ride through (LVRT) capability, specifies that the WPGS must be connected to the power grid during a grid fault to provide active power control to the grid during and after the grid fault and to help re-establish the grid voltage after the clearance of the grid fault. The FRT capability is necessary in integrating large-scale wind power generations into the power networks, because it reduces the spinning reserve demands required for the intermittent wind power and impacts of voltage

and stability of the grid.

The FRT is of special interest to DFIG-WT since the stator of the DFIG is connected directly with the grid and is sensitive to voltage sags caused by grid faults or load disturbances. The voltage sags of the stator will result in a sharp increase of the stator-flux and over currents of the stator and the rotor windings due to the magnetic coupling between the stator and the rotor windings. These over currents, called inrush currents, may be raised up to three times of their rated values and will damage the rotor and stator windings. And the most serious consequence of such inrush currents is that they can lead to the breakdown of the rotor-side power electronic converter. The voltage sags will also yield the fluctuation of the DC-link voltage, which is controlled via the grid-side converter, and will in turn, affect the dynamic of the rotor-side converter since the DC voltage is required to be remained as constant for operation of the rotor-side converter.

Traditionally, the FRT capability of the DFIG-WT is achieved by the installing crowbar protection of the rotor-side converter [16–18]. However, this solution cannot avoid the disconnection of the wind turbine with the grid during the fault. A sudden loss of large-capacity wind power during the fault will introduce frequency and voltage control problems in the network. Moreover, short-circuit of the rotor of the DFIG converts the DFIG into a squirrel-cage induction generator and loss control over the power of the DFIG, which will consume more reactive power and worsen the voltage sag as the voltage regulation from the power network needs reactive power support during the fault clearing and after the fault period.

Other two methods of improving the FRT capability are hardware modification and designing/modifying of the control of the DFIG-WT [19–22]. There is a lots of efforts on investigating and improving of the LVRT of the DFIG-WT via improving and designing an advanced controller to limit the peak value of rotor inrush current and the fluctuation of the dc-link voltage [20–22]. However, most results reported are based on vector control schemes, which rely on the assumptions of a constant stator-flux and stator-voltage. Due to the relatively smaller value to the stator resistance compared with the mutual inductance L_s, stator resistance R_s is always supposed to be zero in the VC scheme. In fact, dynamic of the stator-flux is a poorly

damped system due to a very small R_s/L_s value. These assumptions are not valid during the voltage sags and grid fault conditions since the stator-flux has performed strong undamped transient dynamic [51]. Moreover, as in most work, stator-flux is not controlled and thus the performance of the DFIG-WT with VC will be degraded under grid faults. The VC based on the stator voltage shows similar characteristics. To improve the FRT capability, control of the dynamic of the stator variables, stator-flux and stator-voltage, should be considered at the designing stage of the controller.

1.2.4 Voltage and stability support of power networks

WPGSs with large capacity are required to support the operation of the power networks via providing similar control functionalities as conventional synchronous generators (SG), such as voltage control, frequency control and stability improvement [23, 24]. Control of the DFIG to make its behavior like an SG was proposed in [24–26], in which control blocks normally employed in the SG like automatic voltage regulator (AVR) and power system stabilizer (PSS) are applied to the DFIG, and a new control scheme called as flux magnitude-angle controller (FMAC) is obtained. In the FMAC, magnitude and angle to the rotor flux are employed as control variables for terminal voltage and active power, respectively. Compared with the SG, the DFIG has better controllability to achieve independent control of the terminal voltage and active power (or the provision of damping) because it has two independent control inputs, while the SG involves a compromise between the conflicting requirements of voltage control and the provision of damping as both AVR and PSS use the magnitude of the field voltage as the control variables (Note that the angle of voltage field cannot change as it is aligned with the rotor). However, all additional controllers are designed based on classical linear control theory, and their parameters are optimized based on one operation point. Based on the idea of the FMAC and solving the parameter tuning, a damping controller is designed based on a simple PI controller and tuned using bacterial foraging technique to enhance the damping of the oscillatory modes [27].

On the other side, because it is difficult to obtain the detailed nonlinear dynamics of a large-scale multi-machine power system, most of the current designs are

carried out based on a single-machine-infinite-bus (SMIB) system, and then verify the controller's performance in the multi-machine power systems via simulation studies. Interactions with the power networks require that the dynamic of the power networks must be considered during the design stage of the controller, *i.e.*, the design of the controllers did better be carried out in multi-machine-power-systems. Decentralised nonlinear control has been proposed for the improvement of transient stability of a power system, in which terminal voltage of the DFIG and slip speed are decoupled controlled via d-q components of the rotor voltage [36]. The design is based on a simplified third-order model of the DFIG with stator dynamics ignored, while the input prime wind power is assumed as constant.

1.3 Motivations

The performance of DFIG-WT depends heavily upon the controllers applied on the generator side and the wind turbine side. The DFIG-WT is usually controlled via a cascaded structure including an inner fast-loop for power regulation of the DFIG and an outer relative slow loop for the speed control of drive train. The reference of active power of the DFIG is determined based on the maximum energy conversion, which is defined as maximum power point tracking (MPPT), when wind speed is below the rated value; while constant reference is given when wind speed is above the rated value. The wind turbine also employs pitch angle control to regulate the extracted power from wind source by wind turbine for wind speed above the rated value, while pitch angle is fixed when wind speed below the rated value.

Main purposes of this thesis are to develop advanced control strategies for DFIG-WTs to improve the energy conversion efficiency and the transient dynamics of DFIG-WTs, by considering nonlinear dynamics, uncertain wind power inputs and grid faults. At first, modeling of a DFIG-WT and the conventional vector control have been reviewed and prepared for the following research. Then a fully decoupled power controller is proposed by using nonlinear control to improve the asymptotically decoupled characteristics provided by VCs. Thirdly, nonlinear control has been proposed for the Maximum Power Point Tracking (MPPT) of DFIG-WTs op-

erating below the rated wind speed. Both modal analysis and simulation studies have been carried out. Finally, to improve the robustness of the nonlinear control and to compensate the time-varying and uncertain wind power inputs, a nonlinear adaptive control based on perturbation estimation has been studied for the MPPT of DFIG-WTs.

1.4 Thesis Outline

- Chapter 2 presents the modeling of a doubly fed induction generator based variable-speed wind turbine, including dynamic model of wind turbine, drive train, DFIG and power electrical converters. For the controller design, the dynamic model of DFIG is obtained under the two-phase d-q rotating reference frame by applying Clarke and Park's transformations of the original three-phase natural reference frame.

- Chapter 3 proposes a nonlinear power control for DFIG. The conventional used power control strategy, vector control, is recalled at first. As vector control can only achieve the asymptotical regulation of the active/reactive powers of the DFIG, a fully decoupled nonlinear power control based on feedback linearization control is designed for the direct power control of the DFIG. Moreover, a cascade two stages nonlinear controller, which consists of an outer loop to provide current reference for the rotor current from the stator active and reactive powers, and an inner loop applies the input/output feedback linearization control for the current regulation.

- In Chapter 4, the nonlinear control based maximum power point tracking is studied. The operation regions of wind turbine are introduced at first, where MPPT control normally works in the range between the cut-in and rated wind speed. Both VC and FLC are applied for MPPT control under time-varying wind speeds, to achieve the maximum power extraction from the wind power. Modal analysis is used to analysis the dynamics of DFIG-WT provided by VC and FLC respectively, which shows that the FLC can provide consistent

dynamics with time-varying wind power inputs.

- Chapter 5 investigates the nonlinear adaptive control for DFIG-WT in order to deal with the parameter uncertainties, uncertain wind power inputs and improve the robustness of the nonlinear controller proposed in Chapter 4. The proposed adaptive controller designs a perturbation observer to estimate the real time perturbation and uses it to compensate the real uncertainties and disturbances. The design includes two cases: with and without wind speed measurement are carried out, followed by simulation studies.

- Chapter 6 presents conclusions and possible future works.

Chapter 2

Models of a DFIG based Variable Speed Wind Turbine

This chapter describes models of a wind power generation system equipped with doubly fed induction generator for variable speed wind turbine. Different typical configurations of WPGS are reviewed at first. The aerodynamic of wind turbine, drive train, generator(DFIG), and power electrical converters are investigated respectively. Detailed models of the DFIG based on different reference frames are given.

2.1 Introduction

Most modern WPGSs use horizontal axis design, three blades and upwind wind turbines. The larger WTs tend to operate at variable speed whereas smaller, simpler turbines are of fixed speed. For a fixed-speed wind turbine, the turbulence of the wind results in power variations, and thus affect the power quality of the grid. As in a variable-speed wind turbine, the generator is controlled by power electronic equipments, which makes it possible to control the rotor speed to maximize the energy conversion efficiency. In this way, the power fluctuations caused by wind variations can be absorbed by changing the rotor speed. Thus power variation originating from the wind variations and the stress of the drive train can be reduced. Hence, the

power quality impact caused by the wind turbine can be improved, compared to a fixed-speed turbine.

Fixed-speed wind turbines

This type of turbines are also called Type A turbine. Fixed-speed wind turbines are electrically fairly simple devices consisting of a WT rotor, a low-speed shaft, a gearbox, a high-speed shaft and an induction (or called as asynchronous) generator. From the electrical system viewpoint, they are perhaps best considered as large fan drives with torque applied to the low-speed shaft from the wind flow. Figure 2.1 illustrates the configuration of a fixed-speed wind turbine [37]. It consists of a squirrel-cage induction generator (SCIG) coupled to the power system through a turbine transformer. The generator operating slip changes slightly as the operating power level changes and the rotational speed is therefore not entirely constant. Because the operating slip variation is generally less than 1 %, this type of WPGS is normally referred to as fixed speed.

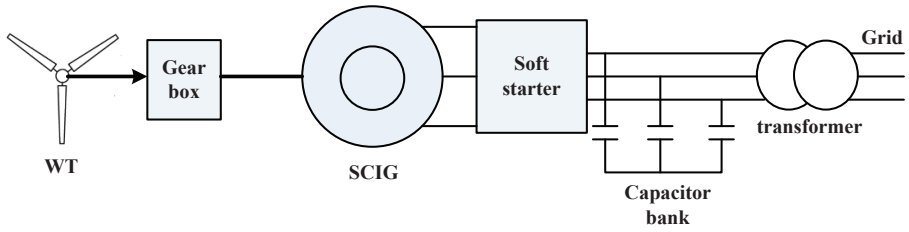

Figure 2.1: Schematic diagram of a fixed-speed wind turbine

Squirrel-cage induction machines consume reactive power and so it is conventional to provide factor correction capacitors for each wind turbine. The function of the soft-starter unit is to build up the magnetic flux slowly and thus minimize transient currents during energization of the generator. Meanwhile, by applying the network voltage slowly to the generator, once energized, it brings the drive train slowly to its operating rotational speed.

Variable speed wind turbine

During the past few years, variable-speed wind turbines have become the dominant type among the installed wind turbines. Variable-speed wind turbines are designed to achieve maximum aerodynamic efficiency over a wide range of wind speeds. With a variable-speed operation, it has become possible continuously to adapt (accelerate or decelerate) the rotational speed ω_r of the wind turbine to the wind speed V_{wind}. Thus, the tip speed ratio λ can be controlled at a predefined optimal value that corresponds to the maximum power coefficient. Contrary to a fixed-speed system, the variations in wind are absorbed by changes in the generator speed. The electrical system of a variable-speed wind turbine is more complicated than that of a fixed-speed wind turbine. It is typically equipped with an induction or synchronous generator and connected to the grid through power converters. The power converters control the generator speed; that is, the power fluctuations caused by wind variations are absorbed mainly by changes in the rotor speed of generator and consequently in the rotor speed of wind turbine. The advantages of variable-speed wind turbines are an increased energy capturing efficiency, improved power quality and reduced mechanical stress on the wind turbine. The disadvantages are losses in power electronics converters, the use of more components and the increased cost of equipment and maintenance because of the power electronics. The introduction of variable-speed wind-turbine types increases the number of applicable generator types and also introduces several degrees of freedom in the combination of generator typed and power converter type [38].

Most common used variable speed wind turbine configurations are listed as follows.

a Limited variable speed (Type B)

b Variable speed with partial scale frequency converter (Type C)

c Variable speed with full scale frequency converter (Type D)

Figure 2.2 shows the schematic diagram of a type B wind turbine. This configuration corresponds to the limited variable speed wind turbine with a variable generator rotor resistance. It uses a wound rotor induction generator (WRIG) and has been

used by the Danish manufacturer Vestas since mid 1990s. The generator is directly connected to the grid. A capacitor bank performs the reactive power compensation. A smoother grid connection is achieved by using a soft-starter. The unique feature of this concept is that it has a variable additional rotor resistance, which can be changed by an optimally controlled converter mounted on the rotor shaft. Thus, the total rotor resistance is controllable. This optical coupling eliminates the need for costly slip rings that need brushes and maintenance.

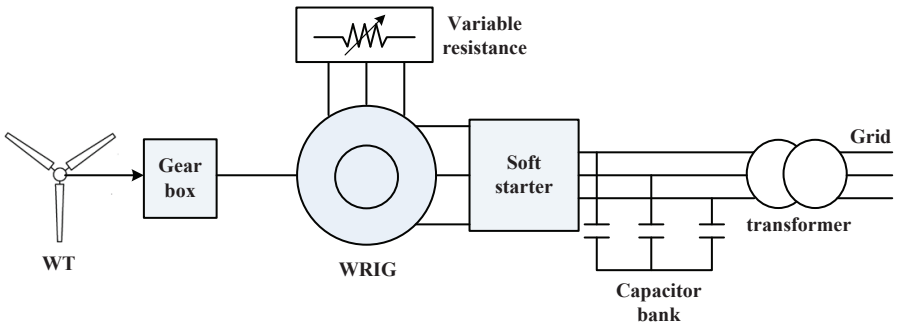

Figure 2.2: Schematic diagram of Type B wind turbine

The rotor resistance can be changed and thus the slip is controlled to regulate the power output of the WPGS. The range of the speed control depends on the size of the variable rotor resistance. Typically, the speed range is from 0 to 10 % above synchronous speed. Wallace and Oliver (1998) describe an alternative concept by using passive components instead of a power electronic converter, which can achieves a 10 % slip range.

For type C wind turbine, the schematic diagram is shown in Figure 2.3. This configuration, known as DFIG-WT, corresponds to the limited variable speed wind turbine with a DFIG and partial scale frequency converter (rated at approximately 30 % of the generator capacity) on the rotor circuit. The partial scale frequency converter performs the reactive power compensation and the smoother grid connection. It has a wider range of dynamic speed control compared with that of type B wind turbine, depending on the size of the frequency converter. Typically, the speed range comprises -40 % to $+30$ % of synchronous speed. The smaller frequency converter

makes this concept attractive from an economical point of view. Compared with type B, its main drawbacks are the use of slip rings and protection of the converters in the case of grid faults.

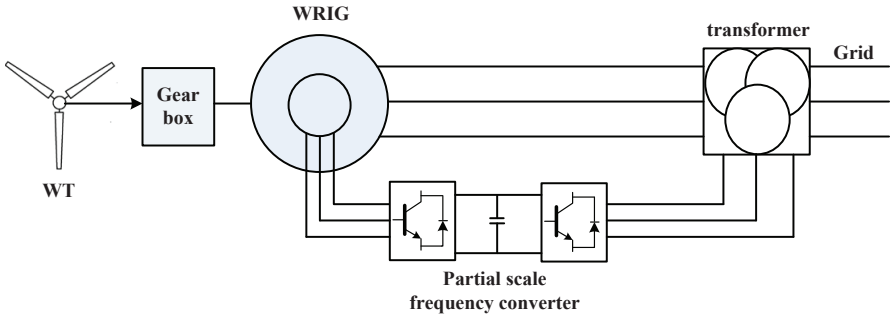

Figure 2.3: Schematic diagram of Type C wind turbine

The type D wind turbine corresponds to a fully variable speed wind turbine, with the generator connected to the grid through a full-scale frequency converter. The grid-side frequency converter performs the reactive power compensation and the smoother grid connection. The generator can be excited electrically (WRSG/WRIG) or by a permanent magnet (PMSG). Some fully variable-speed wind turbine systems have no gearbox. In these cases, a direct driven multi pole generator with a large diameter is used. The wind turbine companies Enercon, Made and Lagerwey are examples of manufacturers using this configuration.

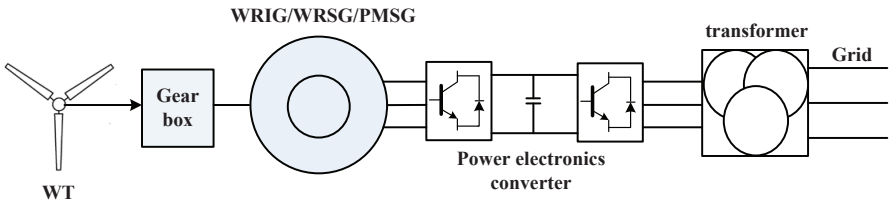

Figure 2.4: Schematic diagram of Type D wind turbine

2.2 Aerodynamics of Wind Turbines & Drive Train Model

Wind turbines produce electricity by converting the mechanical power of the wind to drive an electrical generator. Wind passes over the blades, generating lift and exerting a turning force. The rotating blades turn a shaft inside the nacelle, which goes into a gearbox. The gearbox increases the rotational speed to an appropriate value for the generator, which uses magnetic fields to convert the mechanical energy into electrical energy.

The power contained in the wind is given by the kinetic energy of the flowing air mass per unit time [39]. That is

$$P_{air} = \frac{1}{2}\rho\pi R^2 V_{wind}^3 \tag{2.2.1}$$

where P_{air} is the power contained in wind (in W), ρ is the air density (1.225 kg/m^2 at 15 degree and normal pressure), R is the blade length (in m), and V_{wind} is the wind velocity (in m/s) without rotor interference, i.e., ideally locating at infinite distance from the rotor.

The power captured by the wind turbine P_m is given by the power conversion coefficient

$$C_p = \frac{P_m}{P_{air}} \tag{2.2.2}$$

$$P_m = P_{air} \times C_p = \frac{1}{2}C_p\rho\pi R^2 V_{wind}^3 \tag{2.2.3}$$

where C_p is the power conversion coefficient.

A maximum value of C_p is defined by the Betz limit, which states that a turbine can never extract more than 0.593 of the power from an air stream. In reality, wind turbine have C_p values in the range 0.25-0.45.

For a given wind turbine, the coefficient C_p is dependent upon the aerodynamic characteristic of the wind turbine, and a complex nonlinear function of the blade tip speed ratio $\lambda = \frac{\omega_r R}{V_{wind}}$ (where ω_r is the angular speed of the rotor) and the blade pitch angle β. Generally, C_p can be obtained experimentally by carrying out wind tunnel tests and measuring the real output of the wind turbine under different wind speeds

and pitch angles. Based on experimental results, curve fitting technique can be used to obtain the formula of C_p. Curve fitting was performed to obtain the mathematical representation of the C_p curves used in the model: [40]:

$$C_p(\beta, \lambda) = \sum_{i=0}^{4} \sum_{j=0}^{4} \alpha_{i,j} \beta^i \lambda^j \tag{2.2.4}$$

where the coefficient $\alpha_{i,j}$ are given in Table 2.1.

Note that C_p is a nonlinear formulation of λ and β and it is not very accurate for very low and very big wind speed. Moreover, C_p's value will vary with changes of the shape of the blade caused by ageing and ices mounted on the blade.

Model of Drive Train

The mechanical representation of the entire wind turbine is complex. The power transmission train is constituted by the blades linked to the hub, coupled to the slow shaft, which is linked to the gearbox, which multiplies the rotational speed of the fast shaft connected to the generator.

The mechanical elements of a wind turbine and the forces suffered or transmitted through its components are very numerous. It is therefore necessary to choose the dynamics to represent and the typical values of their characteristic parameters. The first is the resonant frequency of the power train. For the purpose of the control design and simulation, representing the fundamental resonance frequency of the drive train is sufficient and a two-mass model, can then be used to represent the dynamic of the drive train. The second order resonance frequency is much higher and its magnitude is lower and thus can be ignored. The following two types of drive train models of the WPGS are usually available in the power system analysis, as shown in Figure 2.5.

In Figure 2.5(a), the two-mass model of drive train can be described by: [41]

$$\begin{cases} 2H_t \dfrac{d\omega_t}{dt} = T_m - D_t\omega_t - D_{tg}(\omega_t - \omega_r) - T_{tg} \\ 2H_g \dfrac{d\omega_r}{dt} = T_{tg} + D_{tg}(\omega_t - \omega_r) - D_g\omega_r - T_e \\ \dfrac{dT_{tg}}{dt} = K_{tg}(\omega_t - \omega_r) \end{cases} \tag{2.2.5}$$

Table 2.1: C_p coefficients $\alpha_{i,j}$

i	j	$\alpha_{i,j}$
4	4	4.9686e-010
4	3	-7.1535e-008
4	2	1.6167e-006
4	1	-9.4839e-006
4	0	1.4787e-005
3	4	-8.9194e-008
3	3	5.9924e-006
3	2	-1.0479e-004
3	1	5.7051e-004
3	0	-8.6018e-004
2	4	2.7937e-006
2	3	-1.4855e-004
2	2	2.1495e-003
2	1	-1.0996e-002
2	0	1.5727e-002
1	4	-2.3895e-005
1	3	1.0683e-003
1	2	-1.3934e-002
1	1	6.0405e-002
1	0	-6.7606e-002
0	4	1.1524e-005
0	3	-1.3365e-004
0	2	-1.2406e-002
0	1	2.1808e-001
0	0	-4.1909e-001

where ω_t and ω_r are the turbine and generator rotor speed, respectively; T_m and T_e are the mechanical torque applied to the turbine and the electrical torque of the generator, respectively; T_{tg} is an internal torque of the model; H_t and H_g are the inertia constants of the turbine and the generator, respectively; D_t and D_g are the damping coefficients of the turbine and the generator, respectively; D_{tg} is the damping coefficient of the flexible coupling between the two masses; K_{tg} is the shaft stiffness.

To simplify the analysis, the drive train system can also be modeled as a single lumped-mass system with a lumped inertia constant H_m as in Figure 2.5(b):

$$H_m = H_t + H_g \tag{2.2.6}$$

Therefore, one-mass model of drive trains is given by

$$2H_m \frac{d\omega_r}{dt} = T_m - T_e - D_m\omega_r \tag{2.2.7}$$

where D_m is the damping of the lumped-mass system.

2.3 Dynamic Model of DFIG

Nowadays doubly fed induction machine has been widely used in WPGS. These types of machines can be used resolutely as a generator or a motor. Though demands as motor is less because of its mechanical wear at the slip rings but they have gained their prominence for generator application in wind and hydro power plant because of its obvious adoptability capacity and nature of controllability of power. In this section, detailed model of DFIG has been given.

2.3.1 State space model in the a-b-c natural frame

The DFIM is provided with laminated stator and rotor cores with uniform slots in which three-phase winding are placed as shown in Figure 2.6. Usually, the rotor winding is connected to copper slip-rings. Brushes on the stator collect the rotor currents from the rotor-side static power converter. For the time being, the resistances

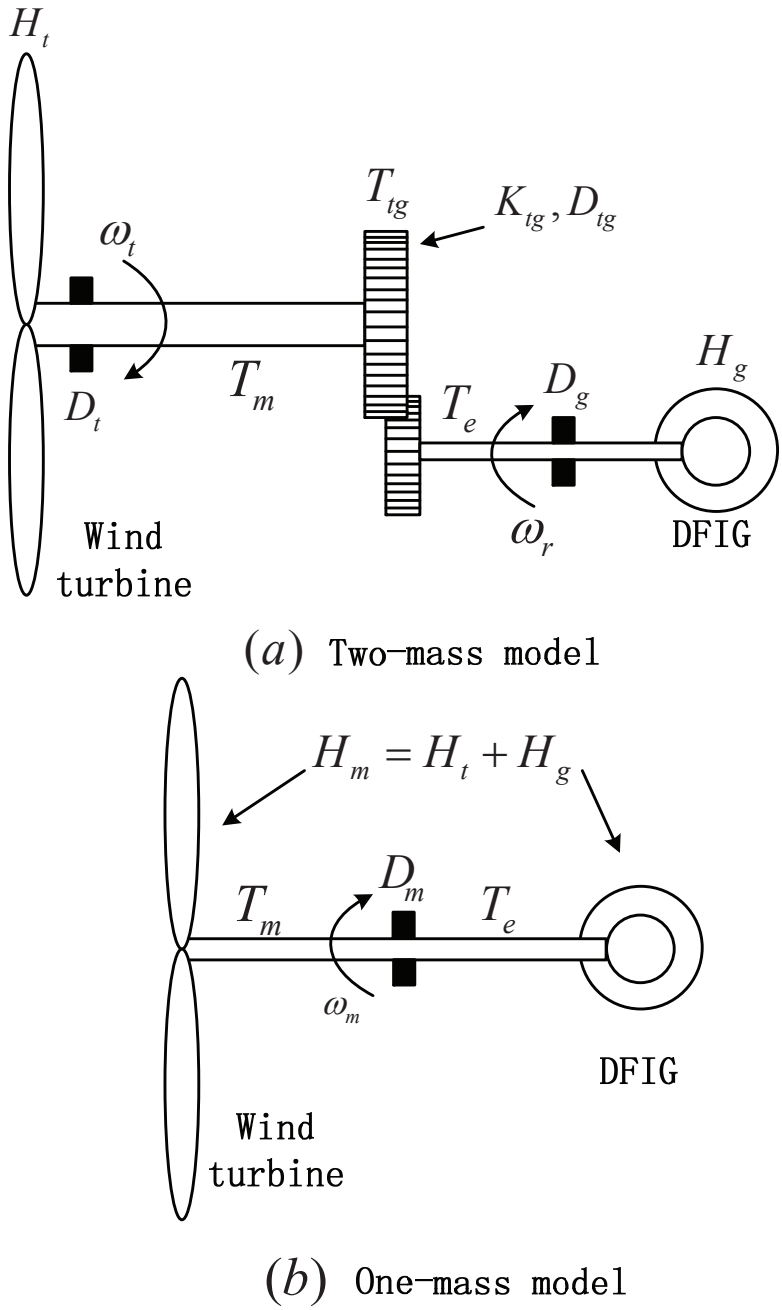

Figure 2.5: Drive train models of wind power generation systems

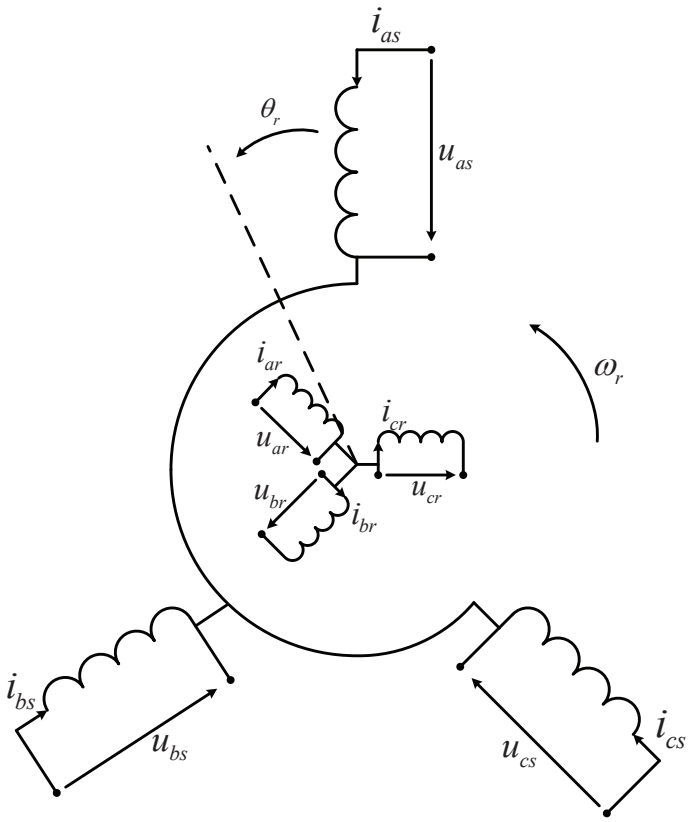

Figure 2.6: DFIM phase circuits

of slip-ring-brush system are lumped into rotor phase resistances, and the converter is replaced by an ideal controllable voltage source. The three-phase model of a DFIG can be described as:

$$\begin{cases} u_{as} = \dfrac{d\psi_{as}}{dt} + i_{as}R_s \\ u_{bs} = \dfrac{d\psi_{bs}}{dt} + i_{bs}R_s \\ u_{cs} = \dfrac{d\psi_{cs}}{dt} + i_{cs}R_s \end{cases} \tag{2.3.1}$$

$$\begin{cases} u_{ar} = \dfrac{d\psi_{ar}}{dt} + i_{ar}R_r \\ u_{br} = \dfrac{d\psi_{br}}{dt} + i_{br}R_r \\ u_{cr} = \dfrac{d\psi_{cr}}{dt} + i_{cr}R_r \end{cases} \tag{2.3.2}$$

where i_{as}, i_{bs}, i_{cs} are the three-phase stator currents; i_{ar}, i_{br}, i_{cr} are the three-phase rotor currents; u_{as}, u_{bs}, u_{cs} are the three-phase stator voltages; u_{ar}, u_{br}, u_{cr} are the three-phase rotor voltages; ψ_{as}, ψ_{bs}, ψ_{cs} are the three-phase stator flux linkages; ψ_{ar}, ψ_{br}, ψ_{cr} are the three-phase rotor flux linkages; R_s and R_r are stator and rotor resistances. Note that, the stator equations are represented in the stator natural frame, and the rotor equations are described in the rotor natural frame.

2.3.2 Clarke transformation

Considering a symmetrical three phase induction machine with stationary a-phase, b-phase and c-phase axes are placed at 120° angle to each other, as shown in Figure 2.7. The main aim of a Clarke transformation is to transform the three-phase stationary frame variables into a two-phase stationary frame variables α-β ,and vice versa.

Any three-phase voltage or current x in a-b-c components can be converted into α-β components via Clarke transformation and can be represented in the matrix form as

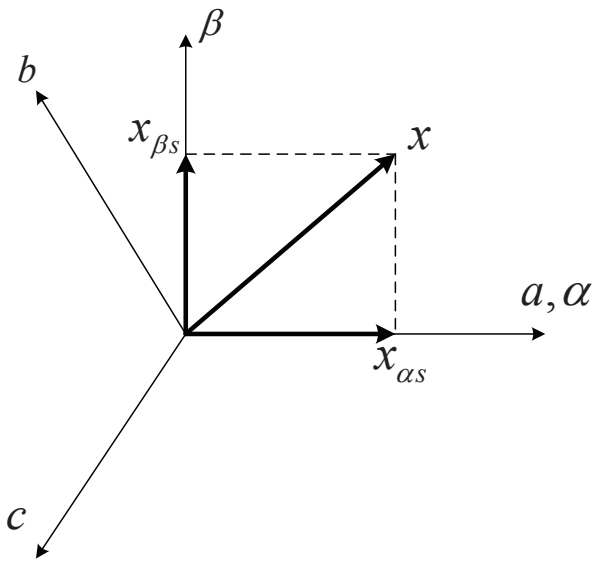

Figure 2.7: a-b-c to α-β axes transformation of stationary frame

$$\begin{bmatrix} x_\alpha \\ x_\beta \\ x_0 \end{bmatrix} = T_C \begin{bmatrix} x_a \\ x_b \\ x_c \end{bmatrix} \tag{2.3.3}$$

where T_C is the transformation matrix of Clarke transformation,

$$T_C = \frac{2}{3} \begin{bmatrix} 0 & -\frac{1}{2} & -\frac{1}{2} \\ 0 & \frac{\sqrt{3}}{2} & -\frac{\sqrt{3}}{2} \\ \frac{1}{2} & \frac{1}{2} & \frac{1}{2} \end{bmatrix} \tag{2.3.4}$$

x_0 is the zero sequence component, which equals to zero for symmetrical three-phase variable. For example, the reference transformation of stator and rotor currents are described as follows, and the reference frames can be seen in Figure 2.7.

$$\begin{bmatrix} i_{\alpha s} \\ i_{\beta s} \\ i_{0s} \end{bmatrix} = T_C \begin{bmatrix} i_{as} \\ i_{bs} \\ i_{cs} \end{bmatrix} \tag{2.3.5}$$

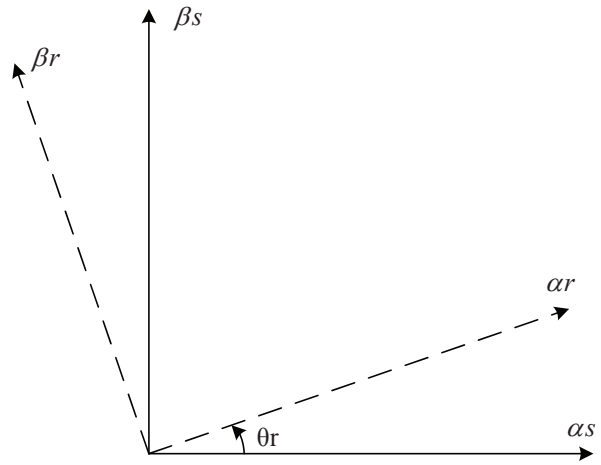

Figure 2.8: Transformation between stationary reference frames for stator and rotor variables

$$\begin{bmatrix} i_{\alpha r} \\ i_{\beta r} \\ i_{0r} \end{bmatrix} = T_C \begin{bmatrix} i_{ar} \\ i_{br} \\ i_{cr} \end{bmatrix} \tag{2.3.6}$$

where i_{0s} and i_{0r} are the zero sequence components of stator and rotor current, respectively.

The rotor variables represented in the rotor stationary reference frame can be referred to the stator stationary reference frame by a transformation matrix $T_{\theta r}$, as shown in Figure 2.8.

$$\begin{bmatrix} i^s_{\alpha r} \\ i^s_{\beta r} \end{bmatrix} = T_{\theta r} \begin{bmatrix} i_{\alpha r} \\ i_{\beta r} \end{bmatrix} \tag{2.3.7}$$

where

$$T_{\theta r} = \begin{bmatrix} \cos\theta_r & -\sin\theta_r \\ \sin\theta_r & \cos\theta_r \end{bmatrix} \tag{2.3.8}$$

Note that, for simplified representation, the following $i_{\alpha r}$ and $i_{\beta r}$ are described for the rotor current vectors referred to the stator stationary reference frame, like in Figure 2.9(a).

2.3.3 Park transformation

A Park transformation transfer variables from a two-phase stator stationary reference frame to a two-phase rotating reference frame through the rotation transformation matrix $T_P(\theta)$, as shown in Figure 2.9(b).

$$\begin{bmatrix} i_{ds} \\ i_{qs} \end{bmatrix} = T_P(\theta) \begin{bmatrix} i_{\alpha s} \\ i_{\beta s} \end{bmatrix} \tag{2.3.9}$$

where $T_P(\theta)$ is the transformation matrix,

$$T_P(\theta) = \begin{bmatrix} \cos\theta & -\sin\theta \\ \sin\theta & \cos\theta \end{bmatrix} \tag{2.3.10}$$

where θ is the angle between d-axis and α-axis.

The same transformation in general orthogonal coordinates, rotating at genetic electric speed $\omega = \frac{d\theta}{dt}$, is valid for all currents and flux linkages. The transformation from three-phase (a-b-c) to two-phase stationary reference frame (α-β) and to a two-phase rotating reference frame (d-q) is summarized in Figure 2.10.

For the design of controllers, the stator and rotor equations should be referred to the same reference frame. The stator equations in the stator stationary reference frame α_s-β_s can be derived from (a-b-c) three-phase model (2.3.1) by using Clarke transformation T_C:

$$\begin{cases} u_{\alpha s} = R_s i_{\alpha s} + \dfrac{d\psi_{\alpha s}}{dt} \\ u_{\beta s} = R_s i_{\beta s} + \dfrac{d\psi_{\beta s}}{dt} \end{cases} \tag{2.3.11}$$

where $i_{\alpha s}$ and $i_{\beta s}$ are α-axis and β-axis stator currents, respectively; $\psi_{\alpha s}$ and $\psi_{\beta s}$ are α-axis and β-axis stator-flux linkages, respectively.

When the state variables in Eq.(2.3.11) are aligned with the rotating d-q frame by substituting the Park transformation matrix $T_P(\theta)$ into Eq.(2.3.11), after the computations of each variables from stationary to rotating reference frame, the equations can be written as:

$$\begin{cases} u_{ds} = R_s i_{ds} + \dfrac{d\psi_{ds}}{dt} - \omega\psi_{qs} \\ u_{qs} = R_s i_{qs} + \dfrac{d\psi_{qs}}{dt} + \omega\psi_{ds} \end{cases} \tag{2.3.12}$$

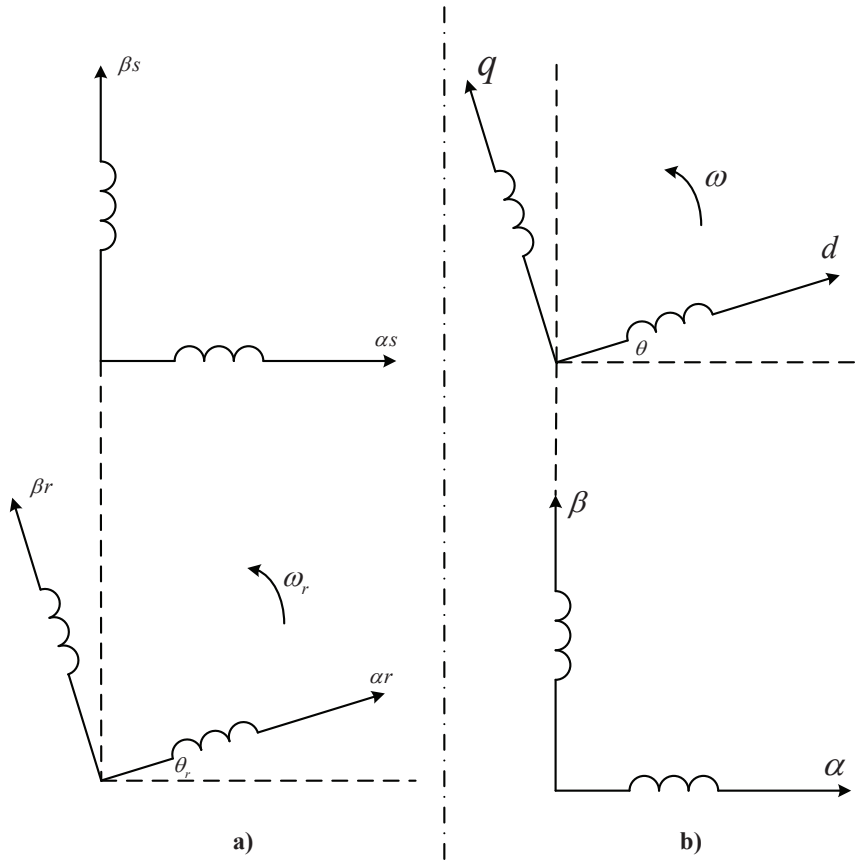

Figure 2.9: Park transformation

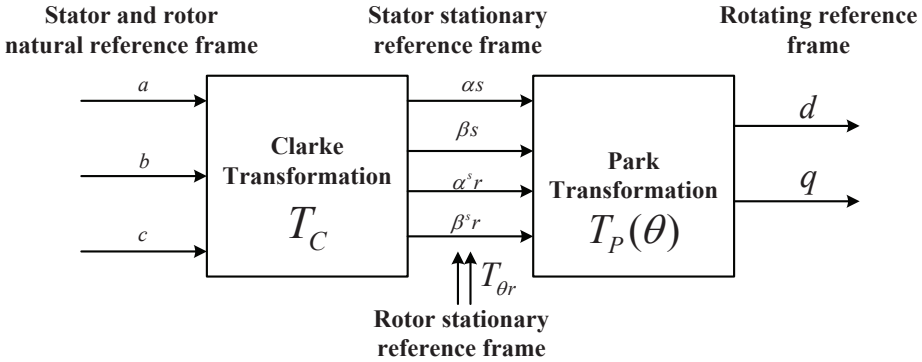

Figure 2.10: Transformation of reference frames

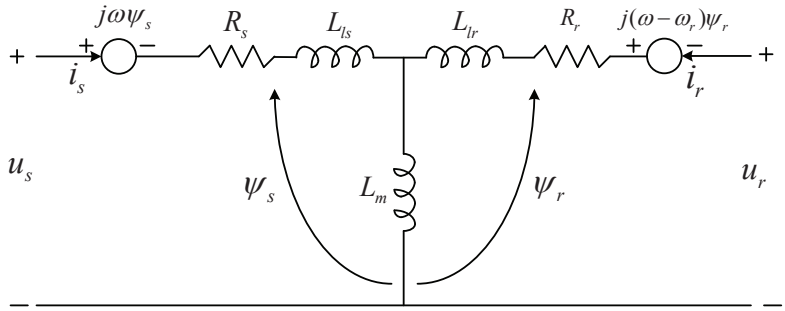

Figure 2.11: Dynamic d-q equivalent circuits of machine

where all the variables are in rotating reference frame, ω is the rotation speed. The last terms in equation (2.3.12) can be defined as speed emf due to rotation of the axes, that is, when $\omega = 0$, the equations revert to stationary form.

Since the rotor actually moves at speed ω_r against to the stator, the d-q axes fixed on the rotor move at a speed $\omega - \omega_r$. Therefore, in d-q frame, the rotor equations represented in the d-q frame as:

$$\begin{cases} u_{dr} = R_s i_{dr} + \dfrac{d\psi_{dr}}{dt} - (\omega - \omega_r)\psi_{qr} \\ u_{qr} = R_s i_{qr} + \dfrac{d\psi_{qr}}{dt} + (\omega - \omega_r)\psi_{dr} \end{cases} \tag{2.3.13}$$

Figure 2.11 shows the equivalent circuits for d-q dynamic model that satisfy equations (2.3.12) and (2.3.13), in which $u_s = u_{ds} + ju_{qs}$, the i_s, i_r, ψ_s, ψ_r can be presented in the same form, $L_s = L_{ls} + L_m$ is the stator self-inductance; $L_r = L_{lr} + L_m$ is the rotor self-inductance; L_{ls} is the stator leakage inductance; L_{lr} is the rotor leakage inductance; L_m is the mutual inductance.

The flux linkage expressions in terms of the currents can be obtained from Figure 2.11 as follows:

$$\begin{cases} \psi_{ds} = L_s i_{ds} + L_m i_{dr} \\ \psi_{qs} = L_s i_{qs} + L_m i_{qr} \\ \psi_{dr} = L_r i_{dr} + L_m i_{ds} \\ \psi_{qr} = L_r i_{qr} + L_m i_{qs} \end{cases} \tag{2.3.14}$$

The electromagnetic torque equation is represented as

$$T_e = \psi_{ds} i_{qs} - \psi_{qs} i_{ds} = L_m(i_{qs} i_{dr} - i_{ds} i_{qr}) = \psi_{dr} i_{qr} - \psi_{qr} i_{dr} \tag{2.3.15}$$

In summary, the model of DFIG under d-q rotating reference frame can be obtained by applying Clarke and Park transformations from equations (2.3.1) and (2.3.2):

$$\begin{cases} \dfrac{d\psi_{ds}}{dt} = u_{ds} - R_s i_{ds} + \omega \psi_{qs} \\ \dfrac{d\psi_{qs}}{dt} = u_{qs} - R_s i_{qs} - \omega \psi_{ds} \\ \dfrac{d\psi_{dr}}{dt} = u_{dr} - R_r i_{dr} + (\omega - \omega_r)\psi_{qr} \\ \dfrac{d\psi_{qr}}{dt} = u_{qr} - R_r i_{qr} - (\omega - \omega_r)\psi_{dr} \end{cases} \tag{2.3.16}$$

The speed ω of above model may take arbitrary value and result in conversion among different reference frames: stator stationary reference frame ($\omega = 0$), rotor stationary reference frame ($\omega = \omega_r$), synchronous rotating reference frame ($\omega = \omega_s$), where ω_s is synchronous speed.

The active and reactive stator power equations are presented as:

$$\begin{cases} P_s = u_{ds} i_{ds} + u_{qs} i_{qs} \\ Q_s = u_{qs} i_{ds} - u_{ds} i_{qs} \end{cases} \tag{2.3.17}$$

with the mathematical equations for computing the active and reactive powers of rotor side

$$\begin{cases} P_r = u_{dr} i_{dr} + u_{qr} i_{qr} \\ Q_r = u_{qr} i_{dr} - u_{dr} i_{qr} \end{cases} \tag{2.3.18}$$

2.4 Model of Grid-side Converter and DC-link

As shown in Figure 2.12, the power converter is made up of a back-to-back converter connecting the rotor circuit and the grid, which is known as a Scherbius scheme. The converters are typically made of voltage-fed current regulated inverters, which enable a two-directional power flow. The inverter valves make use of

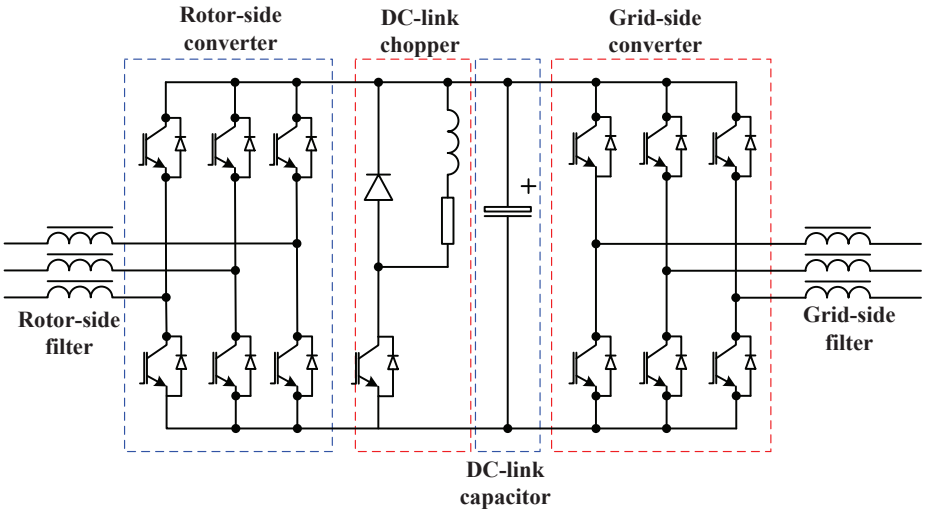

Figure 2.12: Power converter in DFIG based wind turbine

IGBTs provided with freewheeling diodes (see Figure 2.12). An LC-filter is provided on each converter output to minimize switching harmonics and to protect component insulation.

The power rating of the rotor-side converter is dictated by two factors, namely maximum slip power and reactive power control capability. The rotor-side converter can be seen as a current controlled voltage source converter. The rotor current can be controlled in several ways. The commonly used method is by utilizing a PWM modulation as presented in [6], [52]. Another option is to employ a hysteresis modulation method to the rotor-side converter [53]. The principle is also referred to as current-regulated modulation with a tolerance band control [54] or an adaptive current control PWM [55]. In this method, the current control tracks the phase rotor current to be within the hysteresis band by turning on the upper or lower valves of the converter based on a hysteresis control. When the rotor phase current exceeds the upper band, the lower valve of the corresponding phase is turned on and the upper valve is turned off. Similarly, when the actual current is below the lower band, the upper valve of the corresponding phase is turned on and the lower valve is turned off. This mechanism, in turn, forces the actual current to follow the current reference within a tolerance band. The hysteresis band width is defined by considering

the switching frequency limitations and the switching losses of the IGBTs [56].

The power rating of the grid-side converter is mainly dictated by maximum slip power since it usually operates at a unity power factor. A typical output voltage of the gride-side converter is 480 V [57].

The grid-side converter is normally dedicated to control the dc-link voltage and reactive power exchange between DC-link and the grid. It can also be utilized to support grid reactive power during a fault [58] and to enhance grid power quality [59]. However, these abilities are seldom utilized since they require a larger converter rating. In stability studies, it is well accepted to disregard the switching dynamics of the converter and treat them as an ideal device. In addition, converters are assumed to be able to follow the demanded values of the converter current fast enough [60].

A detailed model of a grid-side converter presented in [6] is recalled, where the converter is modeled as a current-controlled voltage source. This constitutes a representation of the dc-link capacitor and the grid-side filter in the model.

The ac-side circuit equation of the GSC can be written as

$$\frac{di_{gabc}}{dt} = -\frac{R_g}{L_g} i_{gabc} + \frac{1}{L_g}(u_{gabc} - u_{sabc}) \tag{2.4.1}$$

where i_{gabc}, u_{gabc}, u_{sabc} are the grid-side current, voltage and stator voltage in vectors, respectively; R_g and L_g are the reactance and inductance of grid-side converter.

By substituting the Clarke and Park transformation matrix Eq. (2.3.4) and (2.3.10) into Eq. (2.4.1), the equation of the GSC will be represented in the rotating reference frame. After that, aligning the d-axis of the state variables with the grid voltage vector u_s ($u_{ds} = u_s, u_{qs} = 0$), the following d-q vector model can be obtained for modeling the GSC ac-side:

$$\begin{cases} u_{dg} = R_g i_{dg} + L_g \dfrac{di_{dg}}{dt} - \omega_s L_g i_{qg} + u_s \\ u_{qg} = R_g i_{qg} + L_g \dfrac{di_{qg}}{dt} + \omega_s L_g i_{dg} \end{cases} \tag{2.4.2}$$

Neglecting harmonics due to switching and the losses in the GSC, the filtering inductor and the transformer, the power balance equation can be obtained as

$$P_{DC} = P_r - P_g = C u_{DC} \frac{du_{DC}}{dt} \tag{2.4.3}$$

where P_r is the active power at the AC terminal of the rotor-side converter; P_g is the active power at the AC terminal of the grid-side converter; P_{DC} is the active power of DC link. These are given by

$$P_r = u_{dr} i_{dr} + u_{qr} i_{qr} \tag{2.4.4}$$

$$P_g = u_{dg} i_{dg} + u_{qg} i_{qg} \tag{2.4.5}$$

$$P_{DC} = u_{DC} i_{DC} \tag{2.4.6}$$

where i_{dr} and i_{qr} are the d and q axis rotor currents, respectively; i_{dq} and i_{qg} are the d and q axis currents of grid-side converter, respectively; u_{dq} and u_{qg} are the d and q axis voltages of grid-side converter, respectively; v_{DC} is the capacitor DC voltage; i_{DC} is the current of the capacitor.

2.5 Summary

In this chapter, different topologies of wind turbine generation system were reviewed. Types of variable-speed wind turbines are implemented in the current wind power generation system more frequently than fix-speed wind turbine, as the wind power output is time-varying and uncertainty. Thereby, the control design for different objectives will be worked out, base on the variable-speed wind turbine with a doubly-fed induction generator in this thesis.

As follows, the dynamic modeling of drive train was investigated, and the one-mass lumped model of drive train run through the following studies. The detailed model of the DFIG system was also studied, with the Clarke and Park transformations. By apply the transformations, the state variables of the DFIG system can be transformed into the two-phase vectors oriented with different rotating reference frame, for simply controller design.

Finally, the dynamic of the DC-link capacitor and the grid-side converter considering the output filter were investigated for the studies on the control of grid-side converter.

Chapter 3

Nonlinear Power Control of DFIG based Wind Turbine

3.1 Problem Description

Currently, variable speed WPGSs are continuously increasing their market share, since they are capable of tracking the wind speed variations by adapting the shaft speed, and thus, achieving the optimal power generation. The mostly used WPGS are based on DFIG, which stator is connected to the grid directly and rotor connects through back to back converters. The major advantage of these facilities lies in the fact that the power rate of the inverters is around the 25-30 % of the nominal generator power.

The conventional control method for DFIG is vector control in which d-q components of rotor currents are directly linked with stator active power/reactive power (or torque / flux) and thus the current components can be used to control the stator active and reactive power, respectively, by transforming all variables into a reference frame fixed to stator flux vector (or voltage vector) [61], [62]. Regarding to this method, an accurate synchronization with the stator flux vector enables a decoupled control of the injection of the stator active power (P_s) and reactive power (Q_s), via the q-axis and the d-axis component of the rotor's currents. In addition to the decoupled control of the stator P_s and Q_s, the synchronous rotating reference

frame transforms enables the vector control to treat the state variables of the machine as DC signals. This feature has resulted in its implementation in most DFIG-WTs, though the tuning of the controller parameters is not an easy job.

Another drawback of the vector control is several transformations involved, as well as the heavenly dependence with the stator flux position measurement or estimation. Moreover, this method also requires accurate value of machine parameters such as resistances and inductances and nonlinear operation of the DFIG is not considered for tuning current controllers. Then performance of the vector control method is affected by changing machine parameters and operation condition.

In [53], DFIG control mechanisms are reported using the stator-flux-oriented frame with the position of the stator-flux space estimated through the measurement of the stator-flux space vector in α-β reference frame. In [63], a stator-flux-oriented DFIG control strategy is proposed, in which the position of the stator-flux space vector is estimated through the measurements of stator voltage and rotor-current space vectors in α-β reference frame. In [64], a stator-flux-oriented control of a cascaded doubly-fed induction machine is proposed, in which one of the main approaches used to estimate the position of stator flux space vector is to add a delay angle of 90^o to the stator voltage space vector. Other control approaches are also proposed recently, such as direct-power-control strategies using the stator-flux-oriented frame [11], [12].

The modeling of DFIG-WT used for conventional power control have been represented in the synchronous rotating reference frame as

$$\begin{cases} \dfrac{d\psi_{ds}}{dt} = u_{ds} - R_s i_{ds} + \omega_s \psi_{qs} \\ \dfrac{d\psi_{qs}}{dt} = u_{qs} - R_s i_{qs} - \omega_s \psi_{ds} \\ \dfrac{d\psi_{dr}}{dt} = u_{dr} - R_r i_{dr} + (\omega_s - \omega_r)\psi_{qr} \\ \dfrac{d\psi_{qr}}{dt} = u_{qr} - R_r i_{qr} - (\omega_s - \omega_r)\psi_{dr} \end{cases} \tag{3.1.1}$$

where

$$\begin{cases} \psi_{ds} = L_s i_{ds} + L_m i_{dr} \\ \psi_{qs} = L_s i_{qs} + L_m i_{qr} \\ \psi_{dr} = L_r i_{dr} + L_m i_{ds} \\ \psi_{qr} = L_r i_{qr} + L_m i_{qs} \end{cases} \tag{3.1.2}$$

where R_s and R_r are the stator and rotor resistance; (u_{ds}, u_{qs}), (u_{dr}, u_{qr}), (i_{ds}, i_{qs}), (i_{dr}, i_{qr}), (ψ_{ds}, ψ_{qs}), (ψ_{dr}, ψ_{qr}) are the d and q components of the space vector of stator and rotor voltage, currents, and fluxes; ω_r is the rotor speed; ω_s is the synchronous speed.

The stator active and reactive power can be computed by

$$\begin{cases} P_s = u_{ds} i_{ds} + u_{qs} i_{qs} \\ Q_s = u_{qs} i_{ds} - u_{ds} i_{qs} \end{cases} \tag{3.1.3}$$

In order to distinguish the difference of d and q components of a space vector in different orientation frames, the paper uses a superscript v representing stator-voltage-oriented frame and a superscript f signifying stator-flux-oriented frame in the following sections. Some related researches have been presented in [66].

3.2 Vector Control

Vector control of induction machine is a typical example of real application before theory development. Vector control of induction motor was proposed at 1970s' and originated from the ideas of control of alternative current (AC) induction motor like a direct current (DC) motor, while the corresponding nonlinear control techniques were only matured around 1990s. In terms of the feedback linearization technique, it is found that the vector control of induction motor can be represented by a coordinate transformation (via transforming variables to a special reference frame) and then a design of a linear controller (PI based). It has been shown that the vector control of induction motor can only achieve partial linearization of the original nonlinear system, i.e., only after the rotor flux has achieved its predefined reference value, the dynamic between torque (or rotor speed), and the rotor flux can

be decoupled; and then the relationship between the torque and the corresponding current component is linear. During the transient period of the rotor flux, such as the flux-weaken technique used in the high speed operation of induction motor to prevent the voltage saturation, dynamic between torque and rotor flux is still coupled. However, application of such techniques for DFIG has not reported in the available literatures.

In the past two decades, modeling and control of DFIG-WT have attracted extensive research efforts [6–14]. Among those results, the vector control (VC) with proportional-integral (PI) loops is the most used control algorithm for the regulation of the output power of the DFIG [6, 7] and is the current industrial standard, due to the capability of decoupling control of active and reactive power and simple structure. VC mainly consists of two steps: transforming the two-phase (α-β) stationary reference frame of DFIG model to a two-phase d-q rotating reference frame in which the d-axis is aligned with the vector of one of stator variables of the DFIG (stator-flux or stator-voltage); and decoupling the interaction among state variables, and independently controlling the active power and the reactive power by using the PI loops, through the d-q components of the rotor voltage. Most used reference frames are the stator-flux [6] and stator voltage orientated frame [8, 9]. Transformation of variables of the DFIG into a new rotating reference frame makes some components of the state variable under the new reference frame be zero, thus the decoupling of torque/active and reactive power and the linear relationship between the rotor current/voltage and the controlled variables can be achieved.

3.2.1 Control of rotor-side converter (RSC)

In this section, the conventional vector control methods for control of rotor-side converter are investigated, which the state vectors are oriented with two reference frames respectively. The control outputs are defined as the stator active and reactive power, after the frame transformation, the linear relationship between the control outputs and rotor current vectors can be obtained.

Stator flux orientation (SFO) frame

In the stator-flux orientation frame, the d-axis of the reference frame is aligned along the stator-flux vector so that the stator q-axis flux linkage is zero, and d-axis flux linkage is constant, equal to the amplitude of the stator flux $|\psi_s|$, that is

$$\begin{cases} \psi_{ds}^f = |\psi_s| \\ \psi_{qs}^f = 0 \end{cases} \tag{3.2.1}$$

Then, we can obtain that

$$\begin{cases} \dfrac{\psi_{ds}^f}{dt} = 0 \\ \dfrac{\psi_{qs}^f}{dt} = 0 \end{cases} \tag{3.2.2}$$

Based on first two equations of (3.1.1), and the assumption of ignoring the small stator winding resistance ($R_s \approx 0$), we have

$$\begin{cases} \dfrac{d\psi_{ds}^f}{dt} = u_{ds}^f - R_s i_{ds}^f + \omega_s \psi_{qs}^f = 0 \\ \dfrac{d\psi_{qs}^f}{dt} = u_{qs}^f - R_s i_{qs}^f - \omega_s \psi_{ds}^f = 0 \end{cases} \tag{3.2.3}$$

Thereby, by substituting the assumption $R_s \approx 0$ and the relationship given in Eq. (3.2.1) into (3.2.3), the stator voltage in stator-flux orientation frame can be obtained as:

$$\begin{cases} u_{ds}^f = 0 \\ u_{qs}^f = \omega_s \psi_{ds}^f = |u_s| \end{cases} \tag{3.2.4}$$

where the stator d-axis voltage is zero, and q-axis stator voltage is equal to the amplitude of the stator voltage $|u_s|$.

From (3.1.2), we have

$$\begin{cases} |\psi_s| = L_s i_{ds}^f + L_m i_{dr}^f \\ 0 = L_s i_{qs}^f + L_m i_{qr}^f \end{cases} \tag{3.2.5}$$

then

$$\begin{cases} i_{ds}^f = \dfrac{|\psi_s|}{L_s} - \dfrac{L_m}{L_s} i_{dr}^f \\ i_{qs}^f = -\dfrac{L_m}{L_s} i_{qr}^f \end{cases} \tag{3.2.6}$$

Hence, the stator active and reactive power can be rewritten by substituting Eq. (3.2.6) into (2.3.17):

$$P_s = 0 * i_{ds}^f + \omega_s \psi_{ds}^f * i_{qs}^f = \omega_s \psi_{ds}^f * (-\frac{L_m}{L_s} i_{qr}^f) = -\frac{L_m}{L_s} |u_s| i_{qr}^f \tag{3.2.7}$$

$$Q_s = \omega_s \psi_{ds}^f * (\frac{|\psi_s|}{L_s} - \frac{L_m}{L_s} i_{dr}^f) = \frac{|u_s||\psi_s|}{L_s} - \frac{L_m}{L_s} |u_s| i_{dr}^f \tag{3.2.8}$$

In the stator-flux orientation frame, the position of the stator-flux space vector θ_{sf} can be obtained directly from the stator flux measurement in stationary (α-β) reference frame by the equation $\theta_{sf} = \arctan(\psi_{\alpha s}/\psi_{\beta s})$. Therefore, the rotor voltage can be derived from the rotor currents as:

$$\begin{cases} u_{dr}^f = R_r i_{dr}^f + (L_r - \frac{L_m^2}{L_s}) \frac{di_{dr}^f}{dt} + \Delta_1^f \\ u_{qr}^f = R_r i_{qr}^f + (L_r - \frac{L_m^2}{L_s}) \frac{di_{qr}^f}{dt} + \Delta_2^f \end{cases} \tag{3.2.9}$$

where

$$\begin{cases} \Delta_1^f = -(\omega - \omega_r)(L_r - \frac{L_m^2}{L_s}) i_{qr}^f \\ \Delta_2^f = (\omega - \omega_r)(L_r - \frac{L_m^2}{L_s}) i_{dr}^f + (\omega - \omega_r) \frac{\psi_s L_m}{L_s} \end{cases} \tag{3.2.10}$$

Note that Δ_1^f and Δ_2^f are coupled terms which should be compensated via feed forward approach. Therefore, the linear relationship between rotor voltage and rotor current in stator-flux orientation frame can be obtained as:

$$\begin{cases} u_{dr}^f = R_r i_{dr}^f + (L_r - \frac{L_m^2}{L_s}) \frac{di_{dr}^f}{dt} \\ u_{qr}^f = R_r i_{qr}^f + (L_r - \frac{L_m^2}{L_s}) \frac{di_{qr}^f}{dt} \end{cases} \tag{3.2.11}$$

Figure 3.1 represents the conventional power control based on stator-flux orientation.

Stator voltage orientation (SVO) frame

In the stator-voltage orientation frame, the d-axis of the reference frame is aligned along the stator-voltage vector. Assuming that the grid voltage applied to the stator

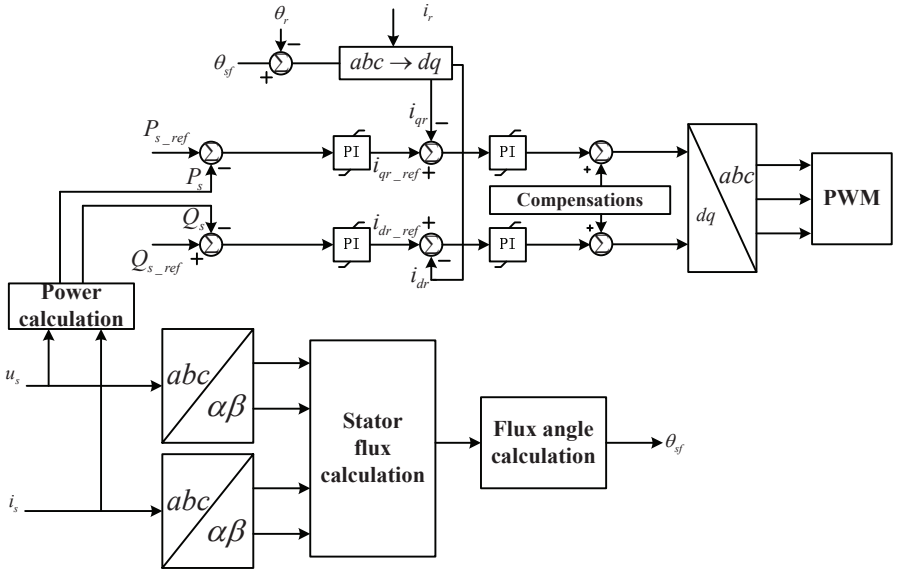

Figure 3.1: Power control under stator flux oriented frame

is constant, then, the stator q-axis voltage is zero, and the stator d-axis voltage is equal to the stator voltage amplitude $|u_s|$:

$$\begin{cases} u_{ds}^v = |u_s| \\ u_{qs}^v = 0 \end{cases} \tag{3.2.12}$$

and

$$\begin{cases} \dfrac{\psi_{ds}^f}{dt} = 0 \\ \dfrac{\psi_{qs}^f}{dt} = 0 \end{cases} \tag{3.2.13}$$

According to Eq. (3.1.1) and (3.2.3), the stator flux in stator-voltage orientation frame can be obtained as:

$$\begin{cases} \psi_{ds}^v = 0 \\ \psi_{qs}^v = |u_s|/\omega_s = |\psi_s| \end{cases} \tag{3.2.14}$$

From (3.1.2), we have

$$\begin{cases} 0 = L_s i_{ds}^v + L_m i_{dr}^v \\ |\psi_s| = L_s i_{qs}^v + L_m i_{qr}^v \end{cases} \tag{3.2.15}$$

and

$$\begin{cases} i_{ds}^{v} = \dfrac{L_m}{L_s} i_{dr}^{v} \\ i_{qs}^{v} = \dfrac{|\psi_s|}{L_s} - \dfrac{L_m}{L_s} i_{qr}^{v} \end{cases} \tag{3.2.16}$$

Then the stator active and reactive power can be rewritten as:

$$\begin{cases} P_s = -\dfrac{L_m}{L_s} u_s i_{dr}^{v} \\ Q_s = -u_s(\dfrac{\psi_s}{L_s} - \dfrac{L_m}{L_s} i_{qr}^{v}) \end{cases} \tag{3.2.17}$$

According to the derivation above, the real and reactive power references are linked with rotor d or q current references, respectively. Therefore, control of DFIG real and reactive power can be implemented by regulating rotor d or q current. In the stator-voltage orientation frame, the position of the stator voltage space vector θ_{sv} can be obtained directly from the stator voltage measurement in stationary (α-β) reference frame by the equation $\theta_{sv} = \arctan(u_{\alpha s}/u_{\beta s})$. Therefore, the rotor voltage can be derived from the rotor currents as:

$$\begin{cases} u_{dr}^{v} = (R_r i_{dr}^{v} + (L_r - \dfrac{L_m^2}{L_s}) \dfrac{di_{dr}^{v}}{dt} + \Delta_1^{v} \\ u_{qr}^{v} = R_r i_{qr}^{v} + (L_r - \dfrac{L_m^2}{L_s}) \dfrac{di_{qr}^{v}}{dt} + \Delta_2^{v} \end{cases} \tag{3.2.18}$$

where

$$\begin{cases} \Delta_1^{v} = -(\omega - \omega_r)(L_r - \dfrac{L_m^2}{L_s}) i_{qr}^{v} - (\omega - \omega_r) \dfrac{L_m}{L_s} \psi_s \\ \Delta_2^{v} = +(\omega - \omega_r)(L_r - \dfrac{L_m^2}{L_s}) i_{dr}^{v} + \dfrac{L_m}{L_s} \psi_s \end{cases} \tag{3.2.19}$$

Note that Δ_1^{v} and Δ_2^{v} are coupled terms which should be compensated via feed forward approach. Therefore, the linear relationship between rotor voltage and rotor current in stator-voltage orientation frame can be obtained as:

$$\begin{cases} u_{dr}^{v} = R_r i_{dr}^{v} + (L_r - \dfrac{L_m^2}{L_s}) \dfrac{di_{dr}^{v}}{dt} \\ u_{qr}^{v} = R_r i_{qr}^{v} + (L_r - \dfrac{L_m^2}{L_s}) \dfrac{di_{qr}^{v}}{dt} \end{cases} \tag{3.2.20}$$

In figure 3.2, the conventional power control based on stator-voltage orientation can be represented in Figure .

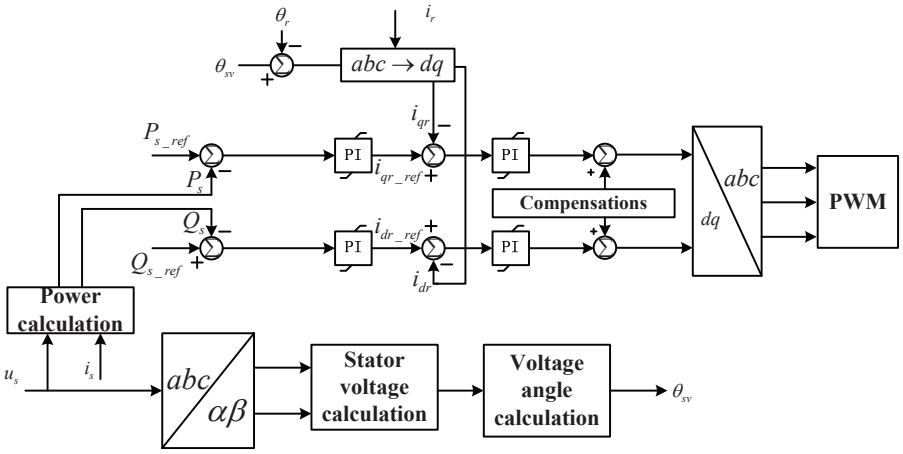

Figure 3.2: Power control under stator voltage oriented frame

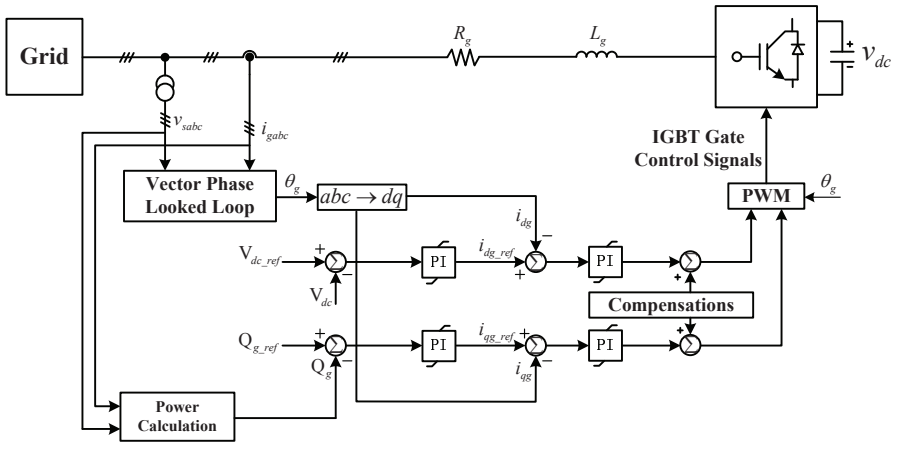

Figure 3.3: Vector control scheme of grid-side converter

3.2.2 Control of grid-side converter (GSC)

Conventional vector control for GSC

The grid-side control scheme consists of two control loop: the inner current control loops regulate independently the d and q axis grid AC-side current components, in the synchronously rotating reference frame; the outer control loops regulate the dc-link voltage and the reactive power exchanged between the GSC and the grid.

In Figure 3.3, the AC-side circuit equations of the GSC, by applying the synchronously rotating reference frame transformation with the d-axis aligned to the grid voltage vector ($u_{ds} = u_s, u_{qs} = 0$),can be written as:

$$\begin{cases} \dfrac{di_{dg}}{dt} = \dfrac{u_{dg}}{L_g} - \dfrac{R_g}{L_g} i_{dg} - u_s + \omega_s i_{qg} \\ \dfrac{di_{qg}}{dt} = \dfrac{u_{qg}}{L_g} - \dfrac{R_g}{L_g} i_{qg} - \omega_s i_{dg} \end{cases} \tag{3.2.21}$$

where R_g and L_g are the grid-side resistance and inductance.

As the same procedure as the control of rotor-side converter, the conventional vector control method is applied for control of grid-side converter. The control inputs u_{dg} and u_{qg} can be obtained by the following feedback loops and PI controllers

$$\begin{cases} u_{dg} = (k_{pg} + \dfrac{k_{ig}}{s})(i_{dg\_ref} - i_{dg}) - \omega_s L_g i_{qg} + u_s \\ u_{qg} = (k_{pg} + \dfrac{k_{ig}}{s})(i_{qg\_ref} - i_{qg}) + \omega_s L_g i_{dg} \end{cases} \tag{3.2.22}$$

where the reference values i_{dg_ref} and i_{qg_ref} are obtained from the outer control loop.

Neglecting harmonics due to switching and the losses in the GSC, the filtering inductor and the transformer, the power balance equation if given by

$$P_{DC} = P_r - P_g = C u_{DC} \frac{du_{DC}}{dt} \tag{3.2.23}$$

Let

$$u_{DC} = u_{DC0} + \Delta u_{DC} \tag{3.2.24}$$

where $u_{DC0} = u_{DC\_ref}$ is the dc component of u_{DC}, Δu_{DC} is the ripple component of u_{DC}. Substituting (3.2.24) into (3.2.23) gives

$$P_r - P_g = C u_{DC0} \frac{du_{DC}}{dt} + C \Delta u_{DC} \frac{du_{DC}}{dt} \tag{3.2.25}$$

Since $\Delta u_{DC} \ll u_{DC0}$, (3.2.25) can be written as

$$P_r - P_g \approx C u_{DC0} \frac{du_{DC}}{dt} \tag{3.2.26}$$

Therefore, the transfer function from P_g to u_{DC} is given by

$$\frac{u_{DC}(s)}{P_g(s)} = \frac{1}{C u_{DC0} s} \tag{3.2.27}$$

Since

$$P_g = \frac{3}{2} u_{ds} i_{dg} = \frac{3}{2} u_s i_{dg} \tag{3.2.28}$$

Therefore, it is possible to design a feedback loop and PI controller to generate the reference value of i_{dg} as follows:

$$i_{dg\_ref} = (k_{pu} + \frac{k_{iu}}{s})(u_{DC\_ref} - u_{DC}) \tag{3.2.29}$$

The reactive power exchanged between the GSC and the grid is given by

$$Q_g = -\frac{3}{2} u_{ds} i_{qg} = -\frac{3}{2} |u_s| i_{qg} \tag{3.2.30}$$

Therefore, the reference value of i_{dg} can be determined directly from the reactive power command.

3.3 Direct Power Control (DPC) via Feedback Linearization Control

In this section, the feedback linearization control method is applied to directly control stator active and reactive powers, compared with the asymptotical characteristics of DFIG provided by the VC. To design nonlinear decoupled controller for stator active and reactive power, the DFIG system in stationary reference frame can be rewritten in a compact form as:

$$\dot{x} = f(x) + b_1 u_{\alpha r} + b_2 u_{\beta r} \tag{3.3.1}$$

where $x = [\psi_{\alpha s} \;\; \psi_{\beta s} \;\; \psi_{\alpha r} \;\; \psi_{\beta r} \;\; \omega_r]^T$

$$f(x) = \begin{bmatrix} u_{\alpha s} - R_s i_{\alpha s} \\ u_{\beta s} - R_s i_{\beta s} \\ -R_r i_{\alpha r} - \omega_r \psi_{\beta r} \\ -R_r i_{\beta r} + \omega_r \psi_{\alpha r} \end{bmatrix} \tag{3.3.2}$$

and

$$b_1 = [0\ 0\ 1\ 0]^T \tag{3.3.3}$$

$$b_2 = [0\ 0\ 0\ 1]^T \tag{3.3.4}$$

According to the equation 3.1.2, the stator and rotor currents represented in the stationary reference frame can be written as:

$$\begin{cases} i_{\alpha s} = -\dfrac{L_r}{L_\sigma}\psi_{\alpha s} + \dfrac{L_m}{L_\sigma}\psi_{\alpha r} \\ i_{\beta s} = -\dfrac{L_r}{L_\sigma}\psi_{\beta s} + \dfrac{L_m}{L_\sigma}\psi_{\beta r} \\ i_{\alpha r} = \dfrac{L_m}{L_\sigma}\psi_{\alpha s} - \dfrac{L_s}{L_\sigma}\psi_{\alpha r} \\ i_{\beta r} = \dfrac{L_m}{L_\sigma}\psi_{\beta s} - \dfrac{L_s}{L_\sigma}\psi_{\beta r} \end{cases} \tag{3.3.5}$$

Stator active power P_s and reactive power Q_s can be represented in terms of stator voltages and currents under the stationary reference frame as:

$$\begin{cases} P_s &= u_{\alpha s} i_{\alpha s} + u_{\beta s} i_{\beta s} \\ Q_s &= u_{\beta s} i_{\alpha s} - u_{\alpha s} i_{\beta s} \end{cases} \tag{3.3.6}$$

Let stator active power P_s and reactive power Q_s as the controlled outputs,

$$\begin{cases} y_1 = P_s \\ y_2 = Q_s \end{cases}, \tag{3.3.7}$$

then we can obtain

$$\begin{cases} \dot{P}_s = F_1 + \dfrac{L_m u_{\alpha s}}{L_\sigma} u_{\alpha r} + \dfrac{L_m u_{\beta s}}{L_\sigma} u_{\beta r} \\ \dot{Q}_s = F_2 + \dfrac{L_m u_{\beta s}}{L_\sigma} u_{\alpha r} - \dfrac{L_m u_{\alpha s}}{L_\sigma} u_{\beta r} \end{cases} \tag{3.3.8}$$

where

$$\begin{aligned} F_1 = &-\tfrac{L_r}{L_\sigma}(u_{\alpha s}(u_{\alpha s} - R_s i_{\alpha s}) - u_{\beta s}(u_{\beta s} - R_s i_{\beta s})) \\ &+\tfrac{L_m}{L_\sigma}(u_{\alpha s}(-R_r i_{\alpha r} - \omega_r \psi_{\beta r}) + u_{\beta s}(-R_r i_{\beta r} + \omega_r \psi_{\alpha r})) \end{aligned} \tag{3.3.9}$$

$$\begin{aligned} F_2 = &-\tfrac{L_r}{L_\sigma}(u_{\beta s}(u_{\alpha s} - R_s i_{\alpha s}) + u_{\alpha s}(u_{\beta s} - R_s i_{\beta s})) \\ &+\tfrac{L_m}{L_\sigma}(u_{\beta s}(-R_r i_{\alpha r} - \omega_r \psi_{\beta r}) - u_{\alpha s}(-R_r i_{\beta r} + \omega_r \psi_{\alpha r})) \end{aligned} \tag{3.3.10}$$

Define the tracking errors as:

$$\begin{cases} e_1 = P_s - P_{s\_ref} \\ e_2 = Q_s - Q_{s\_ref} \end{cases} \tag{3.3.11}$$

where P_{s_ref} and Q_{s_ref} are the reference values of the active and the reactive power, respectively. The dynamical system of the track error can be obtained based on equation (3.3.8) as:

$$\begin{bmatrix} \dot{e_1} \\ \dot{e_2} \end{bmatrix} = \begin{bmatrix} F_1 - \dot{P}_{s\_ref} \\ F_2 - \dot{Q}_{s\_ref} \end{bmatrix} + B \begin{bmatrix} u_{\alpha r} \\ u_{\beta r} \end{bmatrix} \tag{3.3.12}$$

$$B = \begin{bmatrix} \frac{L_m}{L_\sigma} u_{\alpha s} & \frac{L_m}{L_\sigma} u_{\beta s} \\ \frac{L_m}{L_\sigma} u_{\beta s} & -\frac{L_m}{L_\sigma} u_{\alpha s} \end{bmatrix} \tag{3.3.13}$$

where B is the control gains matrix which is not singular when $det(B) = -\frac{L_m^2}{L_\sigma^2}(u_{\alpha s}^2 + u_{\beta s}^2) \neq 0$, when $|u_s| \neq 0$.

The FLC control can be obtained as

$$\begin{bmatrix} u_{\alpha r} \\ u_{\beta r} \end{bmatrix} = B^{-1} \left\{ \begin{bmatrix} -F_1 + \dot{P}_{s\_ref} \\ -F_2 + \dot{Q}_{s\_ref} \end{bmatrix} + \begin{bmatrix} v_1 \\ v_2 \end{bmatrix} \right\} \tag{3.3.14}$$

$$\begin{bmatrix} v_1 \\ v_2 \end{bmatrix} = \begin{bmatrix} -k_1 e_1 \\ -k_2 e_2 \end{bmatrix} \tag{3.3.15}$$

where v_1 and v_2 are control input of the linear system, k_1, k_2 are the feedback gains.

The linearized system is

$$\begin{bmatrix} \dot{e}_1 \\ \dot{e}_2 \end{bmatrix} = \begin{bmatrix} v_1 \\ v_2 \end{bmatrix} \tag{3.3.16}$$

And resulted linear system as

$$\begin{cases} \dot{e}_1 + k_1 e_1 = 0 \\ \dot{e}_2 + k_2 e_2 = 0 \end{cases} \tag{3.3.17}$$

3.4 Cascaded Power Control via Rotor Current Regulation (RC & FLC)

In this section, the input/output feedback linearization control (IOFLC) technique is used to design a fully decoupled power control law to improve the asymptotical characteristics of DFIG provided by VC, based on a full-order DFIG model in the synchronous reference frame. The stator stationary frame model of the DFIG will be used to improve the transient dynamics under unsymmetrical grid faults. This control strategy consists of an outer loop, obtaining the rotor current references from the stator active and reactive powers, and an inner loop, which applies the IOFLC for the current regulation. The dynamic model of DFIG has been rewritten in the state variable of stator and rotor current vectors as

$$\begin{cases} \dfrac{di_{\alpha s}}{dt} = \dfrac{L_m}{L_\sigma}u_{\alpha r} - \dfrac{L_r}{L_\sigma}u_{\alpha s} + \dfrac{R_s L_r}{L_\sigma}i_{\alpha s} - \dfrac{R_r L_m}{L_\sigma}i_{\alpha r} - \omega_r L_m \dfrac{L_r i_{\beta r} + L_m i_{\beta s}}{L_\sigma} \\ \dfrac{di_{\beta s}}{dt} = \dfrac{L_m}{L_\sigma}u_{\beta r} - \dfrac{L_r}{L_\sigma}u_{\beta s} + \dfrac{R_s L_r}{L_\sigma}i_{\beta s} - \dfrac{R_r L_m}{L_\sigma}i_{\beta r} + \omega_r L_m \dfrac{L_r i_{\alpha r} + L_m i_{\alpha s}}{L_\sigma} \\ \dfrac{di_{\alpha r}}{dt} = \dfrac{L_m}{L_\sigma}u_{\alpha s} - \dfrac{L_s}{L_\sigma}u_{\alpha r} - \dfrac{R_s L_m}{L_\sigma}i_{\alpha s} + \dfrac{R_r L_s}{L_\sigma}i_{\alpha r} + \omega_r L_s \dfrac{L_r i_{\beta r} + L_m i_{\beta s}}{L_\sigma} \\ \dfrac{di_{\beta r}}{dt} = \dfrac{L_m}{L_\sigma}u_{\beta s} - \dfrac{L_s}{L_\sigma}u_{\beta r} - \dfrac{R_s L_m}{L_\sigma}i_{\beta s} + \dfrac{R_r L_s}{L_\sigma}i_{\beta r} - \omega_r L_s \dfrac{L_r i_{\alpha r} + L_m i_{\alpha s}}{L_\sigma} \end{cases} \tag{3.4.1}$$

3.4.1 The inner control loop: IOFLC

For the controller design, the state vector of (3.4.1) can be split into two parts

$$\dot{i}_s = A_{11}i_s + A_{12}i_r + B_1 u_s + C_1 u_r \tag{3.4.2}$$

$$\dot{i}_r = A_{21}i_s + A_{22}i_r + B_2 u_s + C_2 u_r \tag{3.4.3}$$

where

$$i_s = \begin{bmatrix} i_{\alpha s} \\ i_{\beta s} \end{bmatrix} \tag{3.4.4}$$

$$i_r = \begin{bmatrix} i_{\alpha r} \\ i_{\beta r} \end{bmatrix} \tag{3.4.5}$$

$$u_s = \begin{bmatrix} u_{\alpha s} \\ u_{\beta s} \end{bmatrix} \tag{3.4.6}$$

$$u_r = \begin{bmatrix} u_{\alpha r} \\ u_{\beta r} \end{bmatrix} \tag{3.4.7}$$

$$\left[\begin{array}{c|c} A_{11} & A_{12} \\ \hline A_{21} & A_{22} \end{array}\right] = \left[\begin{array}{cc|cc} \frac{R_s L_r}{L_\sigma} & -\frac{\omega_r L_m^2}{L_\sigma} & -\frac{R_r L_m}{L_\sigma} & -\frac{\omega_r L_m L_r}{L_\sigma} \\ \frac{\omega_r L_m^2}{L_\sigma} & \frac{R_s L_r}{L_\sigma} & \frac{\omega_r L_m L_r}{L_\sigma} & -\frac{R_r L_m}{L_\sigma} \\ \hline -\frac{R_s L_m}{L_\sigma} & \frac{\omega_r L_m L_s}{L_\sigma} & \frac{R_r L_s}{L_\sigma} & \frac{\omega_r L_s L_r}{L_\sigma} \\ -\frac{\omega_r L_m L_s}{L_\sigma} & -\frac{R_s L_m}{L_\sigma} & -\frac{\omega_r L_s L_r}{L_\sigma} & \frac{R_r L_s}{L_\sigma} \end{array}\right] \tag{3.4.8}$$

$$\left[\begin{array}{c} B_1 \\ \hline B_2 \end{array}\right] = \left[\begin{array}{cc} -\frac{L_r}{L_\sigma} & 0 \\ 0 & -\frac{L_r}{L_\sigma} \\ \hline \frac{L_m}{L_\sigma} & 0 \\ 0 & \frac{L_m}{L_\sigma} \end{array}\right] \tag{3.4.9}$$

$$\left[\begin{array}{c} C_1 \\ \hline C_2 \end{array}\right] = \left[\begin{array}{cc} \frac{L_m}{L_\sigma} & 0 \\ 0 & \frac{L_m}{L_\sigma} \\ \hline -\frac{L_s}{L_\sigma} & 0 \\ 0 & -\frac{L_s}{L_\sigma} \end{array}\right] \tag{3.4.10}$$

The choice of rotor current loop control stems from the fact that the rotor current during a fault is directly controlled, thus allowing the safe use of the entire rotor-side converter current capability. Therefore, the objective is to define a control law that ensures the trajectories of rotor current (3.4.3) to move toward a predefined reference $i_{r\_ref} = [i_{\alpha r\_ref} \quad i_{\beta r\_ref}]^T$ and reach it in a finite period of time even in the presence of uncertainties. So the track error $e_{ir} = i_{r\_ref} - i_r$ must satisfy the following conditions:

$$\begin{cases} \lim\limits_{t\to\infty} (i_{\alpha r\_ref} - i_{\alpha r}) = 0 \\ \lim\limits_{t\to\infty} (i_{\beta r\_ref} - i_{\beta r}) = 0 \end{cases} \tag{3.4.11}$$

From (3.4.3), the dynamic equation of rotor current error is

$$\dot{e}_{ir} = \dot{i}_{r\_ref} - \dot{i}_r = \dot{i}_{r\_ref} - (A_{21} i_s + A_{22} i_r + B_2 u_s + C_2 u_r) \tag{3.4.12}$$

After adding $A_{22}i_{r\_ref} - A_{22}i_{r\_ref}$, it becomes

$$\dot{e}_{ir} = A_{22}e_{ir} - C_2u_r + g \tag{3.4.13}$$

where g is given by

$$g = \dot{i}_{r\_ref} - A_{21}i_s - B_2u_s - A_{22}i_{r\_ref} \tag{3.4.14}$$

Design the nonlinear feedback control input u_r as

$$u_r = C_2^{-1}(A_{22}e + g - v) \tag{3.4.15}$$

where C_2 is nonsingular for all time in the domain of interest, as $det(C_2) = L_s^2/L_\sigma^2 \neq 0$; $v = [v_1 \quad v_2]^T$ is the linear control input.

The dynamic system of the track error (3.4.12) can also be presented as follows:

$$\dot{e}_{ir} = \begin{bmatrix} \dot{e}_1 \\ \dot{e}_2 \end{bmatrix} = \begin{bmatrix} \dot{i}_{\alpha r\_ref} - F_1 \\ \dot{i}_{\beta r\_ref} - F_2 \end{bmatrix} - C_2 \begin{bmatrix} u_{\alpha r} \\ u_{\beta r} \end{bmatrix} \tag{3.4.16}$$

where

$$\begin{cases} F_1 = \dfrac{L_m}{L_\sigma}u_{\alpha s} - \dfrac{R_sL_m}{L_\sigma}i_{\alpha s} + \dfrac{R_rL_s}{L_\sigma}i_{\alpha r} + \omega_rL_s\dfrac{L_ri_{\beta r} + L_mi_{\beta s}}{L_\sigma} \\ F_2 = \dfrac{L_m}{L_\sigma}u_{\beta s} - \dfrac{R_sL_m}{L_\sigma}i_{\beta s} + \dfrac{R_rL_s}{L_\sigma}i_{\beta r} - \omega_rL_s\dfrac{L_ri_{\alpha r} + L_mi_{\alpha s}}{L_\sigma} \end{cases} \tag{3.4.17}$$

The FLC control (3.4.15) can be rewritten in

$$\begin{bmatrix} u_{\alpha r} \\ u_{\beta r} \end{bmatrix} = C_2^{-1}\left\{ \begin{bmatrix} \dot{i}_{\alpha r\_ref} - F_1 \\ \dot{i}_{\beta r\_ref} - F_2 \end{bmatrix} - \begin{bmatrix} v_1 \\ v_2 \end{bmatrix} \right\} \tag{3.4.18}$$

$$\begin{bmatrix} v_1 \\ v_2 \end{bmatrix} = \begin{bmatrix} -k_1e_1 \\ -k_2e_2 \end{bmatrix} \tag{3.4.19}$$

where v_1 and v_2 are control input of the linear system, k_1, k_2 are the feedback gains. As a result, the linearized system can be written as:

$$\begin{cases} \dot{e}_1 + k_1e_1 = 0 \\ \dot{e}_2 + k_2e_2 = 0 \end{cases} \tag{3.4.20}$$

3.4.2 The outer loop: rotor current reference calculation

Assumptions

- In a sinusoidal steady state at a fundamental grid frequency, the amplitude and frequency of stator current are constants
- The transient response of stator power reference is ignored
- The controller proposed in (3.4.15) works properly

Under the assumptions, the rotor current vector error e_{ir} can be $e_{ir} = 0$. In order to obtain the reference of rotor current from stator current, substituting (3.4.14) and (3.4.15) into (3.4.2) results in

$$\dot{i}_s = (A_{11} - C_1 C_2^{-1} A_{21}) i_s + (B_1 - C_1 C_2^{-1}) u_s + (A_{12} - C_1 C_2^{-1} A_{22}) i_{r\_ref} + C_1 C_2^{-1} \dot{i}_{r\_ref} \tag{3.4.21}$$

The time derivative of the rotor and stator currents can be expressed as

$$\dot{i}_{r\_ref} = \begin{bmatrix} 0 & \omega_s \\ -\omega_s & 0 \end{bmatrix} i_{r\_ref} \tag{3.4.22}$$

$$\dot{i}_s = \begin{bmatrix} 0 & \omega_s \\ -\omega_s & 0 \end{bmatrix} i_s \tag{3.4.23}$$

In this section, the outputs of the DFIG based WT to be controlled are the stator active and reactive power. They can be expressed in terms of stator currents and voltages and represented as

$$\begin{bmatrix} P_s \\ Q_s \end{bmatrix} = \begin{bmatrix} u_{\alpha s} & u_{\beta s} \\ u_{\beta s} & -u_{\alpha s} \end{bmatrix} \begin{bmatrix} i_{\alpha s} \\ i_{\beta s} \end{bmatrix} \tag{3.4.24}$$

Then the stator current vectors i_s can be represented in terms of stator voltages and powers:

$$\begin{bmatrix} i_{\alpha s} \\ i_{\beta s} \end{bmatrix} = \frac{1}{u_{\alpha s}^2 + u_{\beta s}^2} \begin{bmatrix} u_{\alpha s} & u_{\beta s} \\ u_{\beta s} & -u_{\alpha s} \end{bmatrix} \begin{bmatrix} P_s \\ Q_s \end{bmatrix} \tag{3.4.25}$$

Substituting (3.4.22), (3.4.23), (3.4.25) into (3.4.21), the rotor current reference cane be computed from stator active and reactive power references as:

$$\begin{bmatrix} i_{\alpha r\_ref} \\ i_{\beta\_ref} \end{bmatrix} = -\frac{H_1}{u_{\alpha s}^2 + u_{\beta s}^2} \begin{bmatrix} u_{\alpha s} & u_{\beta s} \\ u_{\beta s} & -u_{\alpha s} \end{bmatrix} \begin{bmatrix} P_{s\_ref} \\ Q_{s\_ref} \end{bmatrix} + H_2 u_s \tag{3.4.26}$$

where

$$H_1 = \begin{bmatrix} \frac{L_s}{L_m} & -\frac{R_s}{\omega_s L_m} \\ \frac{R_s}{\omega_s L_m} & \frac{L_s}{L_m} \end{bmatrix} \tag{3.4.27}$$

$$H_2 = \begin{bmatrix} 0 & -\frac{1}{\omega_s L_m} \\ \frac{1}{\omega_s L_m} & 0 \end{bmatrix} \tag{3.4.28}$$

and P_{s_ref} and Q_{s_ref} are the reference values of the active and the reactive power, respectively.

The detailed control schedule can be summarized in Figure 3.4.

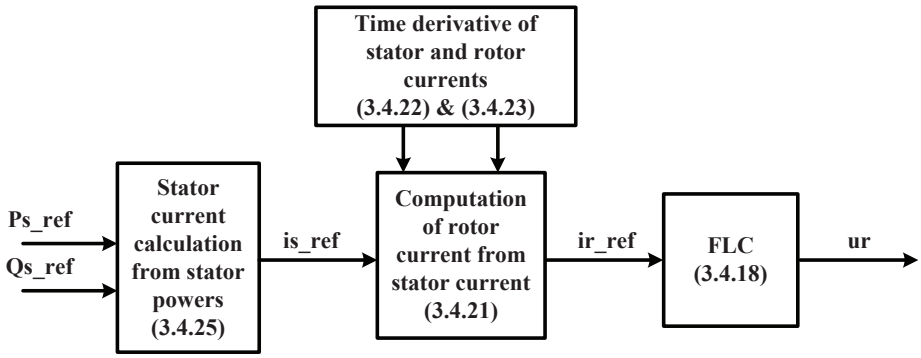

Figure 3.4: Reference computation of rotor current from stator active and reactive power

3.5 Simulation Studies

In this section, simulation studies are carried out by using MATLAB/SIMULINK based on GE $3.6MW$ DFIG-WT. The parameters are given as $R_s = 0.0079pu$, $R_r = 0.025pu$, $L_{ls} = 0.7937pu$, $L_m = 4.4pu$, $L_{lr} = 0.40pu$, $R_e = 0.014pu$,

Table 3.1: Control parameters of FLC and proposed controller

	k_1	k_2
FLC	20	20
RC & FLC	100	100

$X_e = 0.08pu$, base frequency $f = 60Hz$, $H_m = 5.19s$, $D_m = 0$, rotor diameter of wind turbine $= 104m$.

For the outer control loop of conventional power control by VC, the proportional gains of the stator active and reactive power regulation are $2e^{-4}$ and $1e^{-5}$, and the integral time constants are 1 and 0.5, respectively; for inner current control loop, the proportional gain and integral time constant are 0.01 and 0.2, respectively.

The control parameters of FLC, RC are also given in Table 3.1.

3.5.1 Variation of operation points

For simulating the varying operation status, two step changes of signals are applied on stator active and reactive power respectively, as shown in Figure 3.5. The comparison among the performance of three control strategies are given as follows. Figures 3.6 and 3.7 show that the VC, DPC and RC & FLC can track the power references after the step change. However, the VC performs not good enough while the operation point changes, as it only works at specific operation point. The errors between the active power reference and the controlled active power show more clearly comparison among three control strategies. In Figures 3.8-3.9, the dynamic response of stator reactive power by applying VC, DPC and RC & FLC are illustrated. The proposed RC & FLC performs better than other two control methods during the step change of reference powers.

3.5.2 Grid disturbance

To simulate the grid disturbance, the stator voltage is set as a step change from 4160 V to 3000 V, and then recover to 4160 V after 200 ms. Figures 3.10 and 3.11 show the dynamic responses of stator active and reactive power under disturbance

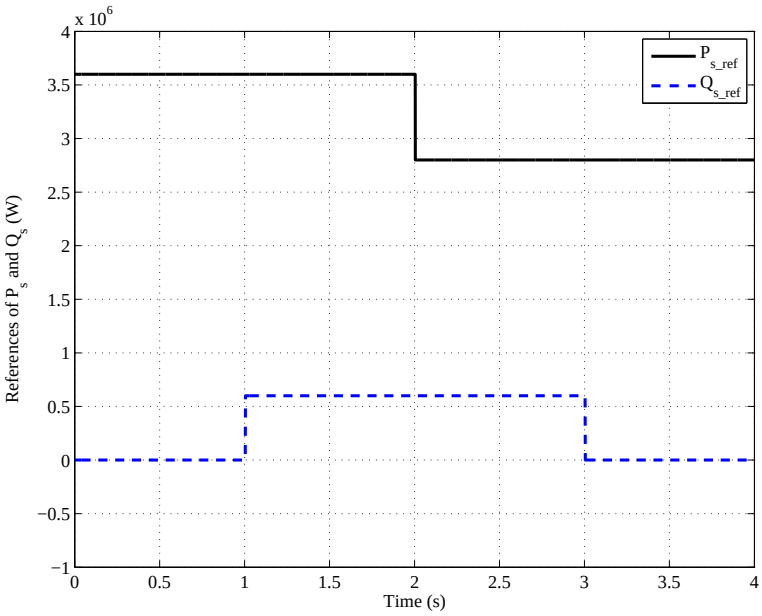

Figure 3.5: References of stator active and reactive power

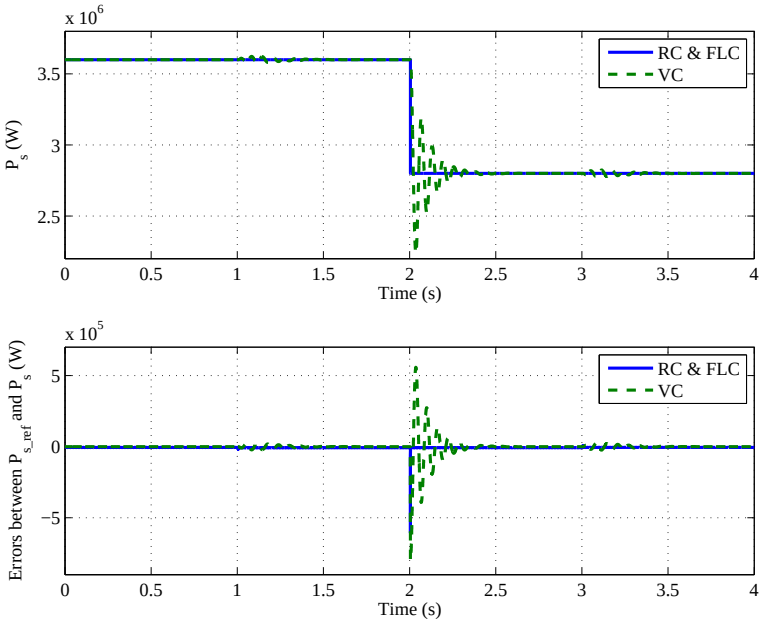

Figure 3.6: Stator active power regulation by RC & FLC, VC and tracking error

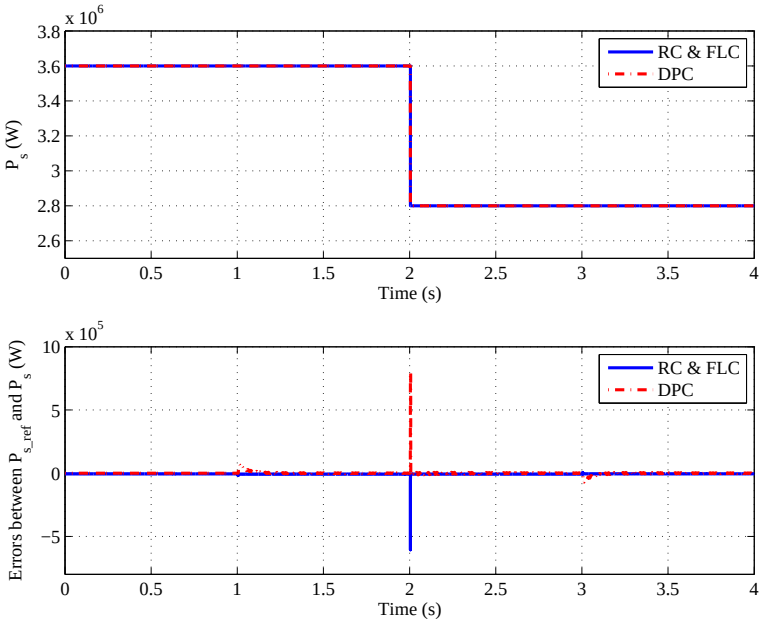

Figure 3.7: Stator active power regulation by RC & FLC, DPC and tracking error

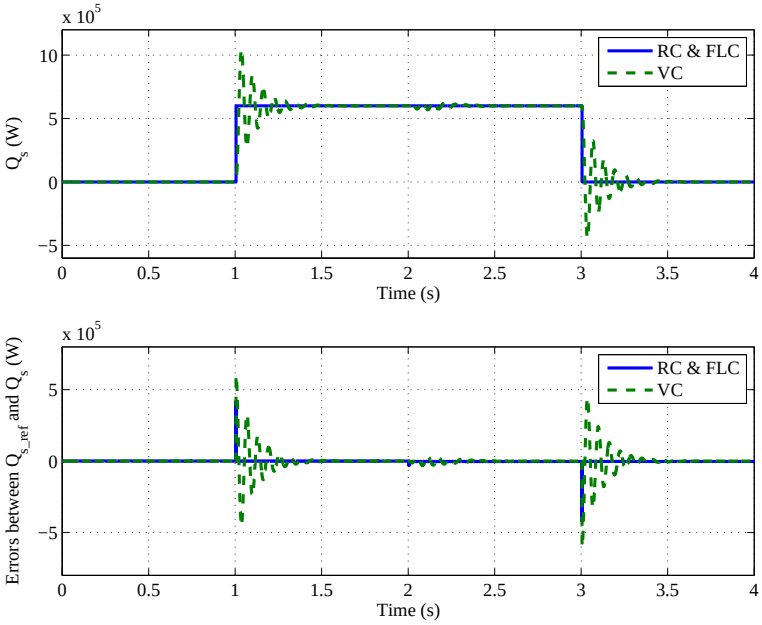

Figure 3.8: Stator reactive power regulation by RC & FLC, VC and tracking error

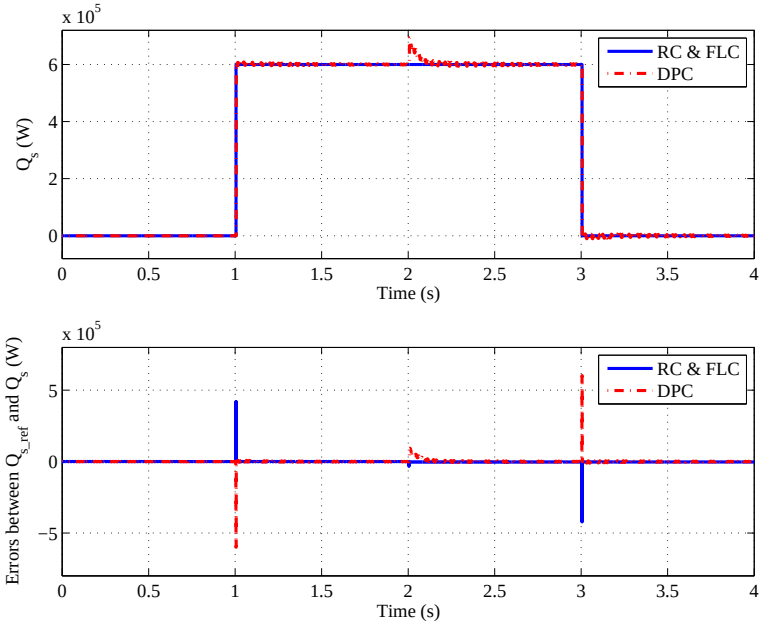

Figure 3.9: Stator reactive power regulation by RC & FLC, DPC and tracking error

by applying VC, DPC and RC & FLC. In Figure 3.10 (a), the performance of stator active power regulation via the proposed RC & FLC is compared with those of VC and DPC. During the grid disturbance, the proposed controller can regulate the stator active power to the reference value faster and more accurate than VC and DPC. Also from the results shown in Figure 3.11, the stator reactive power controlled via RC & FLC can compensate the loss of active power during the grid fault, and after the disturbance, the stator reactive power can be regulated as the minimum value faster than other two control methods. In this section, it can be summarized that the performance of proposed control strategy shows better transient response and more accurate power regulations during the grid disturbance.

3.6 Summary

In this chapter, the decoupling power control of DFIG-WT via conventional vector control method was investigated at first. The conventional vc strategy comprised by the PI controllers and the compensation parts, can achieve the cancelation of

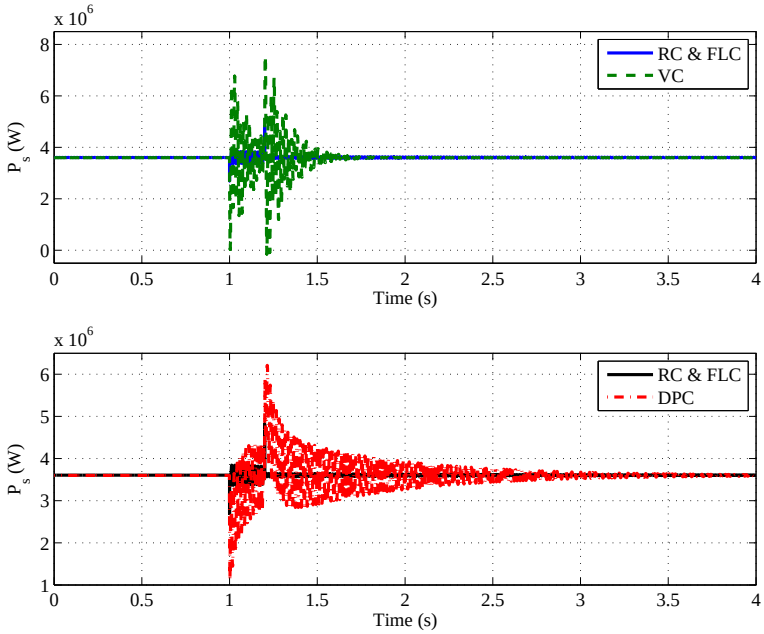

Figure 3.10: Responses of stator active power under grid disturbance

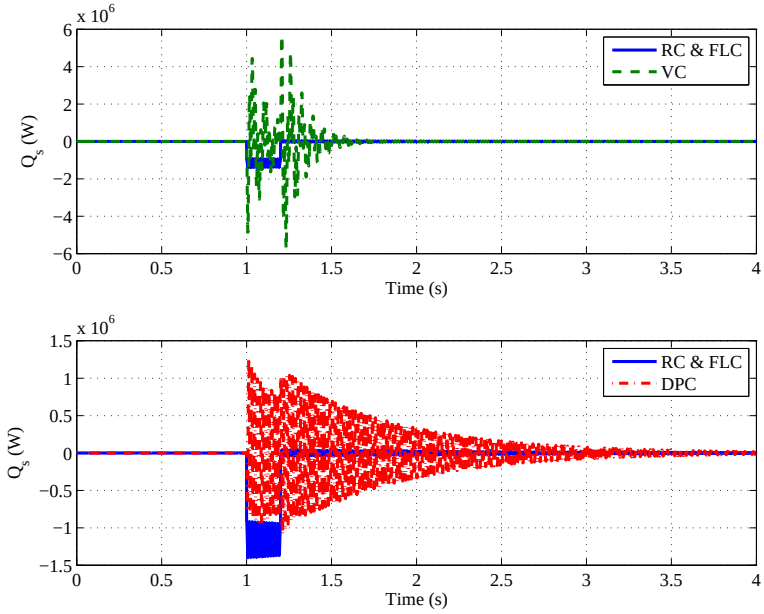

Figure 3.11: Responses of stator reactive power under grid disturbance

coupled dynamics at the feed forward control loop. However, the VC method is not capable of providing a satisfactory transient response for DFIG-WT under the time-varying operation points and grid disturbance due to the following reasons: The parameters of PI control loop can only provide optimal performance around one special operation point, which not valid for time-varying operation points; The control performance will be degraded, as the assumptions for control design were destroyed during the grid faults or voltage sags.

To improve the transient response and achieve full decoupling power control, two control schemes were proposed based on the nonlinear feedback linearization control method. One of them is the direct stator active and reactive power control (DPC), and the other one is called as the cascaded power control via rotor current (RC & FLC). The RC & FLC scheme consists of an outer control loop, for obtaining the rotor current references from stator active and reactive powers, and an inner control loop, which applied the input/output feedback linearization control for the rotor current regulation.

To demonstrate the performance of the proposed control schemes, case studies on the variation of operation points, and grid disturbance were carried out. According to the simulation results and analysis, it shows that the proposed RC & FLC is able to achieve smooth and satisfactory power regulation during the time-varying operation and grid disturbance.

Chapter 4

Nonlinear Control based Maximum Power Point Tracking

4.1 Problem Formulation

To achieve high efficiency in wind power conversion system, the maximum power point tracking (MPPT) in variable-speed WPGS equipped with doubly-fed induction generator (DFIG) or permanent magnetic synchronous generator (PMSG) has attracted lots of attention [67], [68], [69]. Basically, the MPPT methods proposed include three strategies, namely, (1) the methods relying on the measurement of wind speed, (2) the methods relying on output power measurement and calculation, and (3) the methods relying on the optimal power versus rotor speed characteristic curve.

When maximum wind energy is tracked without measuring wind speed, there are mainly polynomial estimation of the power coefficient [78], power mapping [79] and look-up table [80] methods. Polynomial estimation needs online iteration computing for many times, which increases the complexity and reduces the applicability of the control system. Power mapping takes a lot of storage space. Otherwise, the required control accuracy can not be achieved. The slowness of look-up table also affects the tracking effect.

Recently, a proposed topology of employing the power versus rotor speed char-

acteristic curve is used frequently [70], [71], [72], [73], relying on neither difficult wind speed measurements nor complicated estimation algorithm. The optimal reference power curve is constructed according to the experimental tests and stored in micro controller memory, working as a look-up table. One could either measure the rotor speed to obtain power reference and then regulate the power, or measure the wind speed to obtain rotor speed reference and then regulate the rotor speed. The former produces more accurate output power while the latter will have faster dynamic response [74]. Most research in such kind of method simply apply the cube of rotor speed to generate reference power or the square of rotor speed to generate reference torque, which neglect the exact relationship between maximum power and corresponding rotor speed [6], [8]. Such approximation will obviously lead to inaccurate results. More importantly, analysis is necessary as well to verify the stability of the method in terms of varying wind speed and output power. Few paper just address the stability issue of the method proposed in [75], but more detailed quantitative analysis should be conducted.

Modeling for MPPT

The fifth-model of DFIG system (2.2.7) and (2.3.16) for MPPT under synchronous rotating reference frame are written as:

$$\begin{cases} \dfrac{d\omega_r}{dt} = \dfrac{1}{2H_m}(T_m - T_e - D_m\omega_r) \\ \dfrac{d\psi_{ds}}{dt} = u_{ds} - R_s i_{ds} + \omega_s \psi_{qs} \\ \dfrac{d\psi_{qs}}{dt} = u_{qs} - R_s i_{qs} - \omega_s \psi_{ds} \\ \dfrac{d\psi_{dr}}{dt} = u_{dr} - R_r i_{dr} + (\omega_s - \omega_r)\psi_{qr} \\ \dfrac{d\psi_{qr}}{dt} = u_{qr} - R_r i_{qr} - (\omega_s - \omega_r)\psi_{dr} \end{cases} \tag{4.1.1}$$

where H_m is the lumped inertia constant, D_m is the damping of the lumped system, T_m is the mechanical torque given as $T_m = P_m/w_r$. R_s and R_r are the stator and rotor resistance; (u_{ds}, u_{qs}), (u_{dr}, u_{qr}), (i_{ds}, i_{qs}), (i_{dr}, i_{qr}), (ψ_{ds}, ψ_{qs}), (ψ_{dr}, ψ_{qr}) are the d and q components of the space vector of stator and rotor voltage, currents, and fluxes; ω_r is the rotor speed; ω_s is the synchronous speed.

The flux linkage expressions in terms of the currents are given by

$$\begin{cases} \psi_{ds} = L_s i_{ds} + L_m i_{dr} \\ \psi_{qs} = L_s i_{qs} + L_m i_{qr} \\ \psi_{dr} = L_r i_{dr} + L_m i_{ds} \\ \psi_{qr} = L_r i_{qr} + L_m i_{qs} \end{cases} \tag{4.1.2}$$

The electromagnetic torque equation is represented in

$$T_e = \psi_{ds} i_{qs} - \psi_{qs} i_{ds} = L_m (i_{qs} i_{dr} - i_{ds} i_{qr}) = \psi_{dr} i_{qr} - \psi_{qr} i_{dr} \tag{4.1.3}$$

4.1.1 Maximum Power Point Tracking

Operation of a typical wind turbine can be divided into 4 regions as shown in Figure 4.1. In region 1, wind speed is too low to drive the wind turbine. Hence wind turbine would not rotate until wind speed reaches the minimum speed that able to drive the wind turbine rotating. This typical wind speed is so-called cut-in speed. When wind turbine start operating, power output keep increasing as the wind speed increases. When the output power reaches a rated value of the electrical generator, power output will stop increasing. The minimum wind speed that enables wind turbine constantly maintains at the rated power is called rated wind speed. The range between cut-in speed and rated speed is defined as region 2, maximum power point tracking (MPPT) control is applied in this region in order to maximize power output of the wind turbine, pitch angle is fixed in this region to enable the blades receive maximum pressure from the air. As output power increases when wind speed increases, wind turbine will reach its rated power output, pitch angle control is applied to regulate the blades to receive proper pressure such that the input power from wind will not exceed the rated power of the generator. Wind turbine will be cut out and stopped to protect itself from damaged from the maximum mechanical stress when the wind speed is higher than the range of pitch angle control. Region 3 is defined between rated wind speed and cut-out speed. When wind turbine is stopped generating power, its operation belongs to region 4.

Give a C_p function as follows:

$$C_p(\beta, \lambda) = \sum_{i=0}^{4} \sum_{j=0}^{4} \alpha_{ij} \beta^i \lambda^j \tag{4.1.4}$$

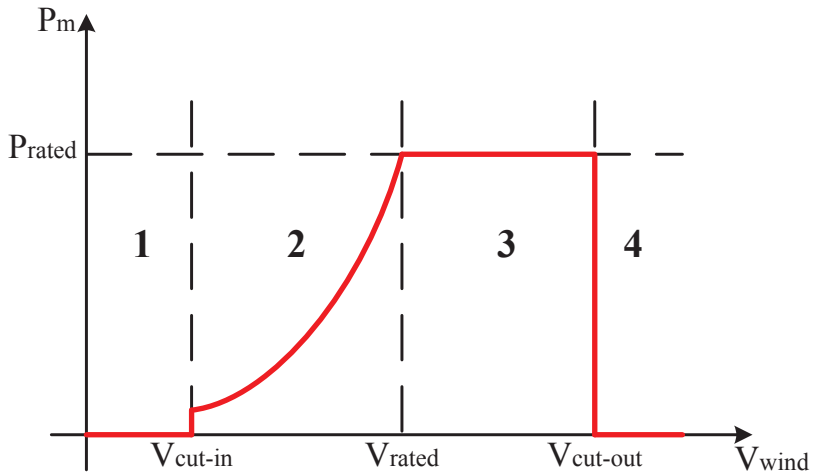

Figure 4.1: Wind turbine operation regions

The curves of the C_p is shown in Figure 4.2, which illustrates the power coefficient against the tip speed ratio. For each pitch angle there is an optimum tip speed ratio which reaches the maximum power coefficient.

The $C_p(\beta, \lambda)$ curve is specific for each wind turbine. It has a unique maximum C_{p_max} at a single point for a given pitch angle.

$$C_{p\_max} = C_p(\beta, \lambda_{opt}) \tag{4.1.5}$$

In order to reach the maximum C_p, the tip speed ratio must be maintained as λ_{opt} under the time-varying wind speed. That is, the rotor speed must track its optimal reference as

$$\omega_{r\_opt} = \frac{\lambda_{opt} V_{wind}}{R} \tag{4.1.6}$$

where R is the length of turbine blade. In this case, the wind speed should be measured for the calculation of optimal rotor speed.

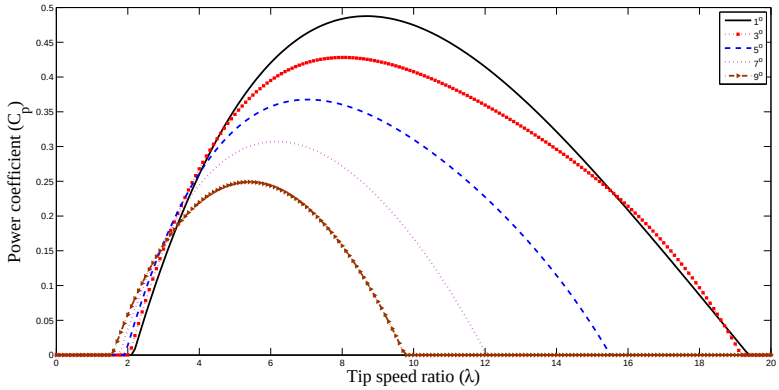

Figure 4.2: The power coefficient C_p versus tip speed ratio at different pitch angles

4.1.2 Control objective

The aim of this chapter is to maximize the output power for variable speed operation of DFIG based wind turbine and minimizing the stator reactive power. The maximum mechanical output power can be obtained by adjusting the rotor speed or electric torque to maximum the power coefficient. The stator reactive power will be maintained as minimum for achieving the maximum generated active power.

The nonlinear controller design relies on the wind speed measurement available, that the rotor speed will be controlled to track the optimal reference speed $\frac{\lambda_{opt} V_{wind}}{R}$ to achieve the maximum power coefficient.

4.2 Feedback Linearization Control

4.2.1 Principle of FLC

In the conventional linearization method, the system is approximately linearized by the first-order Taylor's series based on one operation point. An evident shortage of this method is that the information of higher order derivatives is discarded. Thus the accuracy of transformed system may deteriorate dramatically or even yield contradictory results in the presence of nonlinearity, this in turn inevitably leads the control performance deterioration for operation point varying far away from the

linearized operation point.

Feedback linearization is a typical approach in nonlinear control design. The central idea is to algebraically transform a nonlinear system dynamics into an equivalent (fully or partly) linear one through an appropriate coordinate transformation and a nonlinear control input, after that linear control techniques can be then applied. The nonlinearity of the system is entirely comsidered in the global state space and can be used for both stabilization and tracking control tasks.

The basic concept of input-output linearization is briefly recalled. By input-output linearization, it means the generation of a linear differential relation between the output y and a new input v, then design u to cancel the nonlinearity. A linear controller is systematically synthesized for the linear input-state model to impose the desired linear dynamics. Without the loss of generality, consider a standard affine nonlinear MIMO system in a neighborhood of a point x_0 of the form

$$\begin{cases} \dot{x} = f(x) + g(x)u \\ y = h(x) \end{cases} \tag{4.2.1}$$

where $x \in R^n$ is the state vector, $u \in R^m$ is the control input vector, $y \in R^m$ is the output vector, $f(x)$, $g(x)$ and $h(x)$ are the smooth and continuous vector fields. The input-output linearisation of a MIMO system is obtained via differentiating the output y_i of the system until the input u_j appears, assuming that r_i is the smallest integer such that at least one of the inputs explicitly appears in $y_i^{(r_i)}$

$$y_i^{(r_i)} = L_f^{r_i} h_i + \sum_{j=1}^{m} L_{g_j} L_f^{r_i - 1} h_i u_j \tag{4.2.2}$$

where $y_i^{(r_i)}$ denotes the i^{th}-order derivative of y_i, if $L_{g_j} L_f^{r_i-1} h_i(x) \neq 0$ for at least one j, by continuity that relation is preserved in a finite neighborhood Ω_i of the point x_0. Performing the above procedure for each output y_i gives

$$\begin{bmatrix} y_1^{(r_1)} \\ \vdots \\ y_m^{(r_m)} \end{bmatrix} = \begin{bmatrix} L_f^{r_1} h_1 \\ \vdots \\ L_f^{r_m} h_m \end{bmatrix} + B(x) \begin{bmatrix} u_1 \\ \vdots \\ u_m \end{bmatrix} \tag{4.2.3}$$

$$B(x) = \begin{bmatrix} L_{g_1} L_f^{r_1-1} h_1 & \cdots & L_{g_m} L_f^{r_1-1} h_1 \\ \vdots & \vdots & \vdots \\ L_{g_1} L_f^{r_m-1} h_m & \cdots & L_{g_m} L_f^{r_m-1} h_m \end{bmatrix} \tag{4.2.4}$$

Here $B(x)$ is the $m \times m$ control gain matrix. Define the Ω as the intersection of the Ω_i. If the partial "relative degrees" r_i are all well defined, then Ω is itself a finite neighborhood of x_0. Furthermore, if $B(x)$ is invertible, the physical control law of the MIMO nonlinear system is calculated immediately by

$$u = B(x)^{-1} \left\{ \begin{bmatrix} -L_f^{r_1} h_1 \\ \vdots \\ -L_f^{r_m} h_m \end{bmatrix} + \begin{bmatrix} v_1 \\ \vdots \\ v_m \end{bmatrix} \right\} \tag{4.2.5}$$

where v_i are new inputs of the equivalent linear systems expressed as

$$y_i^{(r_i)} = v_i \tag{4.2.6}$$

Since the input v_i only affects the output y_i it is called the decoupling control law, and the invertible matrix $B(s)$ is called the decoupling matrix of the system. The system Eq. (4.2.1) is then said to have relative degree $(r_1, \ldots, r_m)$ at x_0, and the scalar $r = r_1 + \ldots + r_m$ is called the total relative degree of the system at x_0.

Assume now it is desired to track a prespecified trajectory $y_{id} = [y_{id}^{(r_i)} \; y_{id}^{(r_i-1)} \; \ldots \; y_{id}]$. Choosing the artificial input v as a simple linear pole-placement controller provides any guarantee about the stability of the overall system:

$$v_i = y_{id}^{(r_i)} - \alpha_{r_i-1} e_i^{(r_i-1)} - \ldots - \alpha_1 \dot{e}_i - \alpha_0 e_i \tag{4.2.7}$$

where $e_i = y_i - y_{id}$ leads to the tracking error dynamics and α_i are the control gains, the proposed control law yields the following characteristic equation

$$s^{(r_i)} + \alpha_{r_i-1} s^{(r_i-1)} + \ldots + \alpha_1 s + \alpha_0 = 0 \tag{4.2.8}$$

Now nominal stability of the system, and therefore boundedness of the output, is ensured if the controller tuning coefficients α_i are chosen such that Eq. (4.2.8) is a Hurwitz polynomial. To this end, any desired dynamics can be imposed on the new system.

4.2.2 Control Design for MPPT

Choosing the rotor speed ω_r and stator reactive power Q_s as the controlled outputs it obtains

$$\begin{cases} y_1 = \omega_r \\ y_2 = Q_s \end{cases} \tag{4.2.9}$$

Let ω_{r_opt} and Q_s^* be the given references of the rotor speed and reactive power respectively, and define the tracking error $e = [e_1 \;\; e_2]^T$ as:

$$e = \begin{bmatrix} e_1 \\ e_2 \end{bmatrix} = \begin{bmatrix} \omega_r - \omega_{r\_opt} \\ Q_s - Q_s^* \end{bmatrix} \tag{4.2.10}$$

The input/output feedback linearization of equation (4.1.1) can be obtained as:

$$\begin{bmatrix} \ddot{e}_1 \\ \dot{e}_2 \end{bmatrix} = \begin{bmatrix} f_1 - \ddot{\omega}_{r\_opt} \\ f_2 - \dot{Q}_s^* \end{bmatrix} + B(x) \begin{bmatrix} u_{dr} \\ u_{qr} \end{bmatrix} \tag{4.2.11}$$

where

$$\begin{aligned} f_1 = {} & \tfrac{\dot{T}_m}{2H_m} - \tfrac{1}{2H_m}((-u_{qs} + R_s i_{qs} + \omega_s \psi_{ds})(\tfrac{L_r}{L_\sigma}\psi_{ds} + i_{ds}) \\ & + (u_{ds} - R_s i_{ds} + \omega_s \psi_{qs})(i_{qs} + \tfrac{L_r}{L_\sigma}\psi_{qs}) - \tfrac{L_m}{L_\sigma}\psi_{ds}(R_r i_{qr} \\ & + (\omega_s - \omega_r)\psi_{dr}) - \tfrac{L_m}{L_\sigma}\psi_{qs}(-R_r i_{dr} + (\omega_s - \omega_r)\psi_{qr})) \end{aligned} \tag{4.2.12}$$

$$\begin{aligned} f_2 = {} & u_{qs}\tfrac{L_m}{L_\sigma}(-R_r i_{dr} + (\omega_s - \omega_r)\psi_{qr}) - u_{qs}\tfrac{L_r}{L_\sigma}(u_{ds} - \\ & R_s i_{ds} + \omega_{qs}) - u_{ds}\tfrac{L_m}{L_\sigma}(-R_r i_{qr} - (\omega_s - \omega_r)\psi_{dr}) + \\ & u_{ds}\tfrac{L_r}{L_\sigma}(u_{qs} - R_s i_{qs} - \omega_s \psi_{ds}) \end{aligned} \tag{4.2.13}$$

and

$$B(x) = \begin{bmatrix} \frac{L_m}{2H_m L_\sigma}\psi_{qs} & -\frac{L_m}{2H_m L_\sigma}\psi_{ds} \\ \frac{L_m}{L_\sigma}u_{qs} & -\frac{L_m}{L_\sigma}u_{ds} \end{bmatrix} \tag{4.2.14}$$

where $B_0(x) = B(x)|_{L_m = L_{m0}}$, $\Delta B(x) = B(x) - B_0(x)$. Note that when $det(B) = 0.5\frac{L_m^2}{H_m L_\sigma^2}(-\psi_{qs}u_{ds} + \psi_{ds}u_{qs}) \neq 0$, system (4.2.11) can be linearized as following

$$\begin{bmatrix} \ddot{e}_1 \\ \dot{e}_2 \end{bmatrix} = \begin{bmatrix} v_1 \\ v_2 \end{bmatrix} \tag{4.2.15}$$

where $v = [v_1 \;\; v_2]^T$ is the control input of the linear system defined as

$$\begin{bmatrix} v_1 \\ v_2 \end{bmatrix} = - \begin{bmatrix} k_{11}e_1 + k_{12}\dot{e}_1 \\ k_{21}e_2 \end{bmatrix} \tag{4.2.16}$$

where k_{11}, k_{12}, k_{21} are the feedback gains.

Then the FLC control law of equation (4.1.1) can be obtained as follows

$$\begin{bmatrix} u_{dr} \\ u_{qr} \end{bmatrix} = B(x)^{-1}(\begin{bmatrix} -f_1 + \ddot{\omega}_{r\_opt} \\ -f_2 + \dot{Q}_s^* \end{bmatrix} + v) \tag{4.2.17}$$

4.3 Modal Analysis

The dynamic performance of the controller proposed is cooperatively carried out by modal analysis and simulation tool. Through examining each system mode trajectory the system stability can be directly analyzed, then simulation tool can be then used to verify the obtained results.

Small signal stability is the stability of power system under small disturbance. The disturbance occurs continuously because of small load or change of voltage in the power system. Normally, this disturbance will be treated as small enough, which can make linearization of system equations easily during system analysis [76].

Since power system small signal stability concerns the ability of the system to maintain stable subject to small disturbances, eigenvalue analysis is suitable for the studies of small signal stability. The original system under study is first linearized at the operating point to derive the linear state equations from which the system matrix is obtained. Then the eigenvalues of the system matrix are calculated for checking the small signal stability. If all the real parts of eigenvalues are negative, the system will be classified as stable. It is noted that the system to be studied usually has high order system matrix due to the large number of generators so that it will be time consuming to calculate and to analyze all the eigenvalues. It is most desirable in system planning and operation to find out only those eigenvalues corresponding to the mode with lowest damping, and/or to all unstable oscillatory modes, instead of all the system eigenvalues for fast determination of system stability.

4.3.1 Introduction of modal analysis method

The behavior of a dynamic system, such as a power system, may be described by $\dot{x} = f(x, u)$. For analyzing the stability of dynamic system, linearization of

dynamic equations should be carried out first. Let x_0 be the initial state vector and u_0 the input vector corresponding to the equilibrium point about which the small-signal performance is to be investigated. When x_0 and u_0 satisfy the equation above, we have

$$\dot{x_0} = f(x_0, u_0) = 0 \tag{4.3.1}$$

Let's perturb the system from above state, by setting $x = x_0 + \Delta x$ and $u = u_0 + \Delta u$, where the prefix Δ denotes a small deviation. The new state should also satisfy equation $\dot{x} = f(x, u)$. Hence,

$$\dot{x} = \dot{x_0} + \Delta\dot{x} + f[(x_0 + \Delta x), (u_0 + \Delta u)] \tag{4.3.2}$$

As the perturbations are assumed to be small, the nonlinear functions $f(x, u)$ can be expressed in terms of Taylor's series expansion . With terms involving second and higher order powers of Δx and Δu neglected, we can write

$$\begin{aligned} \dot{x_i} &= \dot{x}_{i0} + \Delta\dot{x_i} = f_i[(x_0 + \Delta x), (u_0 + \Delta u)] \\ &= f_i(x_0, u_0) + \tfrac{\partial f_i}{\partial x_1}\Delta x_1 + \ldots + \tfrac{\partial f_i}{\partial x_n}\Delta x_n + \tfrac{\partial f_i}{\partial u_1}\Delta u_1 + \tfrac{\partial f_i}{\partial u_r}\Delta u_r \end{aligned} \tag{4.3.3}$$

Since $\dot{x_{i0}} = f_i(x_0, u_0)$, we obtain

$$\Delta\dot{x_i} = \frac{\partial f_i}{\partial x_1}\Delta x_1 + \ldots + \frac{\partial f_i}{\partial x_n}\Delta x_n + \frac{\partial f_i}{\partial u_1}\Delta u_1 + \ldots + \frac{\partial f_i}{\partial u_r}\Delta u_r \tag{4.3.4}$$

with i=1,2,...,n. Therefore, the linearized forms of $\dot{x} = f(x, u)$ can be written as

$$\Delta\dot{x} = A\Delta x + B\Delta u \tag{4.3.5}$$

where

$$A = \begin{pmatrix} \frac{\partial f_1}{\partial x_1} & \cdots & \frac{\partial f_1}{\partial x_n} \\ \cdots & \cdots & \cdots \\ \frac{\partial f_n}{\partial x_1} & \cdots & \frac{\partial f_n}{\partial x_n} \end{pmatrix}$$

$$B = \begin{pmatrix} \frac{\partial f_1}{\partial u_1} & \cdots & \frac{\partial f_1}{\partial u_r} \\ \cdots & \cdots & \cdots \\ \frac{\partial f_n}{\partial u_1} & \cdots & \frac{\partial f_n}{\partial u_r} \end{pmatrix}$$

The above partial derivatives are evaluated at the equilibrium point about which the small perturbation is being analyzed. By taking the Laplace transform of the above equations, we obtain the state equations in the frequency domain:

$$s\Delta x(s) - \Delta x(0) = A\Delta x(s) + B\Delta u(s) \tag{4.3.6}$$

Rearranging it, we have

$$(sI - A)\Delta x(s) = \Delta x(0) + B\Delta u(s) \tag{4.3.7}$$

We can see that the Laplace transform of Δx have two components, on dependent on the initial conditions and the other on the inputs. These are the Laplace transforms of the free and zero-state components of the state and output vectors.

The poles of $\Delta x(s)$ are the roots of the equation

$$det(sI - A) = 0 \tag{4.3.8}$$

where the values of s are known as eigenvalues of matrix A, and equation above is referred to as the characteristic equation of matrix A.

For example, the eigenvalues of a matrix are given by the values of the scalar parameter λ_i for which there exist non-trivial solutions to the equation

$$A\Phi = \lambda_i\Phi \tag{4.3.9}$$

where A is an n*n matrix, Φ is an n*1 vector

To find the eigenvalues, the equation may be written in the form

$$(A - \lambda_i I)\Phi = 0 \tag{4.3.10}$$

For a non-trivial solution

$$det(A - \lambda_i I) = 0 \tag{4.3.11}$$

Expansion of the determinant gives the characteristic equation. The n solutions of $\lambda_i = \lambda_1, \lambda_2, ...\lambda_n$ are eigenvalues of A. The eigenvalues may be real or complex. If A is real, complex eigenvalues always occur in conjugate pairs.

The time dependent characteristic of a mode corresponding to an eigenvalue λ_i is

given by $e^{\lambda_i t}$. Therefore, the stability of the system is determined by the eigenvalues as follows:

(a) A real eigenvalue corresponds to a non-oscillatory mode. A negative real eigenvalue represents a decaying mode. The larger its magnitude, the faster the decay. A positive real eigenvalue represents aperiodic instability.

(b) Complex eigenvalues occur in conjugate pairs, and each pair corresponds to an oscillatory mode.

The associated eigenvectors will have appropriate complex values so as to make the entries of $x(t)$ real at every instant of time. For example $(a+jb)e^{(\sigma-j\omega)t}+(a-jb)e^{(\sigma+j\omega)t}$ has the form $e^{\sigma t}\sin(\omega t+\theta)$, which represents a damped sinusoid for negative σ.

The real component of the eigenvalues gives the damping, and the imaginary component gives the frequency of oscillation. A negative real part represents a damped oscillation whereas a positive real part represents oscillation of increasing amplitude. Thus for a complex pair of eigenvalues:

$$\lambda_i = \sigma \pm j\omega \tag{4.3.12}$$

The frequency of oscillation in Hz is given by

$$f = \frac{\omega}{2\pi} \tag{4.3.13}$$

This represents the actual or damped frequency. The damping ratio is given by

$$\zeta = \frac{-\sigma}{\sqrt{\sigma^2+\omega^2}} \tag{4.3.14}$$

The damping ratio ζ determines the rate of decay of the amplitude of the oscillation. The time constant of amplitude decay is $1/|\sigma|$. In other words, the amplitude decays to $1/e$ of the initial amplitude in $1/|\sigma|$ seconds or in $1/2\pi\zeta$ cycles of oscillation.

The stability status can be judged from eigenvalue of matrix A according to Table 4.1.

4.3.2 Case studies

In this section, case studies are carried out based on the system linearized around an operation point and the eigenvalue analysis of the matrix A, for assessing the

Table 4.1: Behaviors for different eigenvalues

Eigenvalues (λ_i)	solution of differential equation	Stability status
positive real root $\lambda_i = \sigma$	$\Delta\delta = ce^{\sigma t}$	non-periodic unstable
negative real root $\lambda_i = -\sigma$	$\Delta\delta = ce^{-\sigma t}$	non-periodic stable
conjugate imaginary root $\lambda_i = \pm j\beta$	$\Delta\delta = c\sin(\beta t + \varphi)$	continuous oscillation
complex root with positive real part $\lambda_i = \gamma \pm j\theta$	$\Delta\delta = c\sin(\theta t + \varphi)e^{\gamma t}$	unstable oscillation
complex root with negative real part $\lambda_i = -\gamma \pm j\theta$	$\Delta\delta = c\sin(\theta t + \varphi)e^{-\gamma t}$	stable damping oscillation

small-signal stability of the system.

Realization of MPPT

In order to harvest the maximum amount of energy from the wind, the wind turbine must have a specific rotational speed to maintain its tip-speed ratio λ as close as possible to its optimal value λ_{opt}, this concept is well-known as MPPT. In Figure 4.10 a series of wind step change $v_{wind} = 7 - 11[m/s]$ are tested to show the control performance of FLC, the smoother and faster tracking capability within different wind speed manifests its significant superiority in MPPT, which can be clearly explained by the inherent characteristic of the system mode.

To begin with, Table 4.2 gives the system eigenvalues under nominal operation point. Poles $\lambda_{1,2}$, $\lambda_{3,4}$ and λ_5 represent the stator, rotor fluxes and mechanical mode respectively. Here $\lambda_i = \sigma_i \pm j\omega_i$, σ_i determines the i^{th} mode evolution speed while ω_i determines the corresponding oscillation frequency. In the stator flux mode FLC is thoroughly independent and $\omega_{1,2} = 0$ means a non-oscillatory characteristic, while in rotor flux mode both strategies are of the similar conjugative form, at last the smaller σ_5 can definitely provide more damping to system.

By varying the system operation point the system mode loci can now be obtained. The single most striking observation to emerge from Figure 4.3 is that ψ_{qs} mode of FLC is invariant under varying operation range, which can be interpreted

as the fully decoupled control by coefficient α_2 after feedback linearization. Since electrical modes are of interest in this paper, and for the sake of illustration succinctness only e_{qs} and i_{qs} modes are given in the following section.

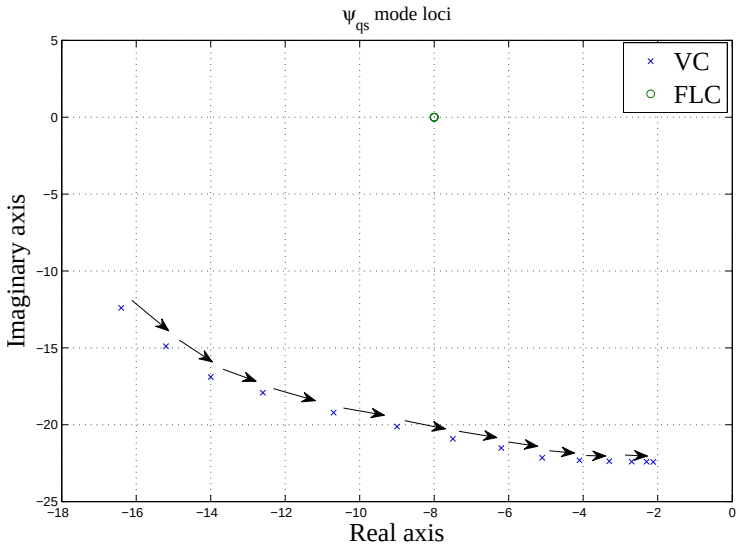

Figure 4.3: ψ_{qs} mode loci under time-varying wind speed

Figures 4.4 and 4.5 describe the mode trajectory of two control strategies during MPPT process. In both modes the FLC varies insignificantly which amounts to tiny active power variation. In Figures 4.13 and 4.14 the dramatic variation of VC active power in the low-speed wind range manifests its shortage in the face of varying operation range, furthermore by tracking the optimal rotational speed after wind step change, the net power output condition $P_m - P_e > 0$ must be satisfied to obtain an increasing ω_r, however, due to the mechanical constraint P_m could not increase immediately and a temporary drop in P_e has to be compromised to provide the required accelerating torque. Needless to say the invariant reactive power is the direct result from ψ_{qs} mode.

Examination of internal dynamics stability

By means of input-output linearization, the dynamics of a nonlinear system is decomposed into an external (input-output) part and an internal (”unobservable”) part. The external part consists of a linear relation between output y and input v

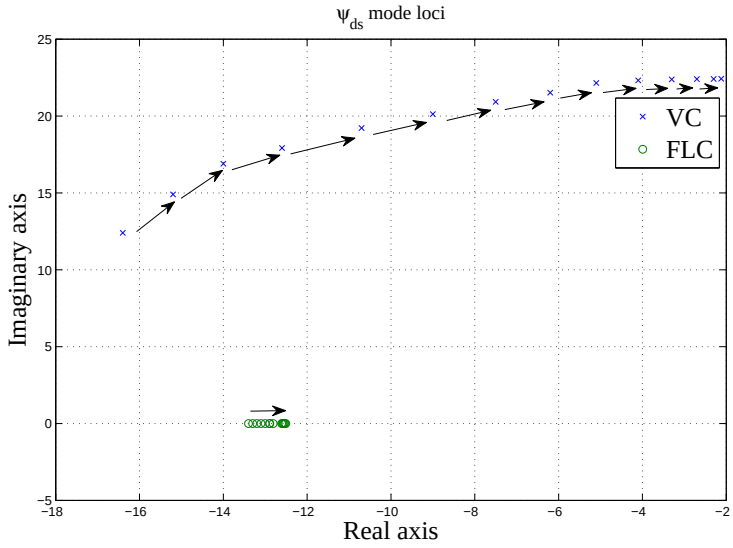

Figure 4.4: ψ_{ds} mode loci under time-varying wind speed

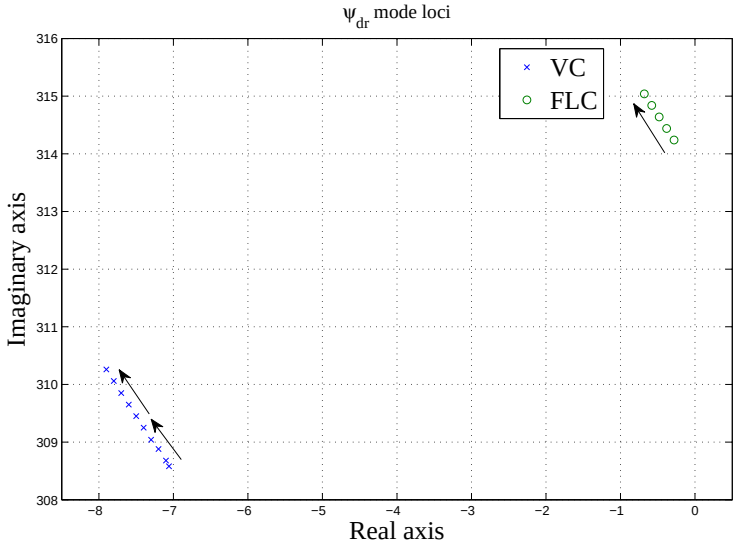

Figure 4.5: ψ_{dr} mode loci under time-varying wind speed

Table 4.2: Eigenvalues under nominal operation point

poles	state variables	VC	FLC
$\lambda_{1,2}$	ψ_{ds},ψ_{qs}	$-2.12 \pm j22.42$	-12.51,-8
$\lambda_{3,4}$	ψ_{dr},ψ_{qr}	$-7.06 \pm j308.48$	$-0.28 \pm j314.34$
λ_5	ω_r	-0.01	-2

so it is easy to design v so that y behaves as desired, however the control design must account for the whole dynamics and therefore cannot tolerate the instability of internal dynamics and the internal behavior has to be addressed carefully.

One can readily find the internal states correspond to $n - r$, here $n = 5$ and $r = 3$ are the system order and total relative degree respectively, these two internal dynamics may have a deleterious effect on the system stability and must be examined carefully during design. Encouragingly since all the system modes loci stayed at the left-half plane(LHF) in Figures 4.3 to 4.5, the internal dynamics stability could be uncovered and this fact corroborates the feasibility of FLC design.

Capability of low-voltage ride through

With the unprecedented increasing integration of wind generators into grid, it is required the DFIG to be capable of LVRT when the voltage is temporarily reduced due to a fault or load change in the grid, some gird codes even address the generator to stay operational and not disconnect from the grid during and after the dip.

To test the LVRT capacity a $300ms$ voltage dip from $1.0v_s$ to $0.5v_s$ occurred and restored to $1.0v_s$ thereafter. It is apparent in Figure 4.6 that for the ψ_{ds} mode FLC trajectory moves much slower than VC, similar results are obtained in the fashion of the ψ_{dr} mode. From Figure 4.7 the severe oscillatory curve in VC active and reactive power can be explained as the large excursion of $\omega_{3,4}$ in current mode, unfortunately, this undesirable feature might lead the relay system activation and disconnect the generator from the grid. Again FLC can perfectly regulate the reactive power as the desired value.

Robustness of parameter uncertainty

It is important to mention that the effect of system sensitivity to parameter uncertainty may be particularly severe when the linearizing transformation is poorly conditioned. In practise the accurate system information is not accessible, and can have strong adverse effects on FLC which does not guarantee robustness in theory.

Since the requirement of exact generator parameter is impossible to achieve, expectantly the modal analysis would be effective to address this issue. Figures

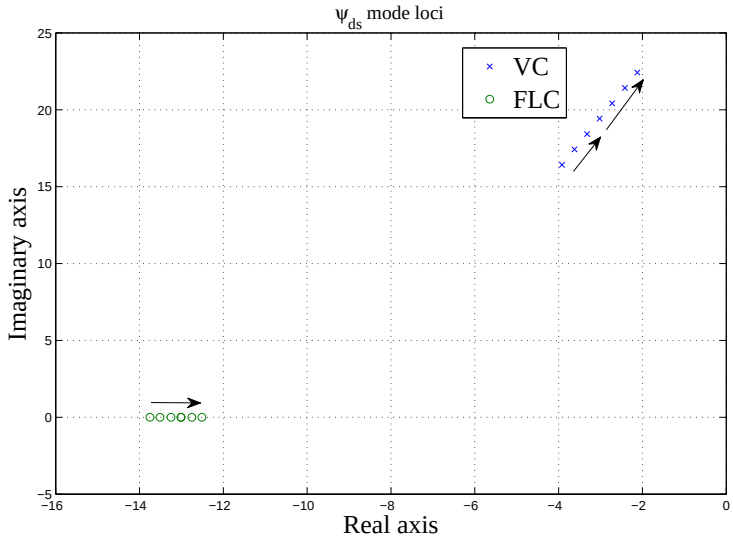

Figure 4.6: ψ_{ds} mode loci under grid disturbance

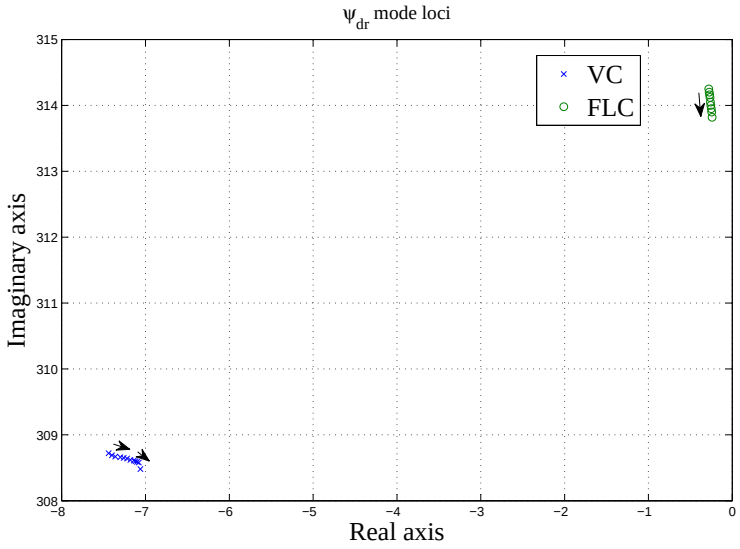

Figure 4.7: ψ_{dr} mode loci under grid disturbance

4.8 and 4.9 provide the system mode loci with varied rotor resistance $1.5R_{r\_nom} \geq R_r \geq 1.0R_{r\_nom}$, which is quite common as internal generator heating, the significant variation can be observed and undoubtedly indicates the vulnerability of FLC to parameter uncertainty. Moreover, if $R_r \geq 1.25R_{r\_nom}$ ψ_{dr} mode loci moves into right-half plane(RHP) and the system stability collapsed completely. In contrast none of the generator parameter is needed in VC thus its operation performance preserved. Figures 4.30 and 4.31 illustrate the active and reactive power evolution of FLC with different R_r values, the unbounded output power is obviously resulted from the ψ_{dr} mode entering into RHP.

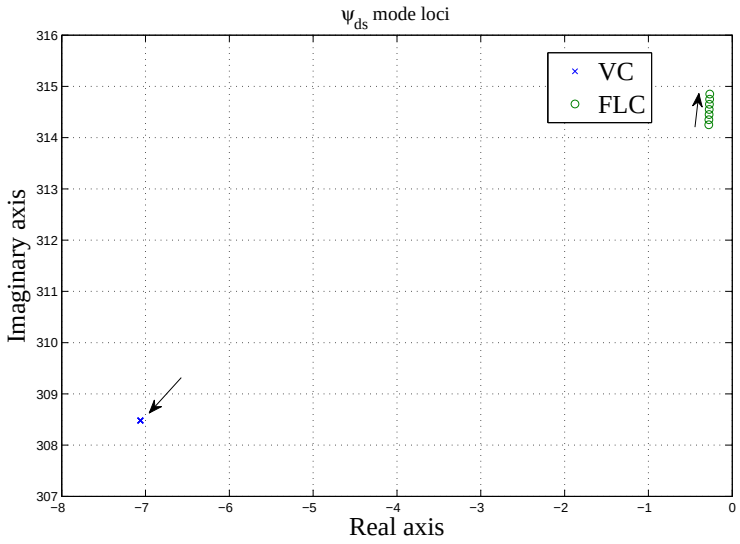

Figure 4.8: ψ_{ds} mode loci under parameter uncertainty

4.4 Simulation studies

In order to verify the effectiveness of the proposed FLC method, case studies based on a GE 3.6 MW DFIG-WT with the FLC are carried out in this section. The MPPT based on the conventional PI-based VC is also tested to compare with the proposed method. The parameters of the DFIG-WT tested are listed as following: $R_s = 0.0079$ pu, $R_r = 0.025$ pu, $L_{ls} = 0.7937$ pu, $L_m = 4.4$ pu, $L_{lr} = 0.40$ pu, $R_e = 0.014$ pu, $X_e = 0.08$ pu, $H_m = 5.19$ s, $D_m = 0$, the base frequency is $f = 60$

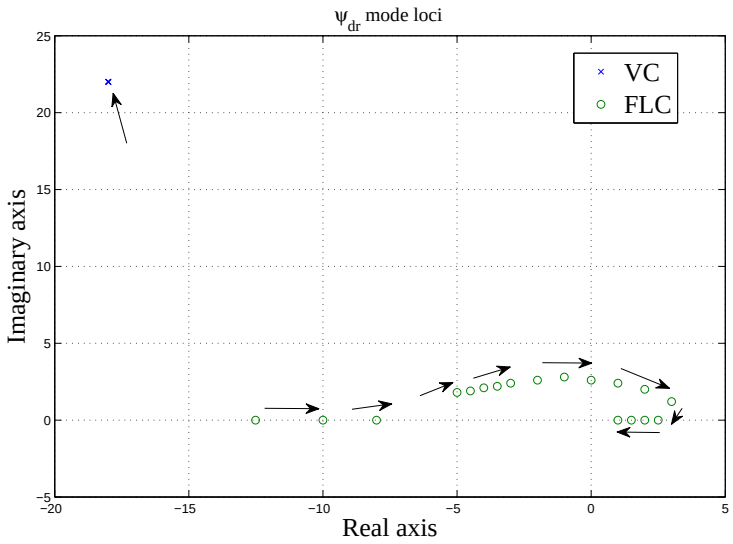

Figure 4.9: ψ_{dr} mode loci under parameter uncertainty

Hz, the rotor diameter of the wind turbine is $d = 104$ m.

The PI parameters of the VC are designed for the case that the wind turbine operates at a specific operating point with wind speed being 8 m/s. The detailed parameters are given as following: For the outer control loop (speed-power control loop), the controller gains are $K_p = 2.0$ and $K_I = 3.0$ for the rotor speed and $K_p = 1.0$ and $K_I = 0.2$ for the stator active power regulation, respectively; for the inner control loop (current control loop), the controller gains of both loops are $K_p = 0.2$ and $K_I = 0$.

The parameters of the FLC, k_{11}, k_{12}, and k_{21} in (4.2.16), are designed based on the pole placement method. The gains are obtained as $k_{11} = 25$, $k_{12} = 10$, and $k_{21} = 5$, by placing the poles of system (4.2.16) at -5.

Three basic types of the disturbance, including step change of wind speed, random change of wind speed, and the parameter uncertainties, are tested and to show the performance on the MPPT under different working conditions. All tests are carried out by using Simulink platform of Matlab 7.10.0 (R2010a) and run on a PC with 2.80 GHz Intel Core i5 CPU, 8GB RAM, and Windows 7 64-bit Ultimate.

4.4.1 Wind speed with large step changes

In order to verify the performance of the proposed FLC method against the large and/or sudden variation of the wind speed, the close-loop system is tested under the wind speed with large step changes, including the increasing and decreasing with different values (1 m/s or 2 m/s), as shown in Figure 4.10. Without loss of generality, it is assumed that those large changes are appearing within 60 seconds to simplify the analysis. In addition, the system is assumed to be operating stably and working at the wind speed of 8 m/s originally. The results obtained from the conventional PI-based VC are also tested to compare with the proposed method.

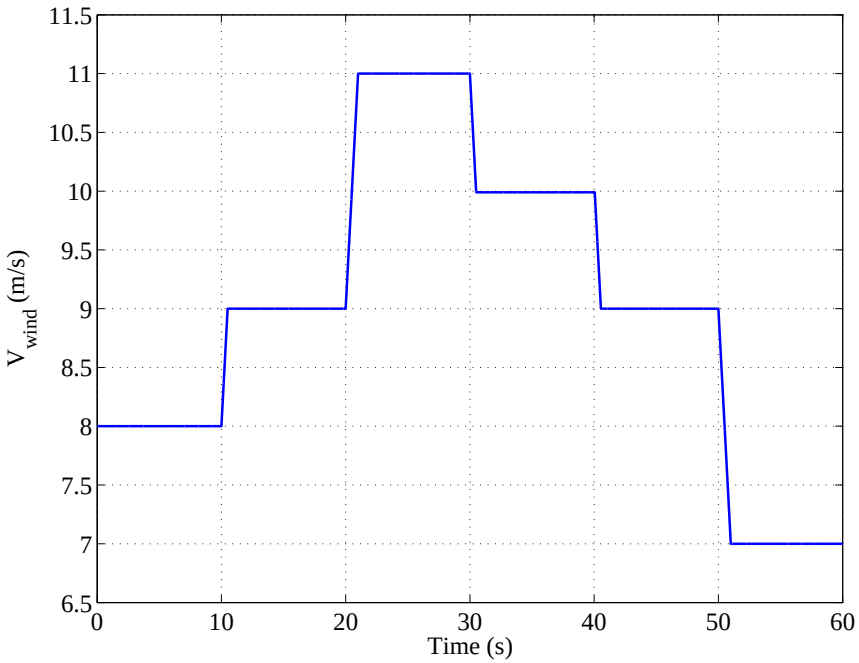

Figure 4.10: Wind speed with large step changes

The power coefficient, C_p, with respect to different wind speed obtained by the VC and FLC is shown in Figure 4.11. where $C_{p\_\max}$ is the maximal power coefficient and it is 0.48 based on the given parameters. From the figure, both the VC and FLC can achieve the maximal power coefficient for the constant wind speed. While the power coefficient, C_p, provided by the VC or the FLC deviates from this maximal value within the time intervals where the speed changes, and the value of deviation for the bigger speed change (2 m/s) is more obvious than that for the

smaller speed change (1 m/s). Moreover, the value of C_p provided by the FLC converges back to its maximal value more quickly than that provided by the VC, and the total time interval, in which the system operates at the maximal power point, is longer when using the FLC. Specifically, within 60 seconds, such time interval for the VC is $T_{vc} = 38$ seconds and that for the FLC is $T_{flc} = 48$ seconds, namely, the system equipped with the VC (or FLC) operates at its highest efficiency condition in the $\frac{38}{60} \times 100\% = 63\%$ (or $\frac{48}{60} \times 100\% = 80\%$) of the whole operating time. Obviously, the FLC can provide a higher efficiency on the wind power conversion.

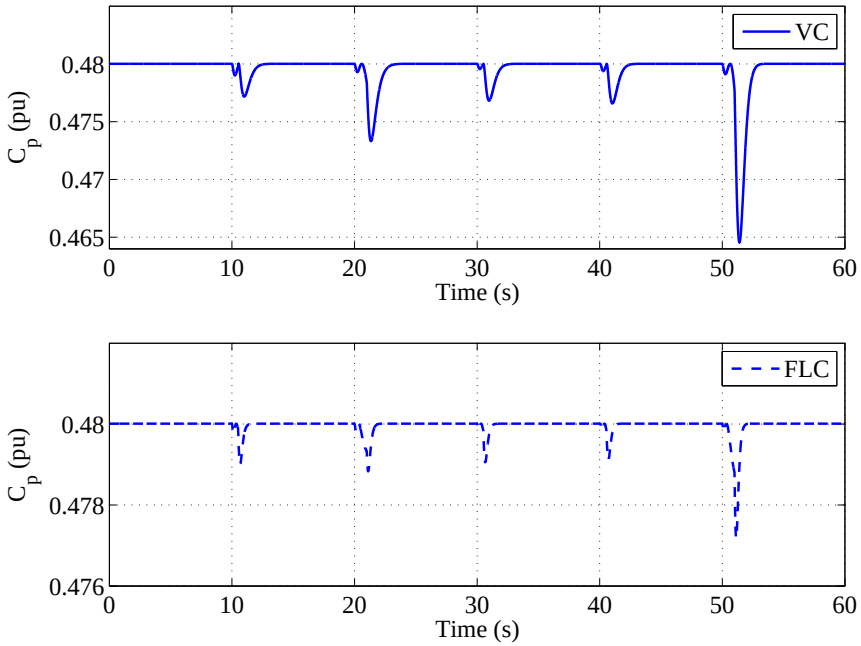

Figure 4.11: The power coefficient and its ITAE under the step change of wind speed

The responses of the rotor speed for the VC and the FLC are given in Figure 4.12(a), where the reference of the rotor speed is the optimal reference value for different wind speed calculated based on (4.1.6). In order to show the difference of the VC and the FLC clearly, the values of the time multiplied absolute value of the error (ITAE) of ω_r is defined as

$$\mathrm{ITAE}_{\omega_r} = \int_0^t t\left(|\omega_r - \omega_{r\_opt}|\right) \mathrm{d}t \tag{4.4.1}$$

The ITAE with respect to different time for the VC and the FLC are shown in Figure

4.12(b), It can be found that there exists an overshoot for the response of the ω_r during the wind speed changes from one value to another value for both the VC and the FLC, and the value of the ω_r provided by the FLC is more close to the optimal reference value than the one provided by the VC.

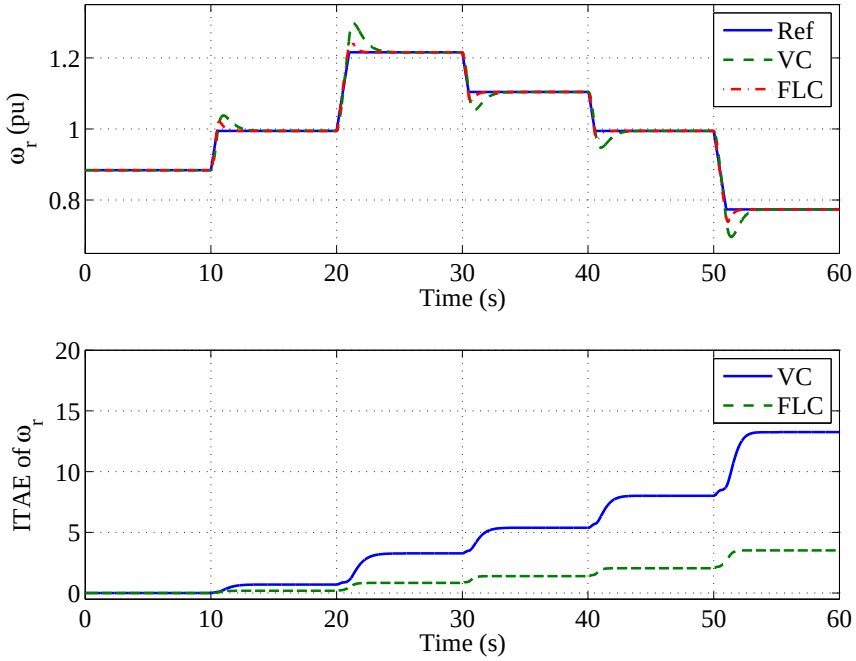

Figure 4.12: The rotor speed and its ITAE under the step change of wind speed

Figure 4.13 shows the responses of the electric power and its ITAE, which is defined as

$$\mathrm{ITAE}_{\mathrm{P_e}} = \int_0^t t\left(|P_e - P_m|\right)\mathrm{d}t \tag{4.4.2}$$

where P_m (i.e., the reference value in figure) is the mechanical power output of the wind turbine for different wind speed. The results that the electric power can track the mechanical power with a small delay and an little overshoot. The overshoot for the VC is a little smaller than that for the FLC, while the FLC can make the electric power track the mechanical power more quickly.

The responses of the stator reactive power for the VC and the FLC are given in Figure 4.14, where the reference value is desired value and equals to zero. The results show that the stator reactive power is controlled to be close to the zero by

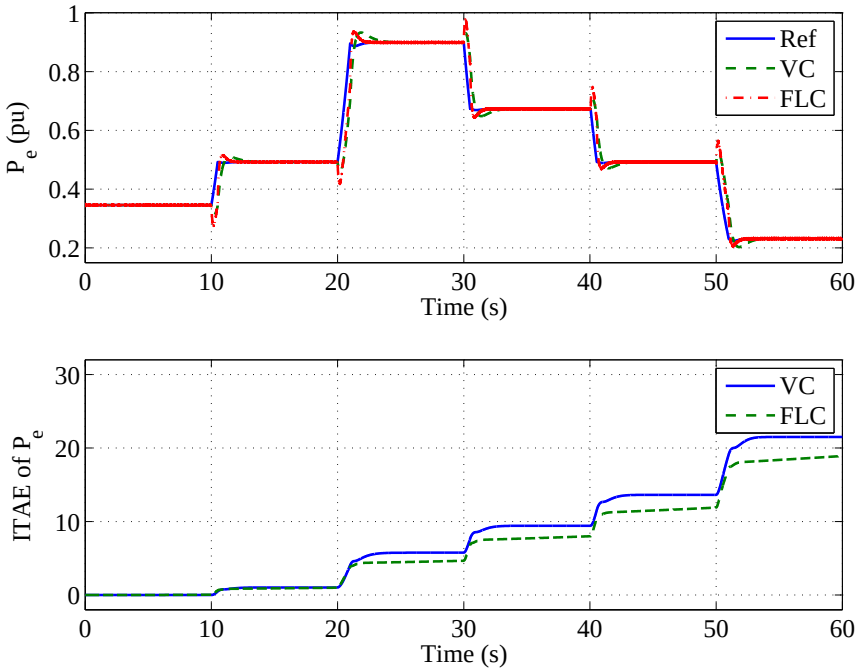

Figure 4.13: The electric power and its ITAE under the step change of wind speed

applying the VC and the FLC, and the value for the FLC (within $\pm 5e-10$) is more close to zero than that (within $\pm 1e-3$) for the VC, which means that the FLC achieves the better performance than the VC does.

The control inputs of the VC and the FLC are presented in Figure 4.15. It is shown that the FLC requires more continual operations.

4.4.2 Wind speed with random changes

In order to verify the performance of the proposed FLC method against the random wind speed around a basic value, which is more common in real world, the close-loop system is tested under the wind speed with bounded random changes, as shown in Figure 4.16. Without loss of generality, it is assumed that the wind speed changes randomly around 8 m/s within 600 seconds. In addition, the controller gains for the conventional PI-based VC is designed for the wind speed of 8 m/s.

The power coefficient, C_p, obtained by the VC and FLC is shown in Figure 4.17. From the figure, both the VC and FLC can provide the power coefficient near to its

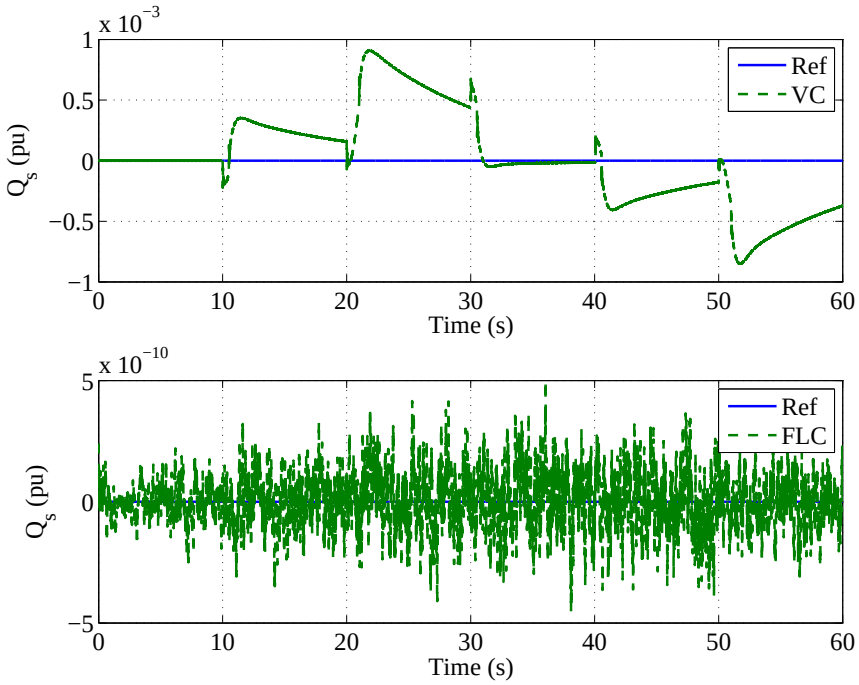

Figure 4.14: The stator reactive power under the step change of wind speed

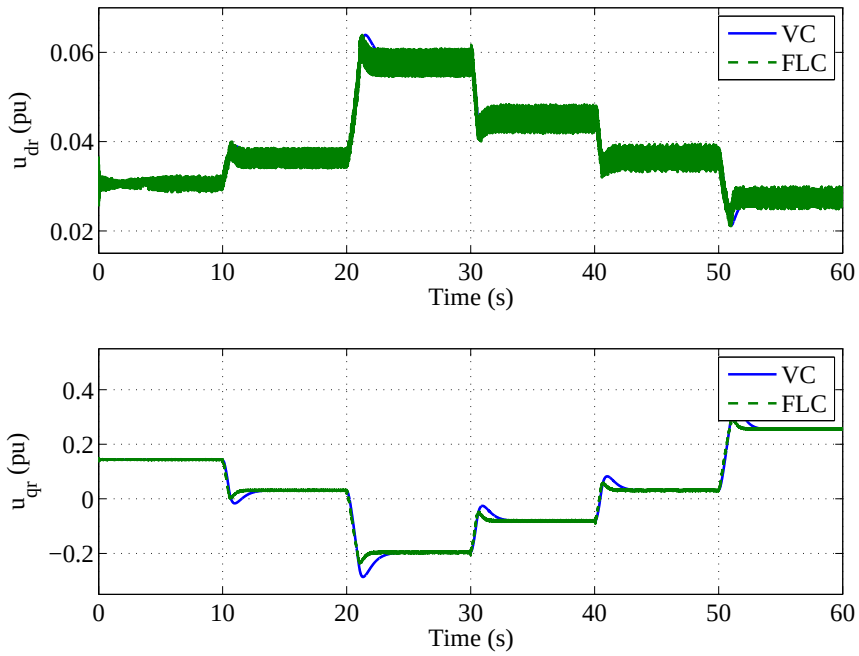

Figure 4.15: The rotor voltage in d- and q-axis under the step change of wind speed

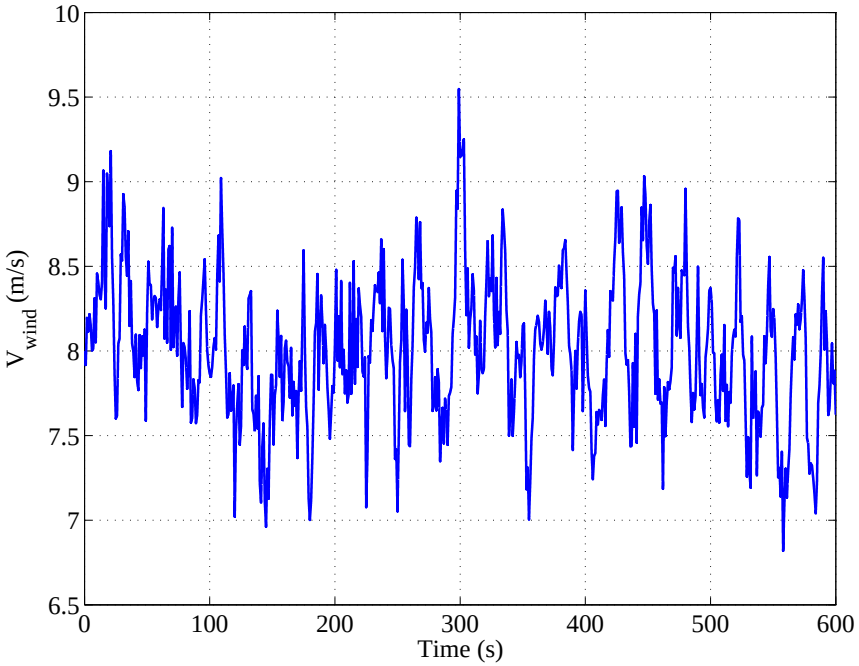

Figure 4.16: Time-varying wind speed

maximal value, 0.48, for different wind speed. The value of C_p provided by the FLC (within [0.4795,0.48]) is closer to this maximal value than the one provided by the VC (within [0.478,0.48]).

The responses of the rotor speed with its ITAE, the electric power with its ITAE, the stator reactive power, and rotor voltage (control input) are shown in Figures 4.18-4.21. From these results, it can be found that the FLC can provide better performance than the VC does for the whole operation interval, such as the smaller tracking errors of the rotor speed (Figure 4.18), the electric power (Figure 4.19), and the stator reactive power (Figure 4.20). Two reasons lead to this phenomenon: 1) the VC is designed based on a linearized system for an special operation point (wind speed is 8 m/s) and it cannot still guarantee the optimal performance when the operation point changes; 2) the proposed FLC is designed based on the original nonlinear system and it has better robustness against the changing of the operation condition.

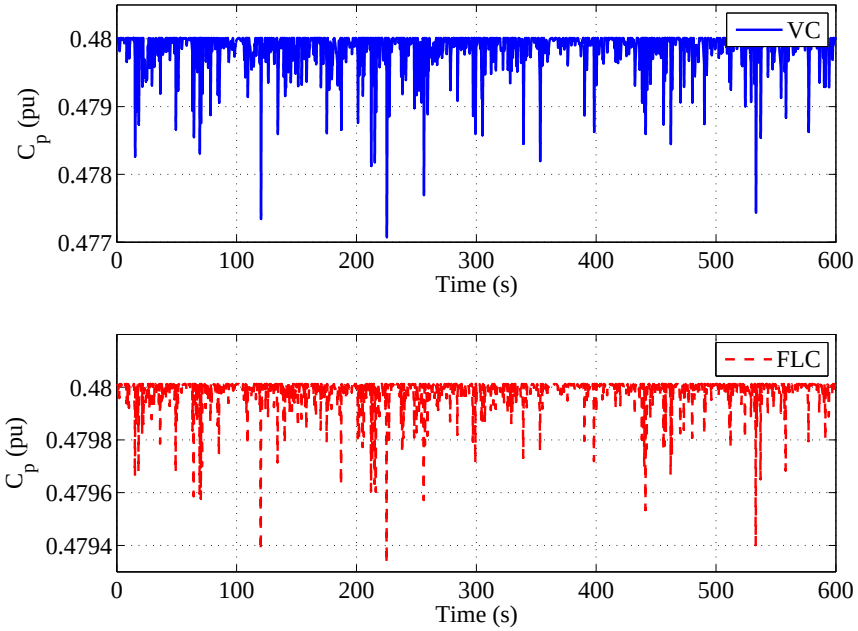

Figure 4.17: The power coefficient under the random wind speed

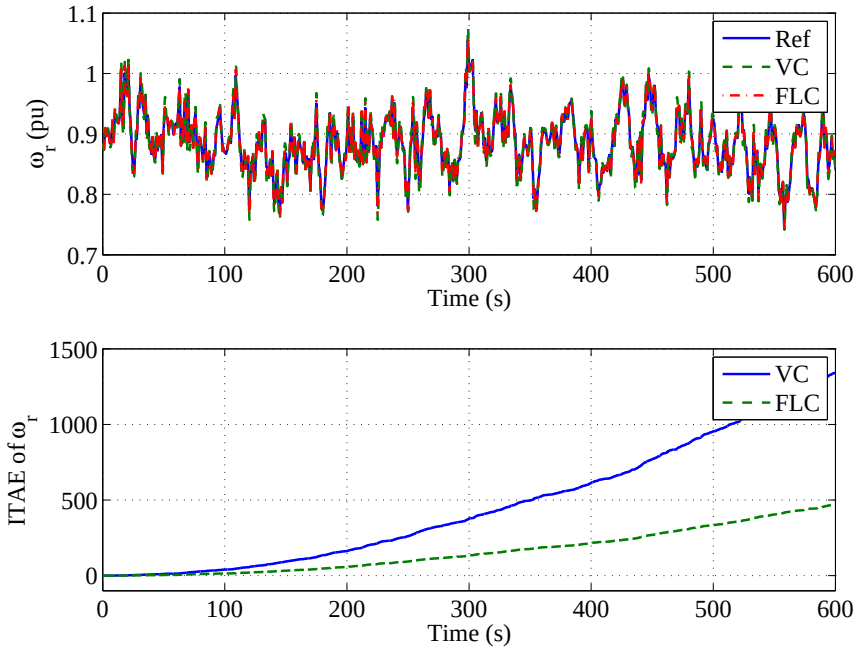

Figure 4.18: The rotor speed under the random wind speed

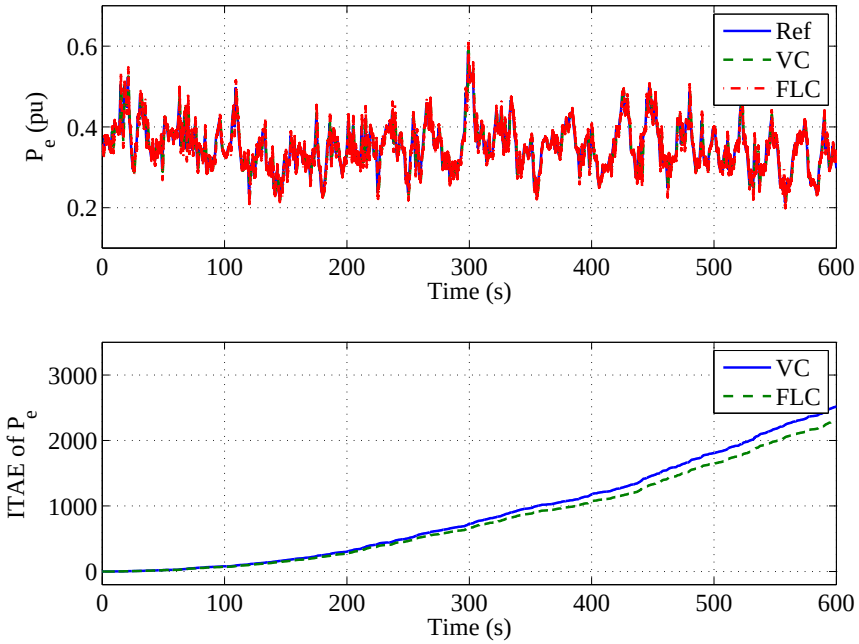

Figure 4.19: The electric power under the random speed

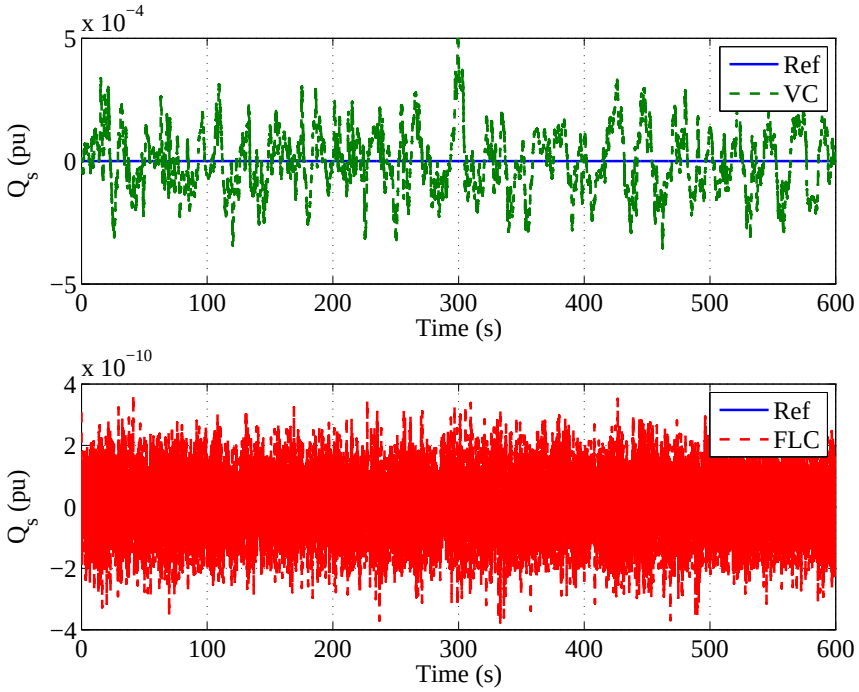

Figure 4.20: The stator reactive power under the random wind speed

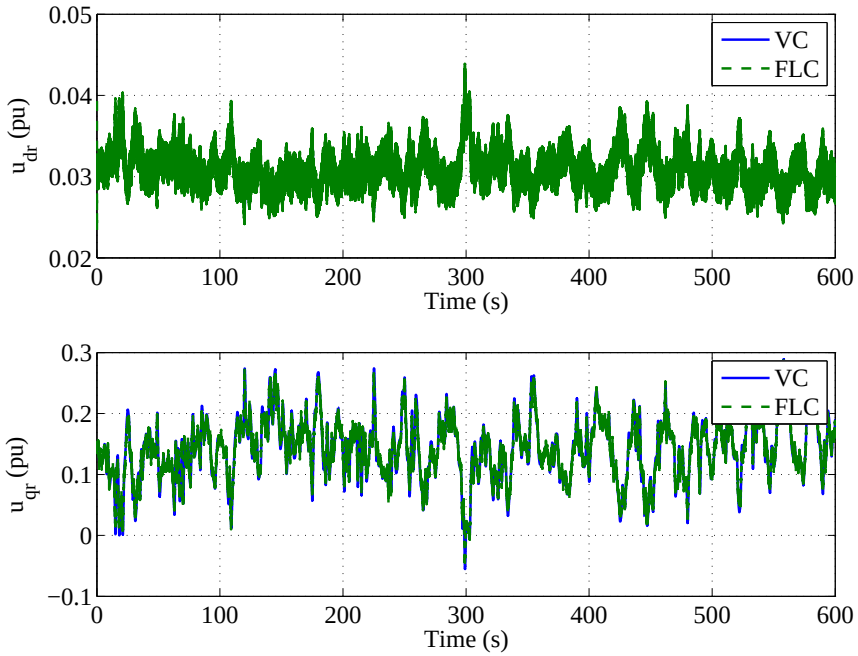

Figure 4.21: The rotor voltage in d- and q-axis under the random wind speed

4.4.3 Low-voltage ride through capability

In order to investigate the low voltage ride through capability of the proposed FLC method, the close-loop system is tested under a grid disturbance. Due to this grid disturbance, the voltage of the stator dips to the 50% of its normal value at $t_1 = 1$ second and lasts 150 ms, and then recovers to the 90% of its normal value, as shown in Figure 4.22. Without loss of generality, it is assumed that the wind speed is constant and is 8 m/s.

The power coefficient, C_p, and its ITAE value obtained by the VC and FLC is shown in Figure 4.23. During the voltage of the stator dips due to the grid disturbance, the value of C_p provided by the FLC is almost constant and equals to the maximal value, while the one provided by the VC obviously deviates from the maximal value. The responses of the rotor speed with its ITAE, the electric power with its ITAE, and the stator reactive power are shown in Figures 4.24-4.26. From these results, it can be found that the FLC has better robustness against the grid disturbance. The reason is that the disturbance changes the operation point of the system.

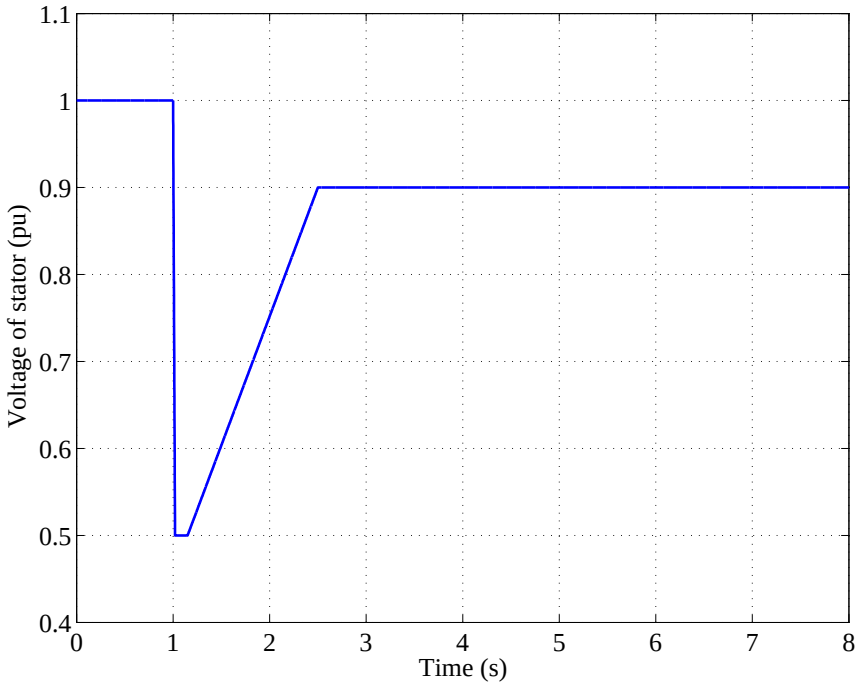

Figure 4.22: The grid disturbance

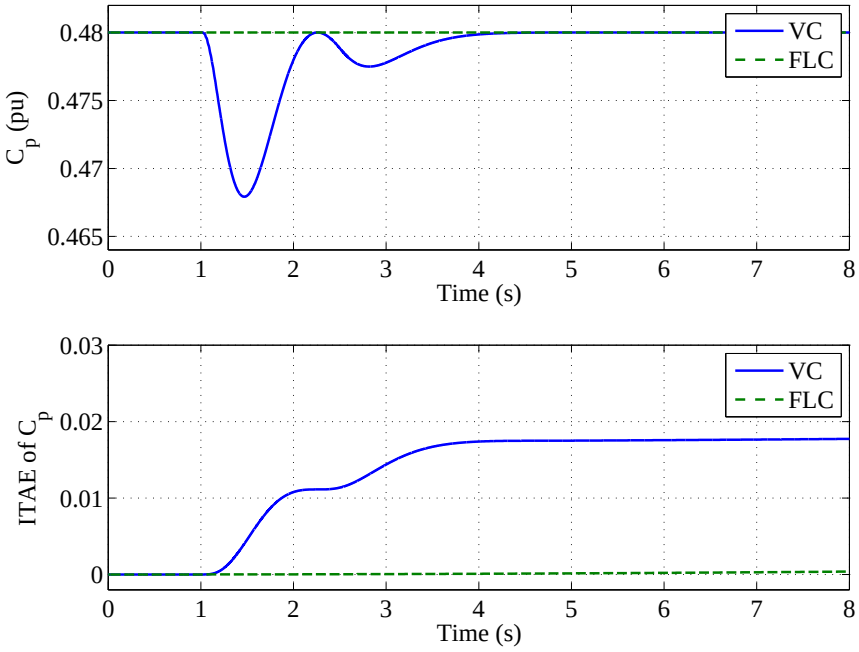

Figure 4.23: The power coefficient under the grid disturbance

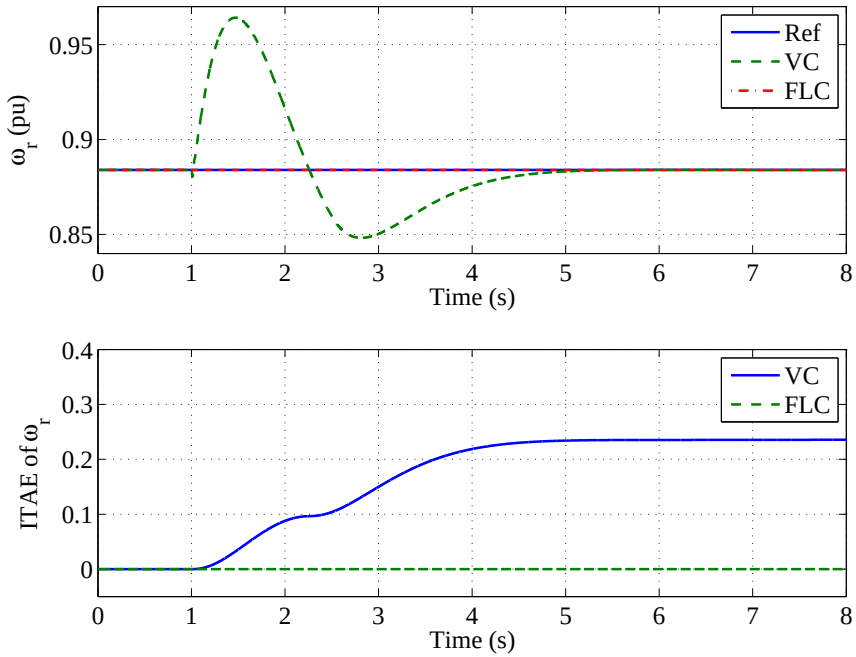

Figure 4.24: The rotor speed under the grid disturbance

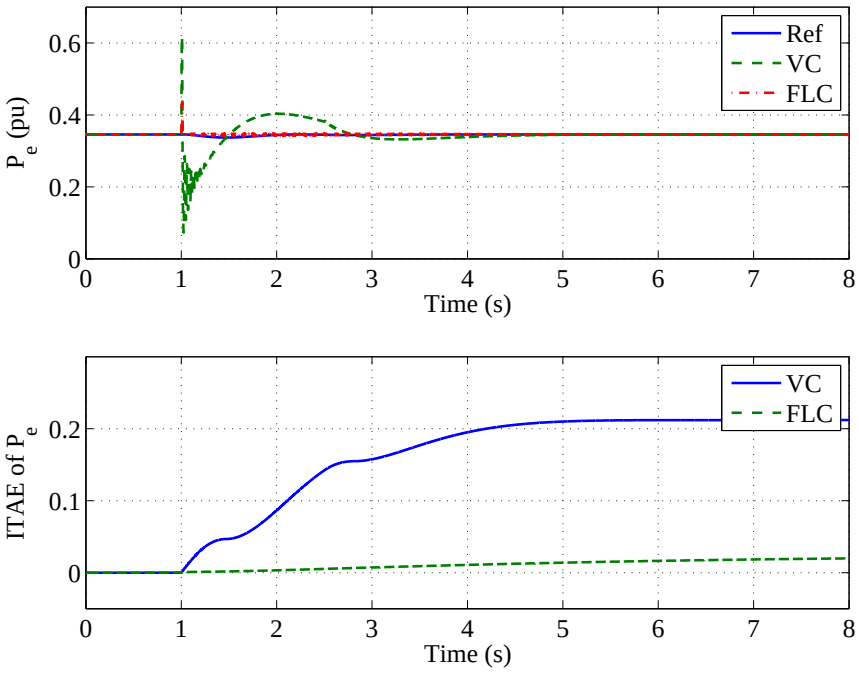

Figure 4.25: The electric power under the grid disturbance

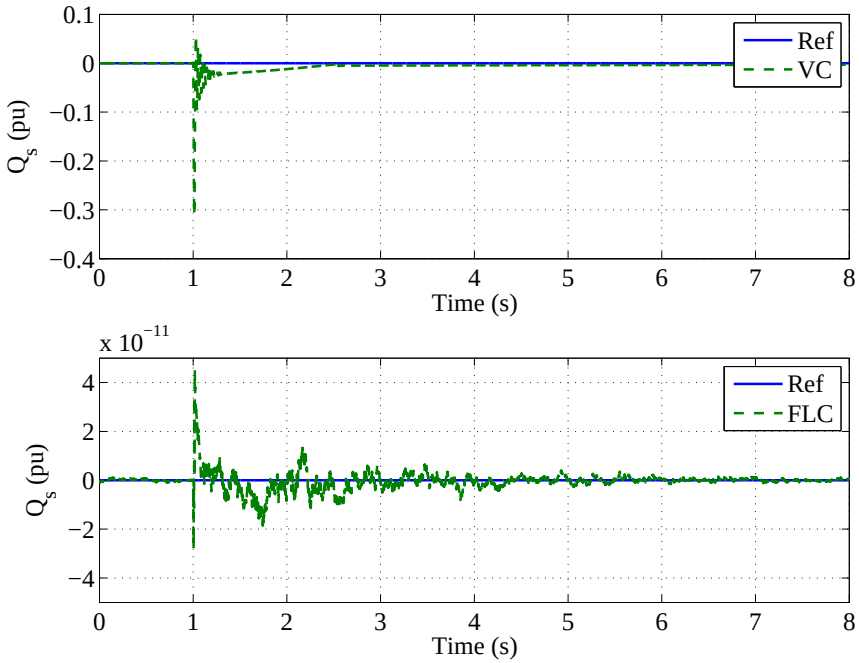

Figure 4.26: The stator reactive power under the grid disturbance

4.4.4 Parameter uncertainty

In order to test the robustness of the proposed FLC method against the parameter uncertainty, the close-loop system is tested for the case that one and/or some of system parameters differ from the normal values. The impact of the changing of the stator resistance, R_r, is investigated in this subsection. The stator resistance may increase with the increase of operating time due to the heating of the devices, the time-varying value of R_r, shown in Figure 4.27, is applied to show such phenomenon without loss of generality. In addition, the wind speed is assumed to be 8 m/s.

The power coefficient, C_p, obtained by the VC and FLC is shown in Figure 4.28. The results show that the value of C_p provided by the VC is almost constant and equals to the maximal value, while the one provided by the FLC obviously deviates from the maximal value. The responses of the rotor speed, the electric power, and the stator reactive power based on the VC and the FLC are shown in Figures 4.29-4.31. From these results, it can be found that the performance of the FLC is seriously influenced by the changing of the stator resistance. All operating

variables, including C_p, ω_r, P_e, and Q_s, deviate from their desired optimal values (reference values in the figures) when the value of R_r is different from the one that applied to design the FLC. The reason is that the design of the FLC has strong connection with such parameter, as shown in (4.2.17). That is to say, the control effort of the FLC is no longer suitable during the value of R_r is different from the one used in the controller. This can be found from the responses of the control input, as shown in Figure 4.32, in which the comparison of the VC and FLC shows that the desired control input and the actual control input of the FLC is inconsistent, for example, from 35 second to 50 second, the desired control input of u_{dr} should be bigger than 0.03 based on the VC, while the actual control input of u_{dr} provided by FLC is smaller than 0.03.

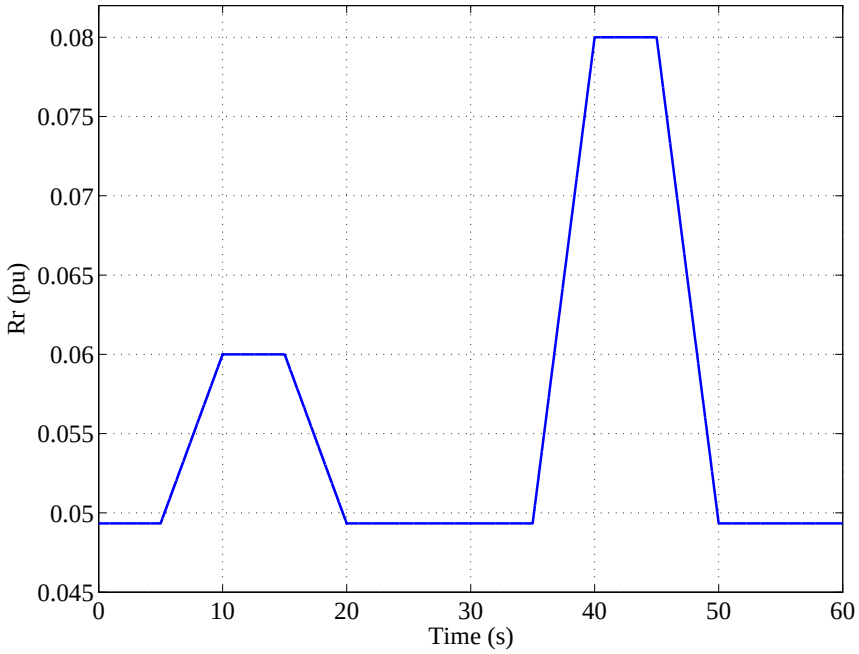

Figure 4.27: The time-varying rotor resistance

4.5 Summary

In this chapter, the nonlinear control design for maximum power power tracking (MPPT) control of DFIG-WT was investigated. The wind turbine operation regions

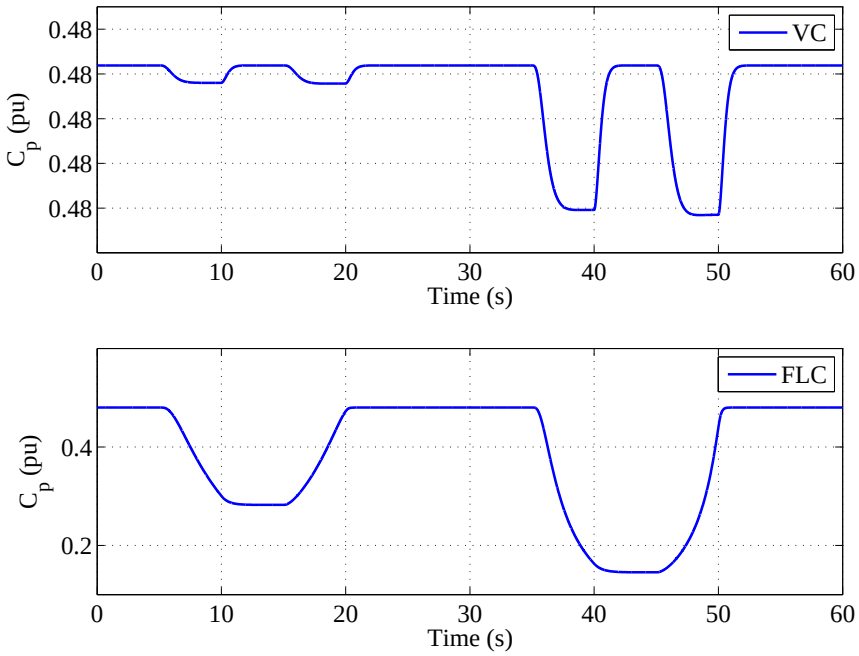

Figure 4.28: The power coefficient under the time-varying rotor resistance

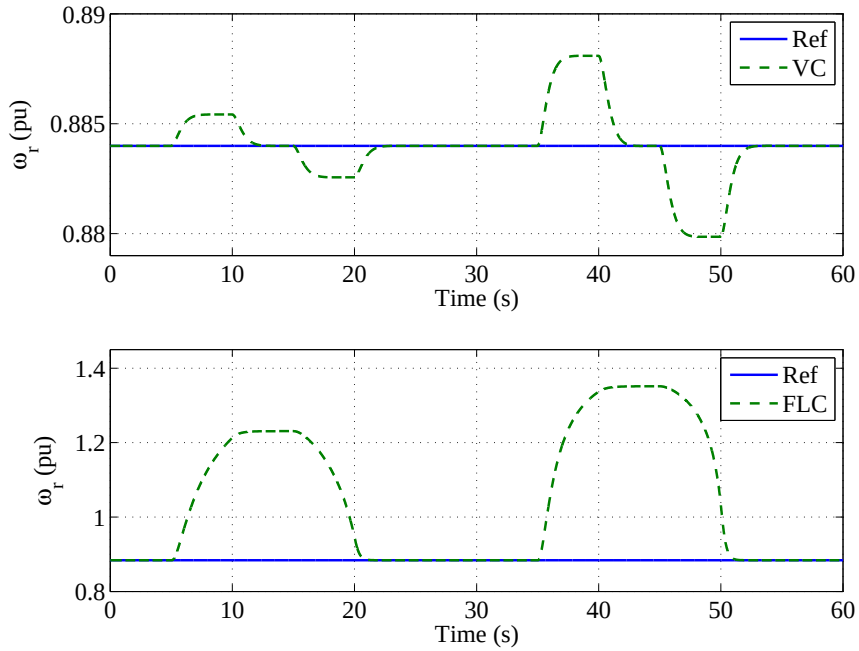

Figure 4.29: The rotor speed under the time-varying rotor resistance

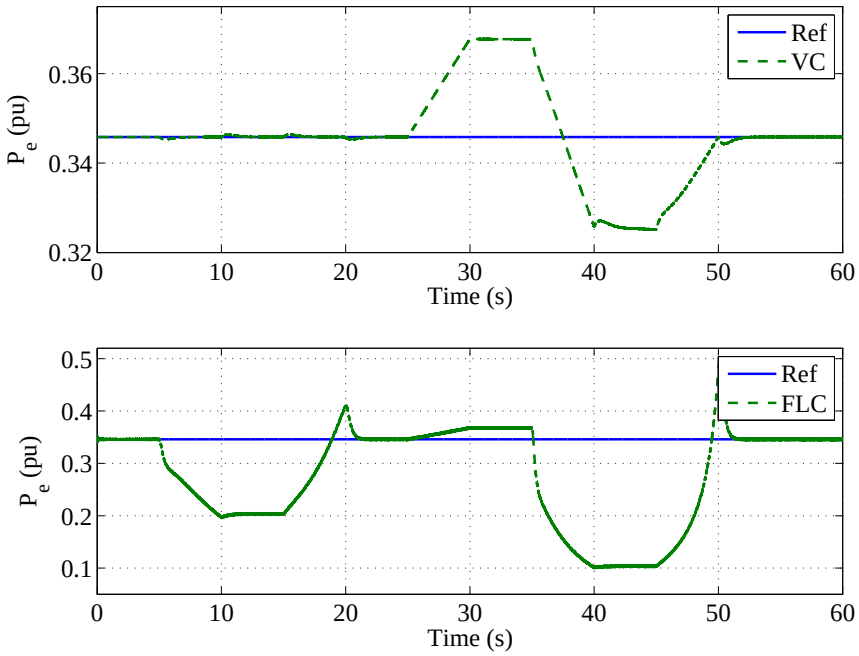

Figure 4.30: The electric power under the time-varying rotor resistance

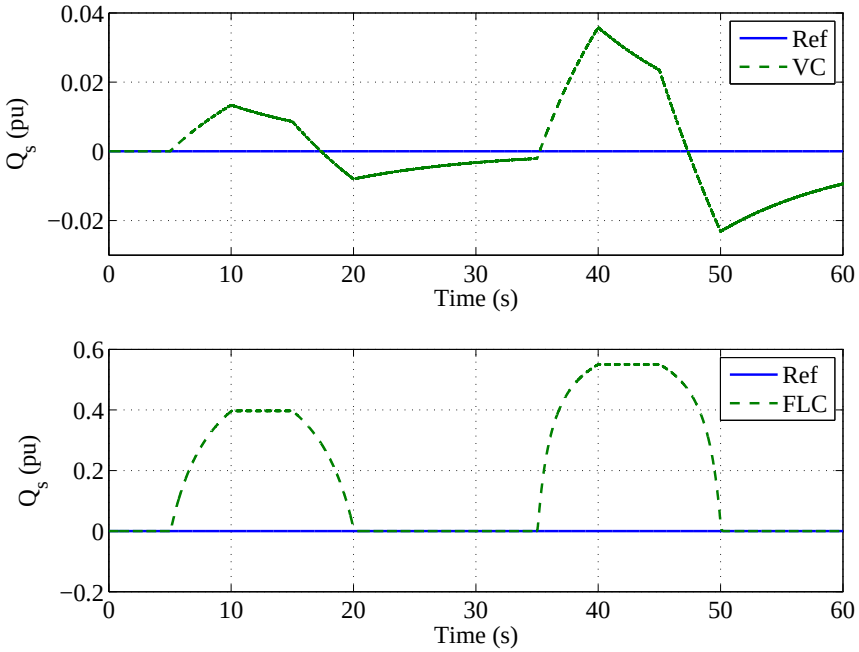

Figure 4.31: The stator reactive power under the time-varying rotor resistance

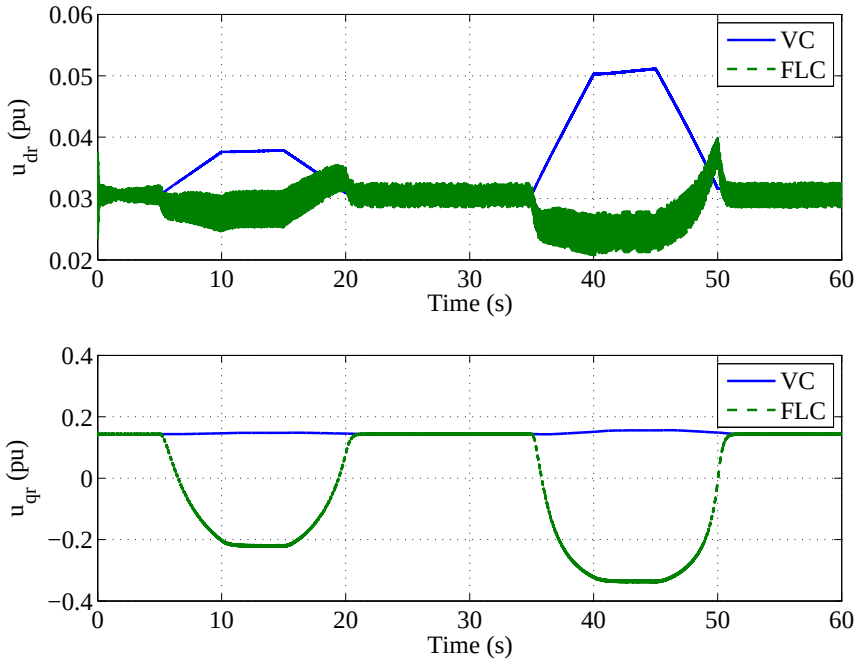

Figure 4.32: The rotor voltage in d- and q-axis under the time-varying rotor resistance

has been reviewed at first, and the MPPT control normally works within the operation range between the cut-in wind speed and the rated one. Moreover, the wind speed was assumed to be measurable for control design in this chapter.

Both VC and FLC were applied for MPPT control under time-varying wind speeds, to achieve the maximum power extraction from the wind power. For mathematical analysis, modal analysis was applied to analysis the dynamics of DFIG-WT provided by VC and FLC respectively, and the results showed that the FLC can provide consistent dynamics with time-varying wind power inputs, although the FLC only achieved partial liearization.

The simulation studies, included wind speed with large step changes, random changes, low-voltage ride through capability and parameter uncertainties, were carried out based on a GE 3.6 MW DFIG-WT connected with an infinite bus. From the results analysis, it showed that the FLC can achieve the global optimal performance, while the wind speed is measurable. However, the FLC can not provide the same performance during the parameter uncertainties, as it depends on the accurate model and parameters of system.

Chapter 5

Nonlinear Adaptive Control for Maximum Power Point Tracking

5.1 Introduction

The model of DFIG-WT belongs to the nonlinear multiple-input multiple-output class, with great nonlinearities existing in the aerodynamics of the WT and the electro-magnetic dynamics of the DFIG. Nonlinear feedback linearization controllers (FLC) has shown an excellent performance in controlling the nonlinear system. This method transforms the original nonlinear system into decoupled linear system, and the controller is performed via linear control laws [81], [82], [83], [84], [85]. It allows nonlinear controllers to be easily designed so that good performance is guaranteed for a wide range of operating points. In [7], the asymptotic regulation of active and reactive power was achieved by means of direct closed-loop control of active and reactive components of the stator current vector, presented in a line-voltage-oriented reference frame. In [**?**], the linear quadratic regulator (LQR) design method was introduced to design the optimal control for the linearized system, and the nonlinear control for DFIG-WT obtained by the inverse coordinate transformation only depends on the parameters of DFIG-WT. All those results require the availability of accurate system models and have more complex control laws than linear methods. In practice, those assumptions are not realistic.

In order to deal with the parameter uncertainties, nonlinear adaptive control has been investigated for DFIG-WT. Nonlinear adaptive controller based on parameter identification has been investigated for DFIG-WT in [35], with the mechanical torque considered as constant. The proposed controller is based on the feedback linearization technique and includes a disturbance observer for estimation of parameter uncertainties. In [34], an adaptive feedback linearization strategy for an WECS with slip power recovery is presented. The proposed adaptive law allows system linearization even in the presence of an imprecise turbine description. Then, the closed-loop dynamic behavior can be determined by a simple tuning of the controller parameters.

5.2 Problem Formulation

Under different wind speed, there exists a maximum output mechanical power P_m, which is mainly related with the turbine shaft speed and the wind velocity. As a result of time-varying wind speed, the rotor speed ω_r can be controlled to make the wind turbine output power reach this value. Thus the maximum power is a function of rotor speed ω_r [44]

$$P_{m\_opt} = K_{opt}\omega_r^3 \tag{5.2.1}$$

and the optimal curve of mechanical torque can be computed by

$$T_{m\_opt} = K_{opt}\omega_r^2 \tag{5.2.2}$$

where the optimal gain K_{opt} is defined as [44]

$$K_{opt} = \frac{1}{2}\rho\pi R^5 \frac{C_{p\_max}}{\lambda_{opt}^3} \tag{5.2.3}$$

According to the equation 2.2.7, the reference of electric torque can be defined as

$$T_{e\_ref} = K_{opt}\omega_r^2 - D_m\omega_r \tag{5.2.4}$$

The curve in Figure 5.1 illustrates the power versus rotor speed characteristics without wind speed measurement. While wind speed varies from V_{wind1} to V_{wind2}, the extracted power increases from point A to B, and $\lambda_B < \lambda_C$ where λ_C is the

optimal tip speed ratio at point C ($C_p > \frac{C_{p\_max}}{\lambda_{opt}^3}\lambda^3$). Then $\dot{\omega}_r > 0$ and the rotor accelerates toward point C. Hence, the power curve without wind speed measurement can be described as the curve P_{opt} from point A to C.

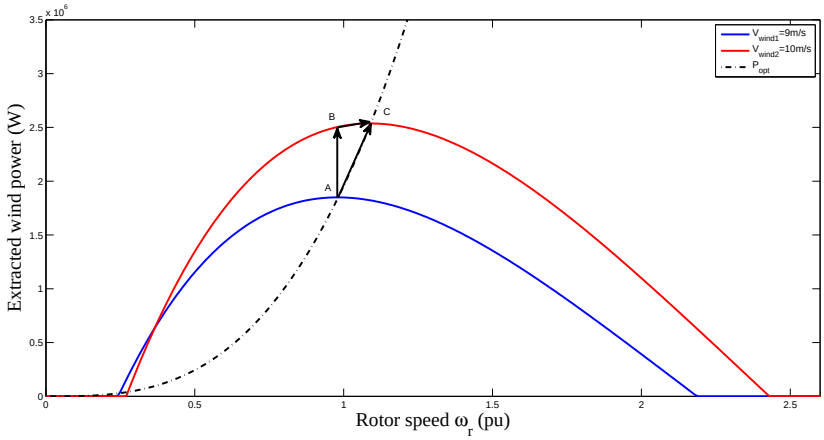

Figure 5.1: The typical power versus speed characteristics without wind speed measurement

This chapter investigates the maximum power point tracking for DFIG-WT by using NAC, considering nonlinear dynamic of the DFIG-WT and unknown and time-varying external wind power inputs simultaneously. The MPPT without wind speed measurement is investigated, following the MPPT with wind speed measurement introduced in Chapter 4. The NAC proposed is designed based on the integrated dynamic model of the wind turbine and the generator together, comparing with the feedback linearization control.

The nonlinear adaptive controller design consists of two cases: case 1, wind speed measurement available, the rotor speed will be controlled to track the optimal reference speed $\frac{\lambda_{opt}V_{wind}}{R}$ to achieve the maximum power coefficient; case 2, without wind speed measurements, the rotor speed will be indirectly adjusted by controlling the electric torque to track the optimal torque reference.

5.3 Nonlinear Adaptive Control based on Perturbation Estimation

The nonlinear adaptive control based on perturbation observer proposed in [86], [87] will be recalled briefly as following steps. A multi-input multi-output (MIMO) system is transformed as interacted subsystems via input/output linearisation at first. Then for each subsystem, a perturbation term is defined to include all subsystem nonlinearities, interactions between subsystems and uncertainties and estimated by designing perturbation observers. The estimates of perturbations are used to compensate the real perturbation and implement an adaptive linearisation and decoupled control of the original nonlinear system.

5.3.1 Input-Output linearization

Consider a MIMO system

$$\begin{cases} \dot{x} = f(x) + g(x)u \\ y = h(x) \end{cases} \tag{5.3.1}$$

where $x \in R^n$ is the state vector, $u \in R^m$ is the control input vector, $y \in R^m$ is the output vector, $f(x)$, $g(x)$ and $h(x)$ are smooth vector fields. The input-output linearisation of a MIMO system is obtained via differentiating the output y_i of the system until the input u_j appears. Thus, assuming that r_i is the smallest integer such that at least one of the inputs explicitly appears in $y_i^{(r_i)}$

$$y_i^{(r_i)} = L_f^{r_i} h_i + \sum_{j=1}^{m} L_{g_j} L_f^{r_i - 1} h_i u_j \tag{5.3.2}$$

where $y_i^{(r_i)}$ is the i^{th}-order derivative of y_i, $L_{g_j} L_f^{r_i-1} h_i(x) \neq 0$ for at least one j. Performing the above procedure for each output y_i yields

$$\begin{bmatrix} y_1^{(r_1)} \\ \vdots \\ y_m^{(r_m)} \end{bmatrix} = \begin{bmatrix} L_f^{r_1} h_1 \\ \vdots \\ L_f^{r_m} h_m \end{bmatrix} + B(x) \begin{bmatrix} u_1 \\ \vdots \\ u_m \end{bmatrix} \tag{5.3.3}$$

$$B(x) = \begin{bmatrix} L_{g_1} L_f^{r_1-1} h_1 & \cdots & L_{g_m} L_f^{r_1-1} h_1 \\ \vdots & \vdots & \vdots \\ L_{g_1} L_f^{r_m-1} h_m & \cdots & L_{g_m} L_f^{r_m-1} h_m \end{bmatrix} \tag{5.3.4}$$

where $B(x)$ is a $m \times m$ control gain matrix. If $B(x)$ is invertible, the feedback linearisation control of the the MIMO nonlinear system can be obtained as

$$u = B(x)^{-1} \left\{ \begin{bmatrix} -L_f^{r_1} h_1 \\ \vdots \\ -L_f^{r_m} h_m \end{bmatrix} + \begin{bmatrix} v_1 \\ \vdots \\ v_m \end{bmatrix} \right\} \tag{5.3.5}$$

where v_i are new inputs of the system. Now the input-output relations are given by

$$y_i^{(r_i)} = v_i \tag{5.3.6}$$

At this point, desired dynamics can be imposed on the system by the new system inputs.

5.3.2 Perturbation observer

Assume all nonlinearities of system (5.3.3) are unknown, and define perturbation terms as

$$\begin{bmatrix} \Psi_1 \\ \vdots \\ \Psi_m \end{bmatrix} = \begin{bmatrix} L_f^{r_1} h_1 \\ \vdots \\ L_f^{r_m} h_m \end{bmatrix} + (B(x) - B_0) \begin{bmatrix} u_1 \\ \vdots \\ u_m \end{bmatrix} \tag{5.3.7}$$

where Ψ_i is the perturbation term, $B_0 = B(x)|_{x=x(0)}$ is the nominal control gain. Then system (5.3.3) can be rewritten as

$$\begin{bmatrix} y_1^{(r_1)} \\ \vdots \\ y_m^{(r_m)} \end{bmatrix} = \begin{bmatrix} \Psi_1(x) \\ \vdots \\ \Psi_m(x) \end{bmatrix} + B_0 \begin{bmatrix} u_1 \\ \vdots \\ u_m \end{bmatrix} \tag{5.3.8}$$

For the i^{th} subsystem, defining state variables as $z_{i1} = y_i, \cdots, z_{ir_i} = y_i^{(r_i-1)}$ and a virtual state to represent the perturbation $z_{i(r_i+1)} = \Psi_i$, the i_{th} subsystem can be

represented as

$$\begin{cases} \dot{z}_{i1} & = & z_{i2} \\ & \vdots & \\ \dot{z}_{ir_i} & = & z_{i(r_i+1)} + B_{0_i} u \\ \dot{z}_{i(r_i+1)} & = & \dot{\Psi}_i \end{cases} \tag{5.3.9}$$

where B_{0_i} is the i^{th} row of the B_0. The perturbation observer has been developed as an important technique for the design of NAC proposed in [86], [87]. Several types of perturbation observers, such as sliding mode observer, high gain observer and linear Lunberger observer have been introduced to obtain the online estimate of the perturbation. High gain observer is introduced in this paper as an example. When all states are available, the perturbation is estimated by a second-order perturbation observer (PO) which use the last state $z_{i(r_i-1)}$ as measurement. A states and perturbation observer (SPO) will be designed to obtain the states and perturbation together when only one system state $z_{i1} = y_i$ is available.

When all states are available, the perturbation is estimated by a second-order perturbation observer (PO) which use the last state z_{ir_i} as measurement as follows

$$\begin{cases} \dot{\hat{z}}_{ir_i} & = & \hat{z}_{i1} + h_{i1}(z_{i1} - \hat{z}_{ir_i}) + B_{0_i} u \\ \dot{\hat{z}}_{i(r_i+1)} & = & h_{i2}(z_{ir_i} - \hat{z}_{ir_i}), \end{cases} \tag{5.3.10}$$

where h_{i1} and h_{i2} are gains of the high gain observer. Throughout this paper, $\hat{z}_{ir_i}$ represents the estimate of z_{ir_i}. By choosing

$$h_{i1} = \frac{\alpha_{i1}}{\epsilon_i}, \quad h_{i2} = \frac{\alpha_{i2}}{\epsilon_i^2}, \tag{5.3.11}$$

where ϵ_i, $0 < \epsilon_i < 1$ is a positive constant to be specified and the positive constants α_{ij}, $j = 1, 2$, are chosen such that the roots of

$$s^2 + \alpha_{i1} s + \alpha_{i2} = 0 \tag{5.3.12}$$

are in the open left-half complex plan.

When only the system output $y_i = z_{i1}$ is available, a $(r_i + 1)^{th}$-order state and perturbation observer (SPO) can be designed to estimate the system states and per-

turbation as

$$\begin{cases} \dot{\hat{z}}_{i1} & = & \hat{z}_{i2} + h_{i1}(z_{i1} - \hat{z}_{i1}) \\ & \cdots & \\ \dot{\hat{z}}_{ir_i} & = & \hat{z}_{ir_i} + h_{ir_i}(z_{i1} - \hat{z}_{i1}) + B_{0_i}u \\ \dot{\hat{z}}_{i(r_i+1)} & = & h_{i(r_i+1)}(z_{i1} - \hat{z}_{i1}), \end{cases} \tag{5.3.13}$$

where $h_{ij} = \frac{\alpha_{ij}}{\epsilon_i^j}$, $j = 1, \cdots, r_i+1$ are gains of the high gain observer, ϵ_i, $0 < \epsilon_i < 1$ is a positive constant to be specified and the positive constants $\alpha_{ij}, j = 1, \cdots, r_i+1$, are chosen such that the roots of

$$s^{r_i+1} + \alpha_{i1}s^{r_i} + \cdots + \alpha_{ir_i}s + \alpha_{i(r_i+1)} = 0 \tag{5.3.14}$$

are in the open left-half complex plan.

5.3.3 Design of NAC controller

Using the estimate of perturbation $\hat{\Psi}_i = \hat{z}_{i(r_i+1)}$ to compensate the real system perturbation, the control law of the NAC can be obtained as

$$u = B_0^{-1}\left\{\begin{bmatrix} -\hat{\Psi}_1 \\ \vdots \\ -\hat{\Psi}_m \end{bmatrix} + \begin{bmatrix} v_1 \\ \vdots \\ v_m \end{bmatrix}\right\} \tag{5.3.15}$$

where $v_i = -K_i z_i$ is the state feedback control of the i^{th} linear system when a PO is designed, or an output feedback $v_i = -K_i\hat{z}_i$ when a SPO is designed. $K_i = [k_{i1}, \cdots, k_{i(r_i-1)}]^T$ are the linear feedback controller gains which can be determined via linear system method.

5.4 Controller Design

5.4.1 With wind speed measurement

Feedback linearization Control

Choose the rotor speed ω_r and stator reactive power Q_s as the controlled outputs:

$$\begin{cases} y_1 = \omega_r \\ y_2 = Q_s \end{cases} \tag{5.4.1}$$

Let ω_{r_opt} and Q_{s_ref} be the given references of the rotor speed and reactive power, and define the tracking error $e = [e_1 \;\; e_2]^T$ as:

$$e = \begin{bmatrix} e_1 \\ e_2 \end{bmatrix} = \begin{bmatrix} \omega_r - \omega_{r\_opt} \\ Q_s - Q_s^* \end{bmatrix} \tag{5.4.2}$$

The input/output feedback linearization of equation (4.1.1) can be obtained as:

$$\begin{bmatrix} \ddot{e}_1 \\ \dot{e}_2 \end{bmatrix} = \begin{bmatrix} f_1 - \ddot{\omega}_{r\_opt} \\ f_2 - \dot{Q}_s^* \end{bmatrix} + B(x) \begin{bmatrix} u_{dr} \\ u_{qr} \end{bmatrix} \tag{5.4.3}$$

where

$$\begin{aligned} f_1 = {} & \tfrac{\dot{T}_m}{2H_m} - \tfrac{1}{2H_m}((-u_{qs} + R_s i_{qs} + \omega_s \psi_{ds})(\tfrac{L_r}{L_\sigma}\psi_{ds} + i_{ds}) \\ & + (u_{ds} - R_s i_{ds} + \omega_s \psi_{qs})(i_{qs} + \tfrac{L_r}{L_\sigma}\psi_{qs}) - \tfrac{L_m}{L_\sigma}\psi_{ds}(R_r i_{qr} \\ & + (\omega_s - \omega_r)\psi_{dr}) - \tfrac{L_m}{L_\sigma}\psi_{qs}(-R_r i_{dr} + (\omega_s - \omega_r)\psi_{qr})) \end{aligned} \tag{5.4.4}$$

$$\begin{aligned} f_2 = {} & u_{qs}\tfrac{L_m}{L_\sigma}(-R_r i_{dr} + (\omega_s - \omega_r)\psi_{qr}) - u_{qs}\tfrac{L_r}{L_\sigma}(u_{ds} - \\ & R_s i_{ds} + \omega_{qs}) - u_{ds}\tfrac{L_m}{L_\sigma}(-R_r i_{qr} - (\omega_s - \omega_r)\psi_{dr}) + \\ & u_{ds}\tfrac{L_r}{L_\sigma}(u_{qs} - R_s i_{qs} - \omega_s \psi_{ds}) \end{aligned} \tag{5.4.5}$$

and

$$B(x) = \begin{bmatrix} \frac{L_m}{2H_m L_\sigma}\psi_{qs} & -\frac{L_m}{2H_m L_\sigma}\psi_{ds} \\ \frac{L_m}{L_\sigma}u_{qs} & -\frac{L_m}{L_\sigma}u_{ds} \end{bmatrix} \tag{5.4.6}$$

where $B_0(x) = B(x)|_{L_m = L_{m0}}$, $\Delta B(x) = B(x) - B_0(x)$. Note that when $det(B) = 0.5\frac{L_m^2}{H_m L_\sigma^2}(-\psi_{qs}u_{ds} + \psi_{ds}u_{qs}) \neq 0$, system (5.4.3) can be linearized as following

$$\begin{bmatrix} \ddot{e}_1 \\ \dot{e}_2 \end{bmatrix} = \begin{bmatrix} v_1 \\ v_2 \end{bmatrix} \tag{5.4.7}$$

where $v = [v_1 \;\; v_2]^T$ is the control input of the linear system defined as

$$\begin{bmatrix} v_1 \\ v_2 \end{bmatrix} = \begin{bmatrix} -k_{11}e_1 - k_{12}\dot{e}_1 \\ -k_{21}e_2 \end{bmatrix} \tag{5.4.8}$$

where k_{11}, k_{12}, k_{21} are the feedback gains.

Then the FLC control law of equation (4.1.1) can be obtained as follows

$$\begin{bmatrix} u_{dr} \\ u_{qr} \end{bmatrix} = B(x)^{-1}\left(\begin{bmatrix} -f_1 + \ddot{\omega}_{r\_opt} \\ -f_2 + \dot{Q}_{s\_ref} \end{bmatrix} + v \right) \tag{5.4.9}$$

Nonlinear adaptive control

FLC control law (5.4.9) assumes all states and parameters are known accurately and is very complex. Moreover, in [35], [**?**], $\dot{T}_m$ is equal to zero, as T_m is assumed be constant during the transient period, which is correspond to constant wind speed.

Based on equation (5.4.3), perturbations $\Psi_1(x)$ and $\Psi_2(x)$ are defined as

$$\begin{cases} \Psi_1(x) &= f_1(x) - \ddot{\omega}_{r\_ref} + \Delta B(x)_{11}u_1 + \Delta B(x)_{12}u_2 \\ \Psi_2(x) &= f_2(x) - \dot{Q}_{s\_ref} + \Delta B(x)_{11}u_1 + \Delta B(x)_{12}u_2 \end{cases} \tag{5.4.10}$$

where $u_1 = u_{dr}$, $u_2 = u_{qr}$.

Note that $\Delta B(x)$ represents parameter uncertainties of control gains.

Defining the state vectors $z_{11} = y_1, z_{12} = \dot{y}_1, z_{13} = \Psi_1(x)$, $z_{21} = y_2, z_{22} = \Psi_2(x)$. Dynamic equations of the subsystems q_1 and q_2 are described as follows:

$$\begin{aligned} q_1 : & \begin{cases} \dot{z}_{11} &= z_{12} \\ \dot{z}_{12} &= z_{13} + B_0(x)_{11}u_1 + B_0(x)_{12}u_2 \\ \dot{z}_{13} &= \dot{\Psi}_1(x) \end{cases} \\ q_2 : & \begin{cases} \dot{z}_{21} &= z_{22} + B_0(x)_{21}u_1 + B_0(x)_{22}u_2 \\ \dot{z}_{22} &= \dot{\Psi}_2(x) \end{cases} \end{aligned} \tag{5.4.11}$$

A third-order SPO, based on equation (5.3.13), is designed for the sub-system q_1.

$$\begin{cases} \dot{\hat{z}}_{11} &= \hat{z}_{12} + h_{11}(z_{11} - \hat{z}_{11}) \\ \dot{\hat{z}}_{12} &= \hat{z}_{13} + h_{12}(z_{11} - \hat{z}_{11}) + B_0(x)_{11}u_1 + B_0(x)_{12}u_2 \\ \dot{\hat{z}}_{13} &= h_{13}(z_{11} - \hat{z}_{11}) \end{cases} \tag{5.4.12}$$

where $[h_{11} \;\; h_{12} \;\; h_{13}] = [\frac{\alpha_{11}}{\epsilon_1} \;\; \frac{\alpha_{12}}{\epsilon_1^2} \;\; \frac{\alpha_{13}}{\epsilon_1^3}]$ are gains of the observer.

A second-order PO designed based on equation (5.3.10) is to estimate the sub-system q_2 perturbation as follows:

$$\begin{cases} \dot{\hat{z}}_{21} &= \hat{z}_{22} + h_{21}(z_{21} - \hat{z}_{21}) + B_0(x)_{21}u_1 + B_0(x)_{22}u_2 \\ \dot{\hat{z}}_{22} &= h_{22}(z_{21} - \hat{z}_{21}) \end{cases} \tag{5.4.13}$$

where $[h_{21} \;\; h_{22}] = [\frac{\alpha_{21}}{\epsilon_2} \;\; \frac{\alpha_{22}}{\epsilon_2^2}]$ are gains of the observer.

After the perturbations are estimated, the nonlinear adaptive control law of the sub-systems q_1 and q_2 are

$$\begin{bmatrix} u_{dr} \\ u_{qr} \end{bmatrix} = B_0(x)^{-1}(\begin{bmatrix} -\hat{\psi}_1 \\ -\hat{\psi}_2 \end{bmatrix} + v) \tag{5.4.14}$$

where v is defined as same as FLC control by equation (5.4.8). Note that an output feedback control of v_1 can be given as:

$$v_1 = -k_{11}e_1 - k_{21}\dot{\hat{e}}_1 \tag{5.4.15}$$

To illustrate the control law clearly, the block diagram of nonlinear adaptive control is shown in Figure 5.2.

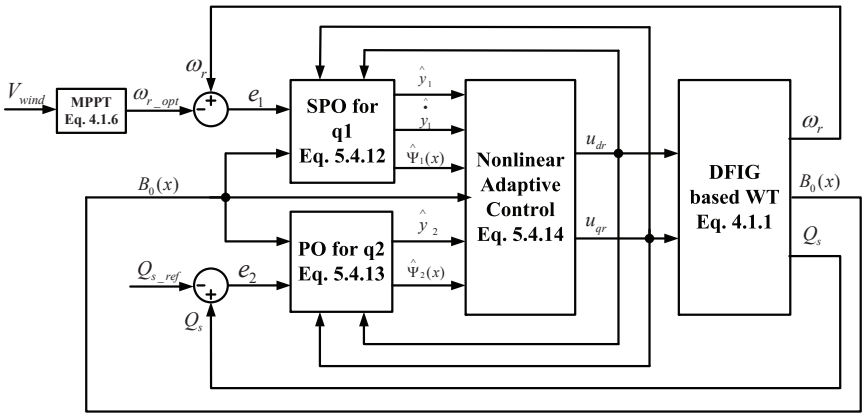

Figure 5.2: Control scheme of NAC with wind speed measurement

5.4.2 Without wind speed measurement

Input-output feedback linearization

Choosing the stator active power P_s and stator reactive power Q_s as controlled outputs:

$$\begin{cases} y_3 = P_s \\ y_4 = Q_s \end{cases} \tag{5.4.16}$$

and defining the tracking error $e = [e_3 \;\; e_4]^T$ as:

$$\begin{cases} e_3 = P_s - P_{s\_ref} \\ e_4 = Q_s - Q_{s\_ref} \end{cases} \tag{5.4.17}$$

where P_{s_ref} is the optimal power output defined in equation (5.2.1), and $Q_{s\_ref} = 0$.

The input/output feedback linearization of equation (4.1.1) can be derived as:

$$\begin{bmatrix} \dot{e}_3 \\ \dot{e}_4 \end{bmatrix} = \begin{bmatrix} f_3 \\ f_4 \end{bmatrix} + C(x) \begin{bmatrix} u_{dr}^* \\ u_{qr}^* \end{bmatrix} \tag{5.4.18}$$

where

$$\begin{aligned} f_3 = {} & \tfrac{L_m u_{ds}}{L_\sigma}(-R_r i_{dr} + (\omega_s - \omega_r)\psi_{qr}) + \tfrac{L_m u_{qs}}{L_\sigma}(-R_r i_{qr} \\ & -(\omega_s - \omega_r)\psi_{dr}) - \tfrac{L_r u_{ds}}{L_\sigma}(u_{ds} - R_s i_{ds} + \omega_s \psi_{qs}) \\ & -\tfrac{L_r u_{qs}}{L_\sigma}(u_{qs} - R_s i_{qs} - \omega_s \psi_{ds}) \end{aligned} \tag{5.4.19}$$

$$\begin{aligned} f_4 = {} & u_{qs}\tfrac{L_m}{L_\sigma}(-R_r i_{dr} + (\omega_s - \omega_r)\psi_{qr}) - u_{qs}\tfrac{L_r}{L_\sigma}(u_{ds} - \\ & R_s i_{ds} + \omega_{qs}) - u_{ds}\tfrac{L_m}{L_\sigma}(-R_r i_{qr} - (\omega_s - \omega_r)\psi_{dr}) + \\ & u_{ds}\tfrac{L_r}{L_\sigma}(u_{qs} - R_s i_{qs} - \omega_s \psi_{ds}) \end{aligned} \tag{5.4.20}$$

and

$$C(x) = \begin{pmatrix} \frac{L_m}{L_\sigma} u_{ds} & \frac{L_m}{L_\sigma} u_{qs} \\ \frac{L_m}{L_\sigma} u_{qs} & -\frac{L_m}{L_\sigma} u_{ds} \end{pmatrix} \tag{5.4.21}$$

where $C_0(x) = C(x)|_{L_m = L_{m0}}$, $\Delta C(x) = C(x) - C_0(x)$.

Note that $\Delta C(x)$ represents parameter uncertainties of control gains, and when $det(C) = \frac{L_m^2}{L_\sigma^2}(-u_{ds}^2 - u_{qs}^2) \neq 0$, system (5.4.3) can be linearized as

$$\begin{bmatrix} \dot{e}_3 \\ \dot{e}_4 \end{bmatrix} = \begin{bmatrix} v_3 \\ v_4 \end{bmatrix} \tag{5.4.22}$$

and $v^* = [v_1^* \;\; v_2^*]^T$ is the control input of the linear system:

$$\begin{bmatrix} v_1^* \\ v_2^* \end{bmatrix} = \begin{bmatrix} -k_3 e_3 \\ -k_4 e_4 \end{bmatrix} \tag{5.4.23}$$

where k_3, k_4 are the feedback gains.

The FLC control law of equation (4.1.1) can be obtained as

$$\begin{bmatrix} u_{dr}^* \\ u_{qr}^* \end{bmatrix} = C(x)^{-1} \begin{bmatrix} -f_3 + v_1^* \\ -f_4 + v_2^* \end{bmatrix} \tag{5.4.24}$$

Perturbation estimation

The perturbations $\Psi_3(x)$ and $\Psi_4(x)$ for two subsystems q_3 and q_4 are expressed respectively as:

$$\begin{cases} \Psi_3(x) &= f_3(x) - \dot{P}_{s\_ref} + \Delta C(x)_{11}u_1^* + \Delta C(x)_{12}u_2^* \\ \Psi_4(x) &= f_4(x) - \dot{Q}_{s\_ref} + \Delta C(x)_{11}u_1^* + \Delta C(x)_{12}u_2^* \end{cases} \tag{5.4.25}$$

where $u_1^* = u_{dr}^*$, $u_2^* = u_{qr}^*$.

Defining the state vectors $z_{11}^* = y_3, z_{12}^* = \Psi_3(x)$, $z_{21}^* = y_4, z_{22}^* = \Psi_4(x)$. The dynamic equations of the system can be described as

$$\begin{aligned} q_3: & \begin{cases} \dot{z}_{11}^* &= z_{12}^* + C_0(x)_{11}u_1^* + C_0(x)_{12}u_2^* \\ \dot{z}_{12}^* &= \dot{\Psi}_3(x) \end{cases} \\ q_4: & \begin{cases} \dot{z}_{21}^* &= z_{22}^* + C_0(x)_{21}u_1^* + C_0(x)_{22}u_2^* \\ \dot{z}_{22}^* &= \dot{\Psi}_4(x) \end{cases} \end{aligned} \tag{5.4.26}$$

Based on equation (5.3.10), two second-order PO is designed to estimate the sub-system q_1' and q_2' perturbation as follows:

$$\begin{cases} \dot{\hat{z}}_{11}^* &= \hat{z}_{12}^* + h_{11}^*(z_{11}^* - \hat{z}_{11}^*) + C_0(x)_{11}u_1^* + C_0(x)_{12}u_2^* \\ \dot{\hat{z}}_{12}^* &= h_{12}^*(z_{11}^* - \hat{z}_{11}^*) \end{cases} \tag{5.4.27}$$

and

$$\begin{cases} \dot{\hat{z}}_{21}^* &= \hat{z}_{22}^* + h_{21}^*(z_{21}^* - \hat{z}_{21}^*) + C_0(x)_{21}u_1^* + C_0(x)_{22}u_2^* \\ \dot{\hat{z}}_{22}^* &= h_{22}^*(z_{21}^* - \hat{z}_{21}^*) \end{cases} \tag{5.4.28}$$

where $[h_{11}^* \;\; h_{12}^*] = [\frac{\alpha_{11}^*}{\epsilon_1^*} \;\; \frac{\alpha_{12}^*}{\epsilon_1^{*2}}]$ and $[h_{21}^* \;\; h_{22}^*] = [\frac{\alpha_{21}^*}{\epsilon_2^*} \;\; \frac{\alpha_{22}^*}{\epsilon_2^{*2}}]$ are gains of the observer.

After the perturbation estimation, the nonlinear adaptive controller of sub-systems q_3 and q_4 can be derived as

$$\begin{bmatrix} u_{dr}^* \\ u_{qr}^* \end{bmatrix} = C_0(x)^{-1}(\begin{bmatrix} -\hat{\psi}_3 \\ -\hat{\psi}_4 \end{bmatrix} + v^*) \tag{5.4.29}$$

here v^* is defined as

$$\begin{bmatrix} v_1^* \\ v_2^* \end{bmatrix} = \begin{bmatrix} -k_3\hat{e}_3 \\ -k_4\hat{e}_4 \end{bmatrix} \tag{5.4.30}$$

Figure 5.3 shows the block diagram of nonlinear adaptive control without wind speed measurement.

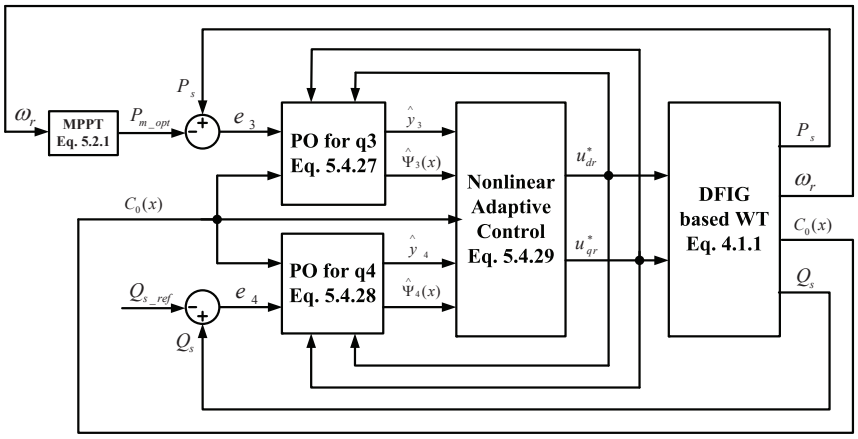

Figure 5.3: Control scheme of NAC without wind speed measurement

5.5 Simulation Studies

In this section, the simulation studies are carried out to verify the effectiveness of the proposed NAC by the following case studies: MPPT control with wind speed measurement and without wind speed measurement, parameter uncertainties during constant wind speed. The parameters of the DFIG-WT tested are the same as listed in chapter 4.

5.5.1 With wind speed measurement

Step change of wind speed

For verifying the performance of the proposed NAC method against the large step change of the wind speed, shown in Figure 5.4, the simulation studies on MPPT of DFIG-WT are carried out by applying FLC and NAC.

From the Figure 5.5, it can be clearly seen that, both the FLC and NAC can achieve the maximum power coefficient during the constant wind speed. However, while the wind speed changes, an increasing error of C_p provided by the FLC can be observed clearly when the large step change of wind speed occurs at $50s$. The simulation result shows that the proposed NAC can provide better performance on power coefficient.

Figure 5.6(a) gives the dynamic responses of rotor speed controlled by FLC and NAC. In order to display the difference between FLC and NAC clearly, the values of ITAE of ω_r for FLC and NAC are shown in Figure 5.6(b). From the obtained results, it can be easily found the rotor speed ω_r controlled by NAC is more close to the optimal reference value than that by the FLC.

To verify the performance for MPPT, the electric power outputs by applying FLC and NAC are carried out in Figure 5.7, with the ITAE compared with the optimal mechanical power. The results show that the overshoot for the NAC is smaller than that for the FLC, and can provide optimal power output more quickly.

The dynamic responses of the stator reactive power for the FLC and NAC are given in Figure 5.8, the stator reactive power controlled by the NAC can compensate the power losses during the step change of wind speed, thereby, improve the efficiency of power conversion and stability of grid.

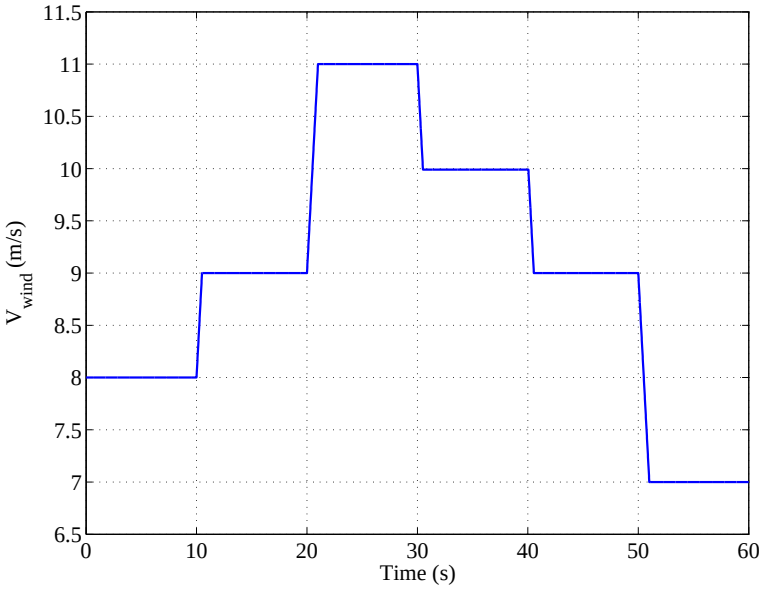

Figure 5.4: Step change of wind speed

The estimation of perturbation f_1 is also given in Figure 5.11. The results show that the estimated perturbation $\hat{f}_1$ can track the f_1 well under NAC. The same performance of f_2 estimation is shows in Figure 5.13. Moreover, the estimations of rotor speed and stator reactive power are illustrated in Figures 5.10 and 5.12.

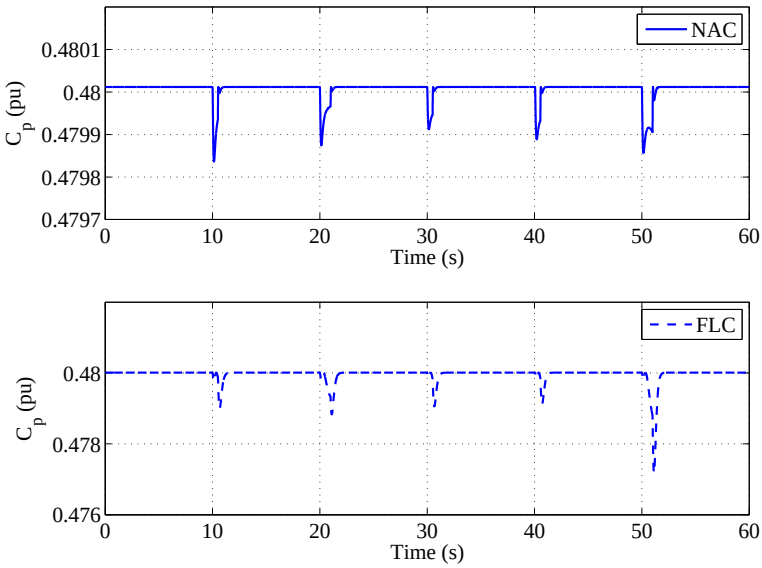

Figure 5.5: Power coefficient under step change of wind speed

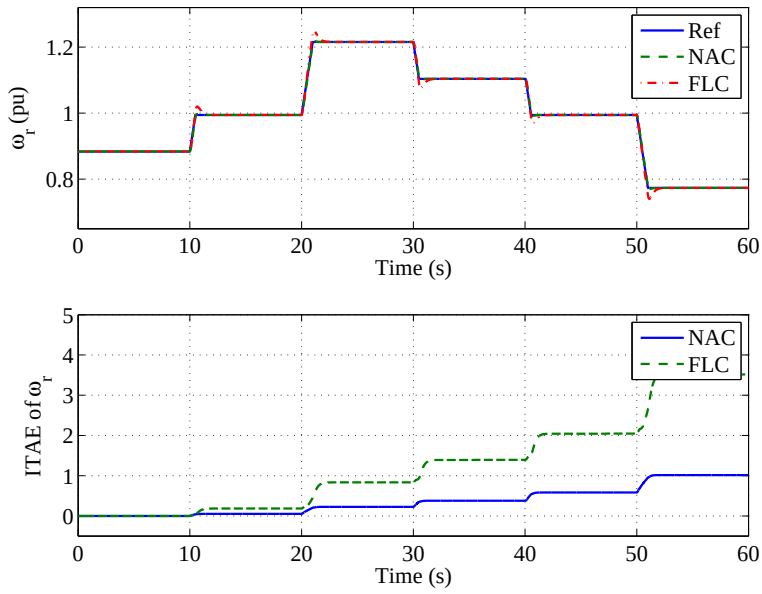

Figure 5.6: Response of rotor speed under step change of wind speed

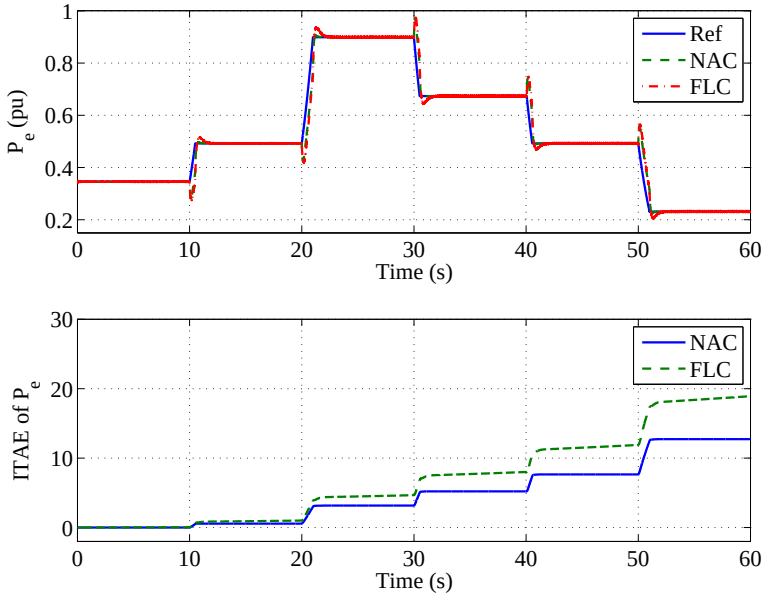

Figure 5.7: Response of electric power under step change of wind speed

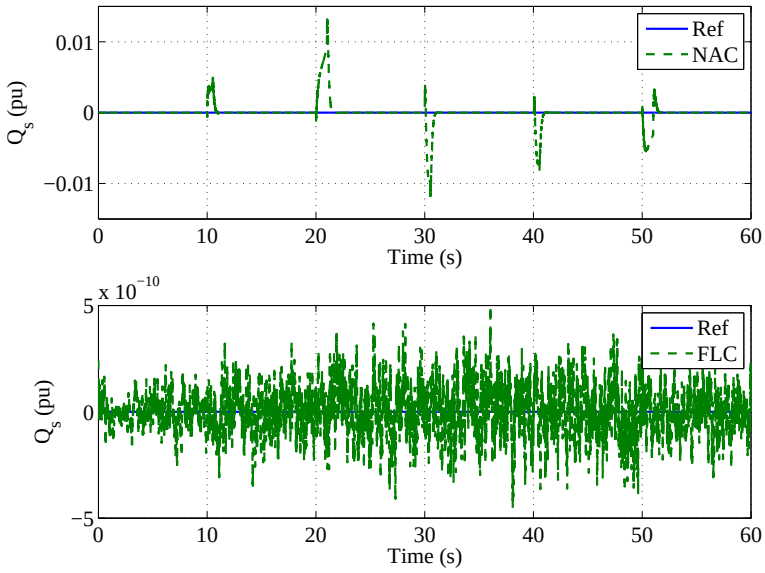

Figure 5.8: Response of stator reactive power under step change of wind speed

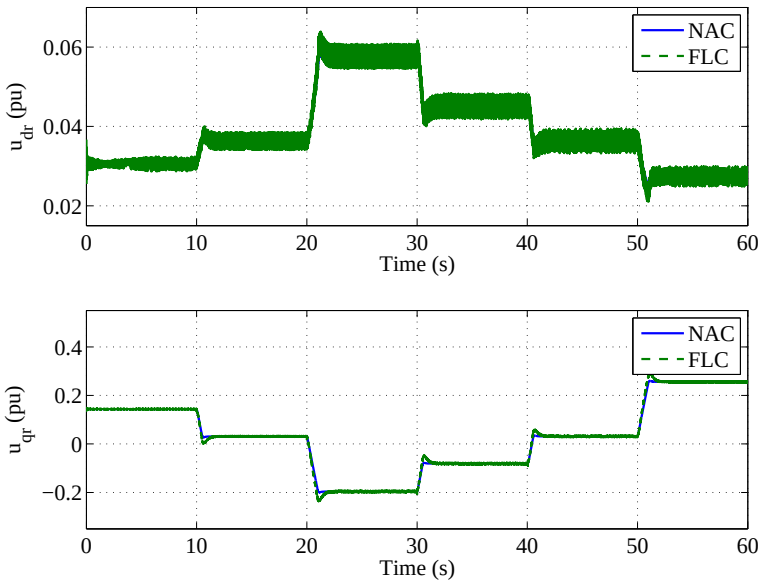

Figure 5.9: Rotor voltage of NAC and FLC in d-axis

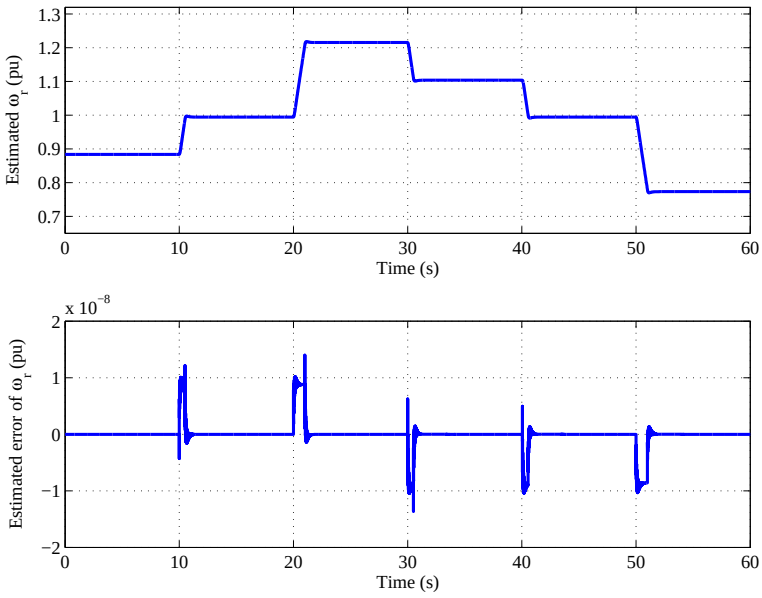

Figure 5.10: Rotor speed ω_r estimation and estimate error

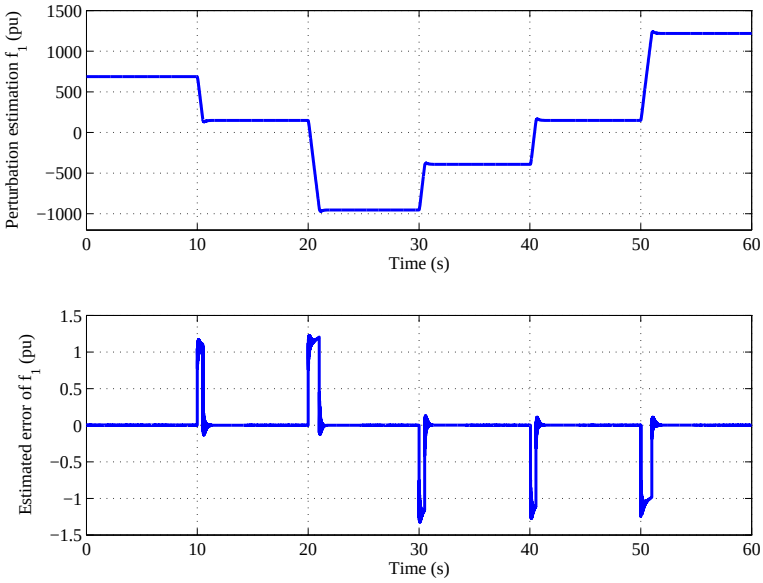

Figure 5.11: Perturbation response of f_1 under step change of wind speed

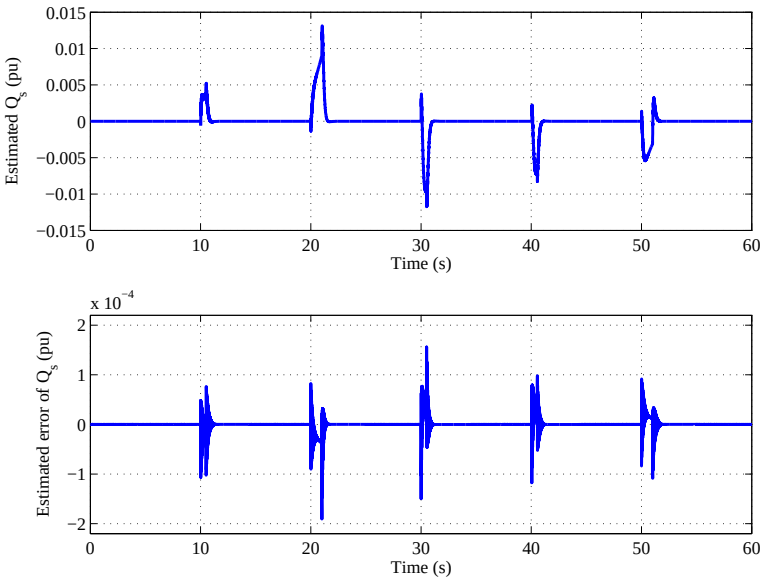

Figure 5.12: Stator reactive power Q_s estimation and estimate error

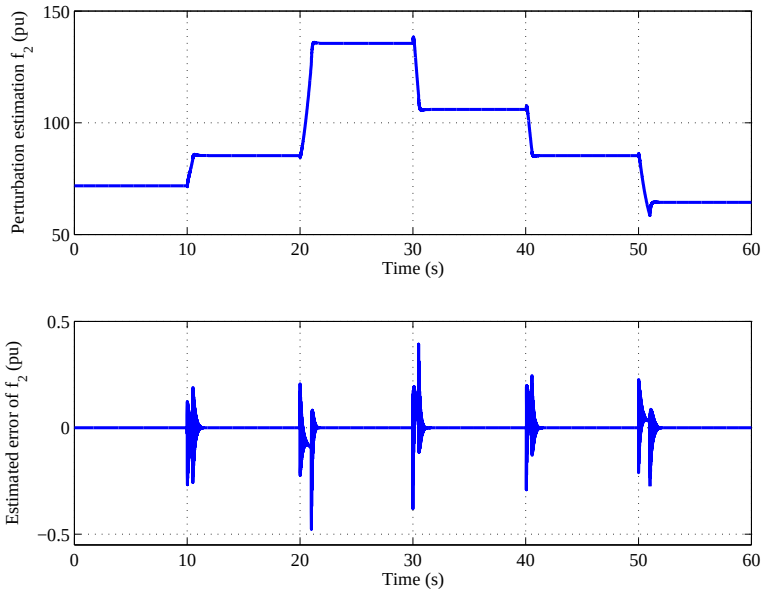

Figure 5.13: Perturbation response of f_2 under step change of wind speed

Random wind speed

In order to verify the performance of the proposed NAC method against the random wind speed around a basic value, which is more common in real world, the close-loop system is tested under the wind speed with bounded random changes, as shown in Figure 5.14. Without loss of generality, it is assumed that the wind speed changes randomly around 8 m/s within 600 seconds.

The power coefficient, C_p, obtained by the FLC and NAC are shown in Figure 5.15. From the figure, both the FLC and NAC can provide the power coefficient near to its maximal value, 0.48, for different wind speed. The value of C_p provided by the NAC (within [0.4799,0.48]) is closer to this maximal value than the one provided by the FLC (within [0.479,0.48]).

The responses of the rotor speed with its ITAE, the electric power with its ITAE, the stator reactive power, and rotor voltage (control input) are shown in Figs. 5.16-5.19. From these results, it can be found that the NAC can provide better performance than the FLC does for the whole operation interval, such as the smaller tracking errors of the rotor speed (Figure 5.16), the electric power (Figure 5.17), and the stator reactive power (Figure 5.18).

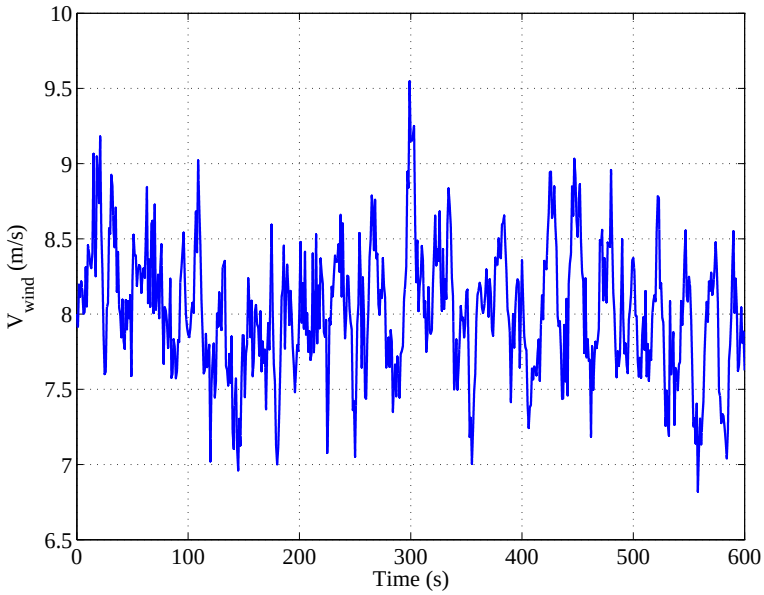

Figure 5.14: Time-varying wind speed

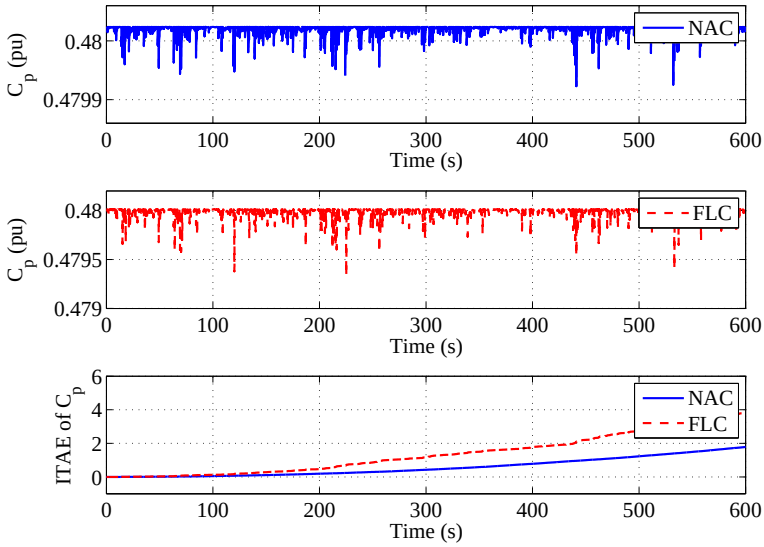

Figure 5.15: Power coefficient under time-varying wind speed

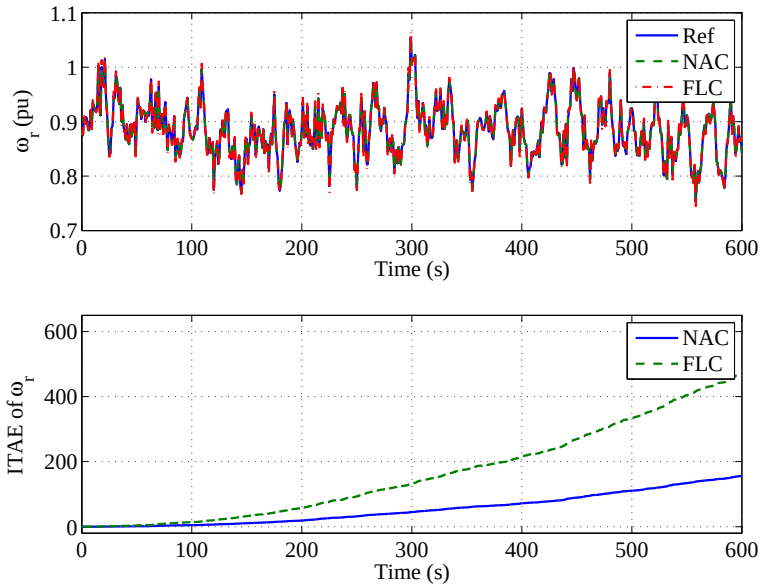

Figure 5.16: Response of rotor speed under time-varying wind speed

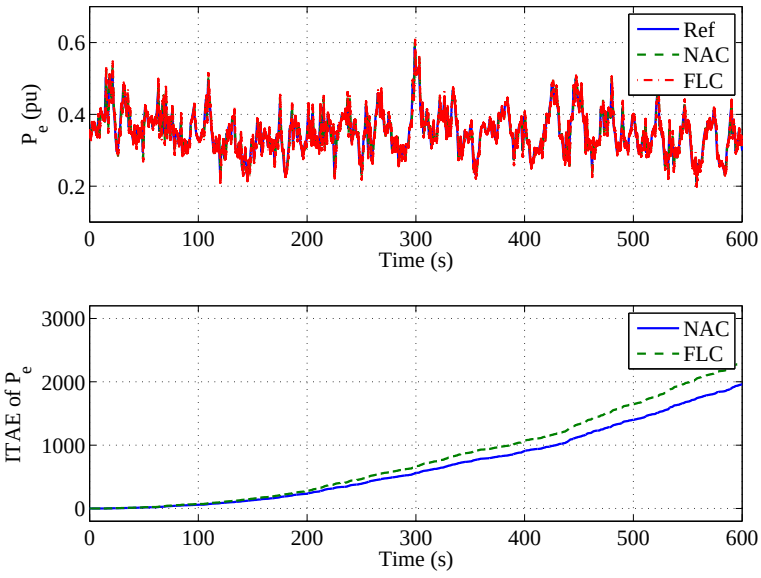

Figure 5.17: Response of electric power under time-varying wind speed

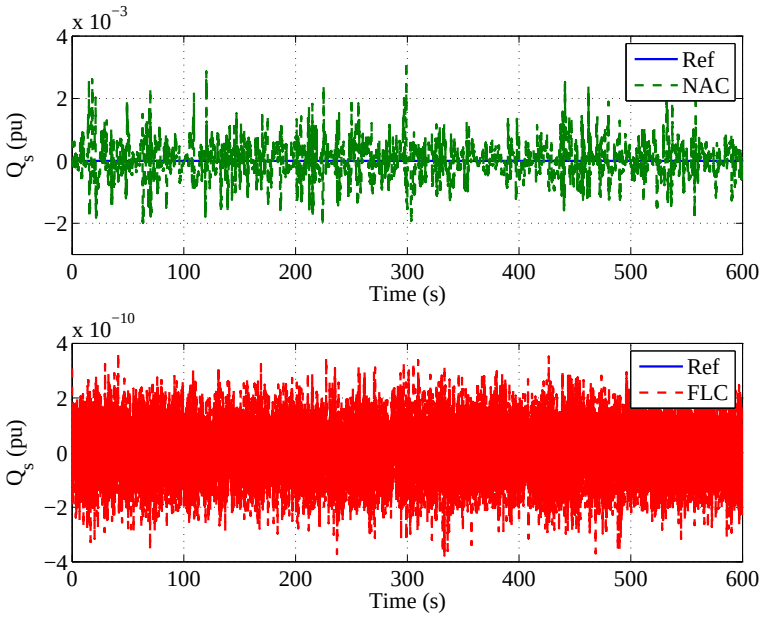

Figure 5.18: Response of stator reactive power under time-varying wind speed

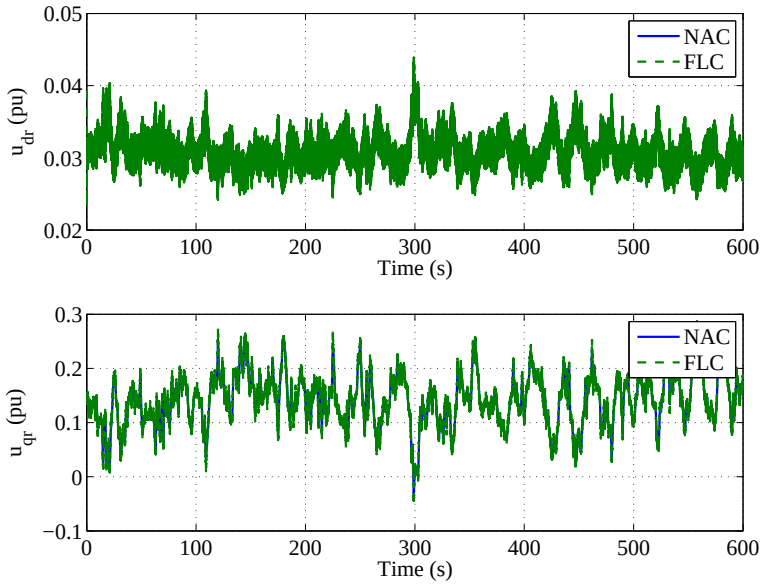

Figure 5.19: Rotor voltage of NAC and FLC in d-axis

The estimation of perturbations are also given shown in Figure 5.21 and 5.23. It shows the estimated perturbation $\hat{f}_1$ can track the f_1 with negligible errors under NAC. Moreover, the estimations of rotor speed and stator reactive power are illustrated in Figures 5.20 and 5.22.

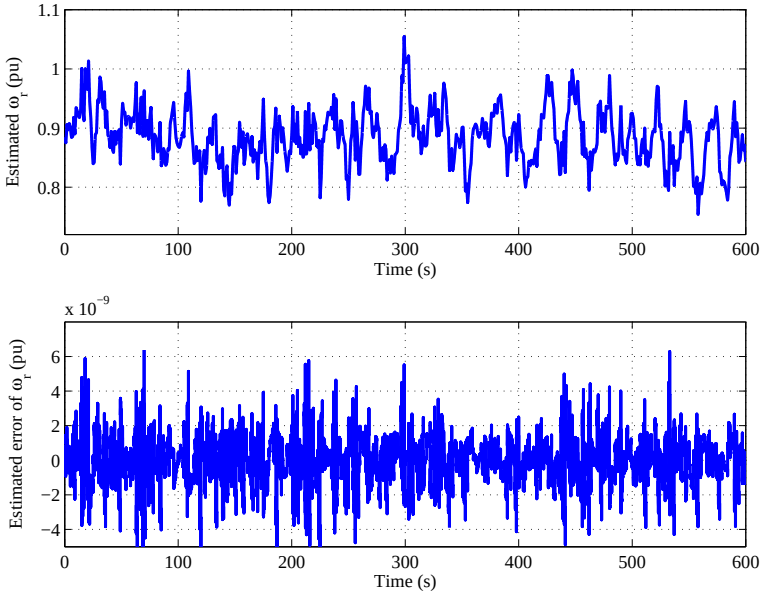

Figure 5.20: Rotor speed ω_r estimation and estimate error

5.5.2 Without wind speed measurement

In this section, the simulation studies without wind speed measurement are carried out by FLC and NAC. To achieve the optimal power output defined in equation (5.2.1), the electric power and stator reactive power are controlled, with the results shown in Figure 5.26 and 5.27. In this case, the signal of wind speed is set as Figure 5.24. The obtained results show that both NAC and FLC can achieve the optimal power output with a small delay. Moreover, the indirectly controlled rotor speed for both FLC and NAC can achieve the optimal value calculated from the wind speed. The control inputs are also given in Figure 5.28.

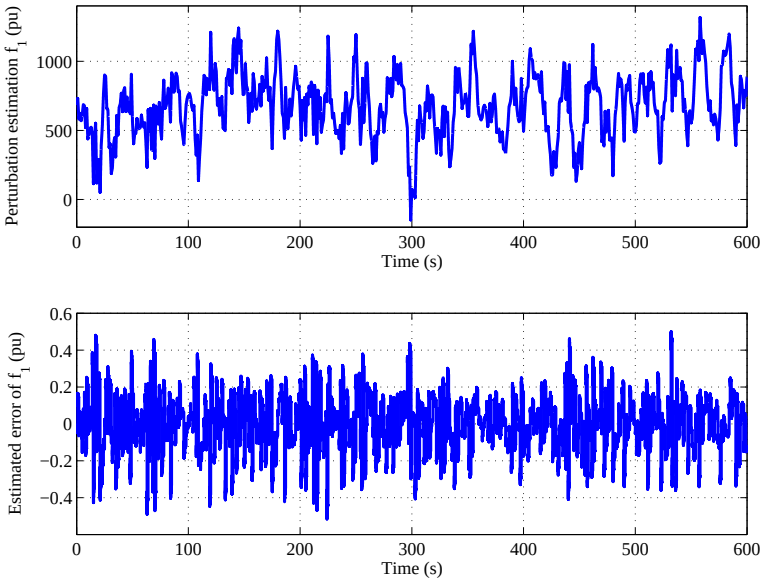

Figure 5.21: Perturbation response of f_1 under time-varying wind speed

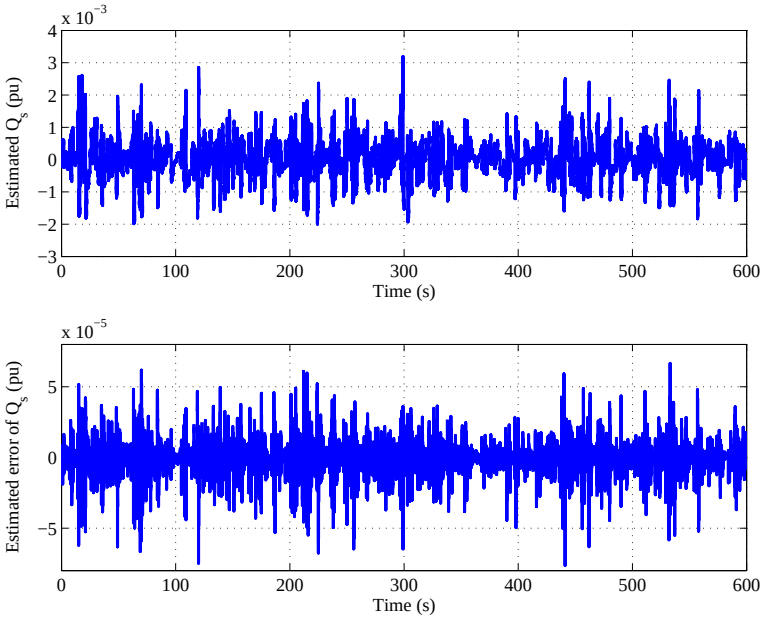

Figure 5.22: Stator reactive power Q_s estimation and estimate error

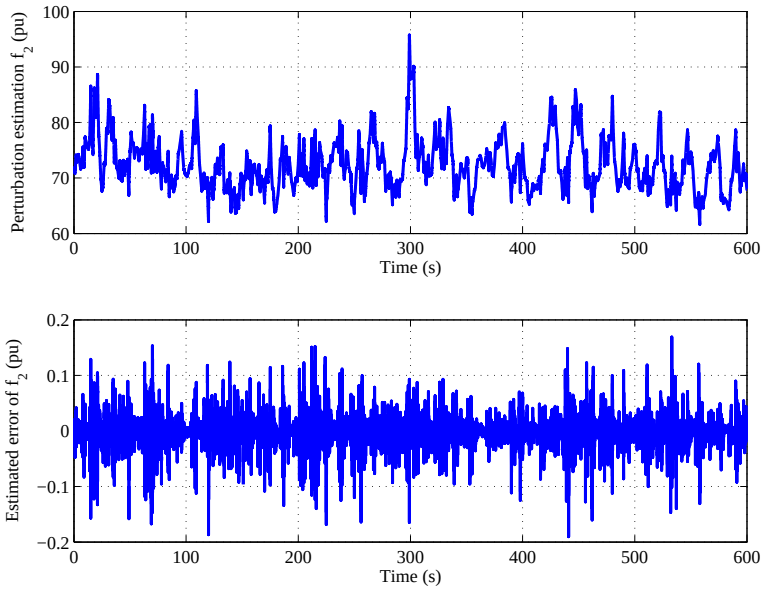

Figure 5.23: Perturbation response of f_2 under time-varying wind speed

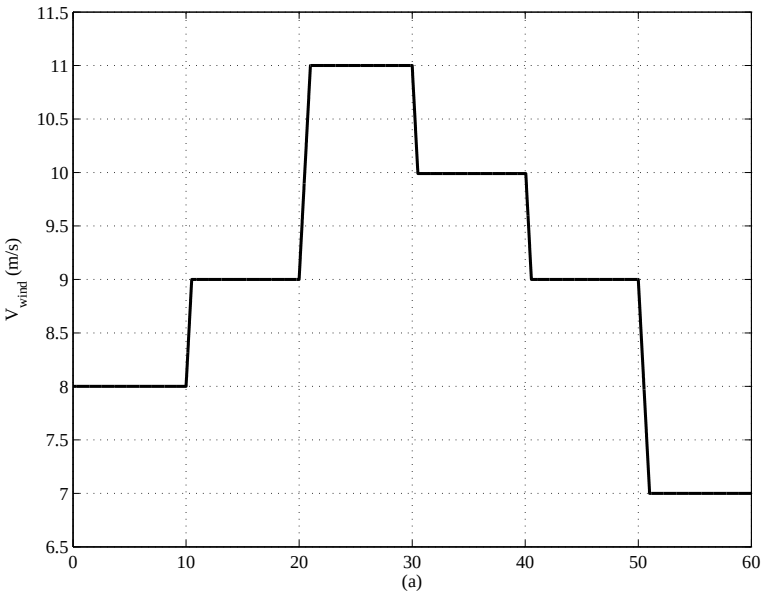

Figure 5.24: Case of without wind speed measurement

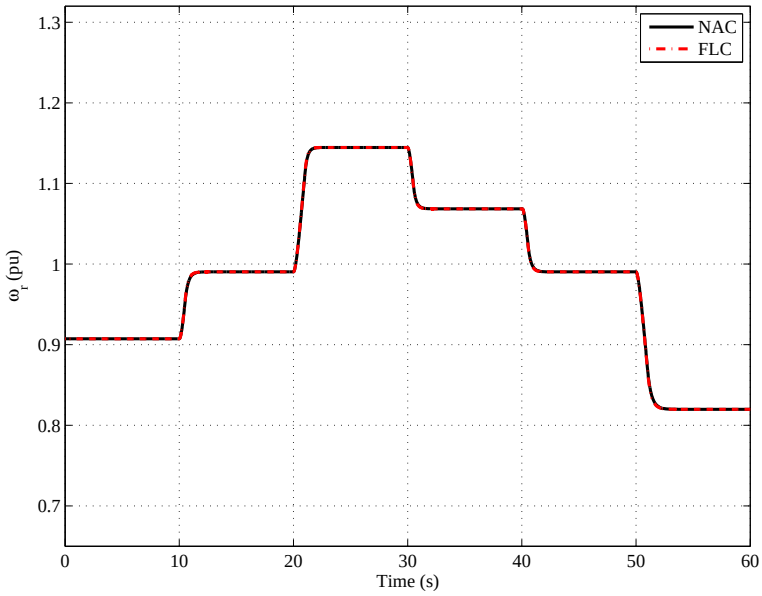

Figure 5.25: Response of rotor speed without wind speed measurement

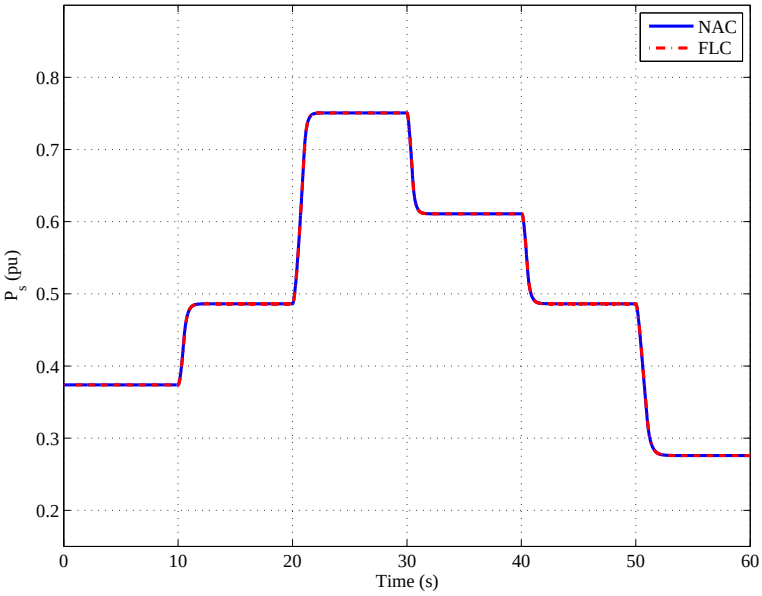

Figure 5.26: Response of electric power without wind speed measurement

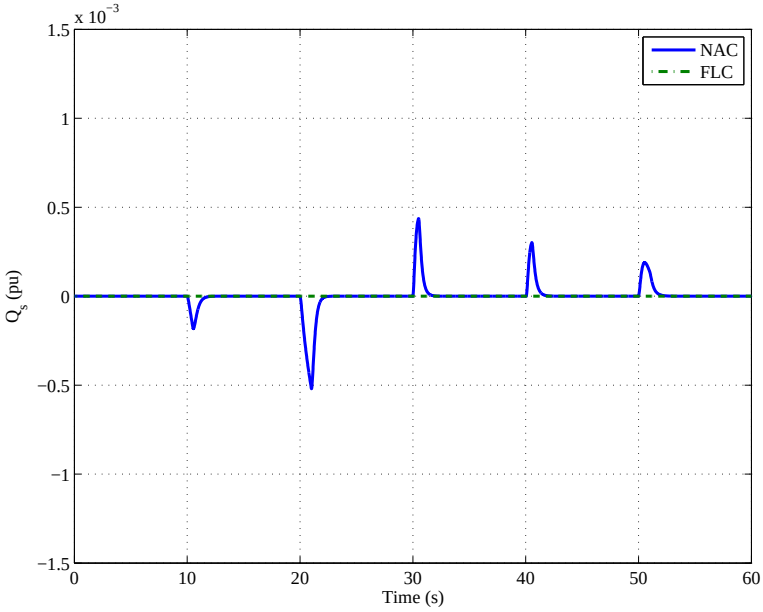

Figure 5.27: Response of stator reactive power without wind speed measurement

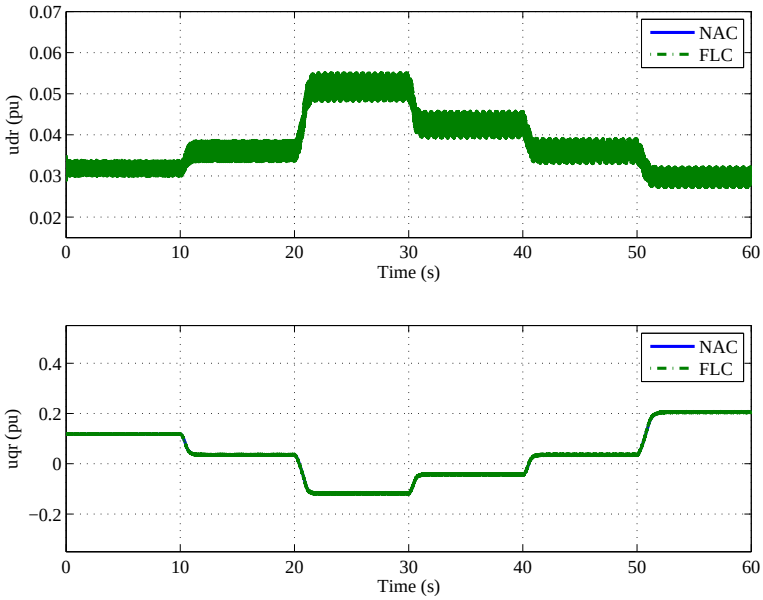

Figure 5.28: Rotor voltage of NAC and FLC in d-axis without wind speed measurement

5.5.3 Parameter uncertainties

Uncertainties of rotor resistance

In order to test the robustness of controllers against the parameter uncertainty, the FLC and NAC are tested when their assumed parameter values differ from the actual plant parameters. In this test, the stator resistance R_r is modified by $20-50\%$ during the simulations. The parameter variations on rotor resistance is shown in $5.29(a)$. In Figure $5.29(b)$, the errors between the electric power and the maximum power output of FLC, NAC under normal parameters and uncertainty parameters are described. As the performance of FLC mainly depends on the accurate model and parameters of system, the electrical power tracking by applying FLC performs not good enough.

In Figure 5.30, the errors of system outputs in the case of rotor resistance uncertainty are compared with those in normal parameters by applying two control approaches. From the simulation results, it can be easily observed that the proposed controller achieve better robustness.

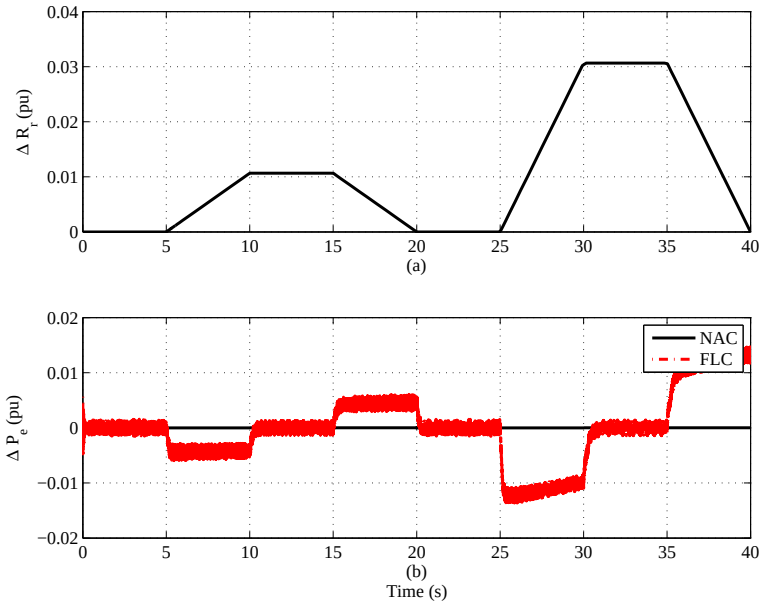

Figure 5.29: Electric power errors under uncertainties of rotor resistance

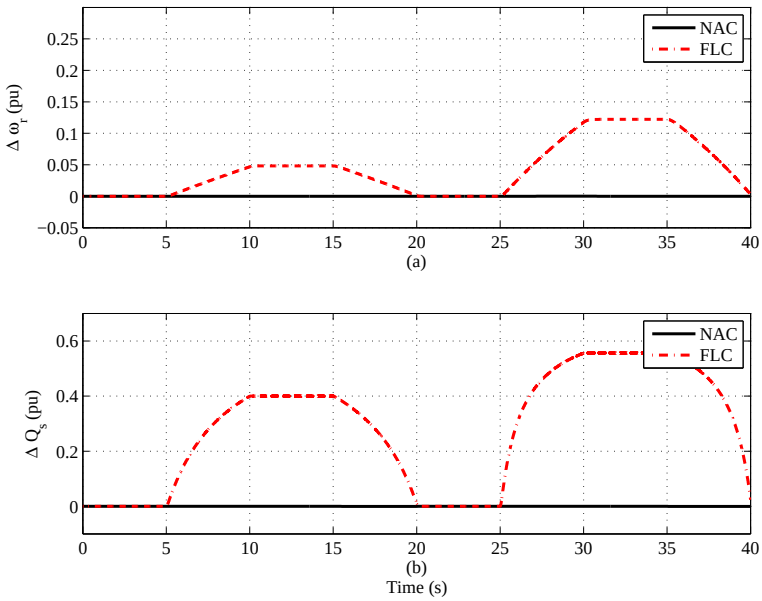

Figure 5.30: System outputs errors under uncertainties of rotor resistance

Tower shadow

In the wind energy conversion systems, tower shadow and wind shear contribute to periodic fluctuations in electrical power output of a wind turbine generator. In this case, the signal shown in Figure 5.31 (a) simulates the fluctuation caused by tower shadow. The differences of the electrical power output errors by applying FLC and NAC are represented in Figure 5.31 (b).

The system outputs errors during tower shadow fluctuation can be also observed from Figure 5.32. As shown in the obtained results, the proposed nonlinear adaptive controller given no steady-state error and the same behavior as in the normal parameter.

Grid voltage dip

During the period of conventional power generation, the short-term voltage dips also affect the electrical power output of DFIG-WT. A $200ms$ voltage drop is simulated in Figure 5.33 (a). From Figure 5.33 (b), the better performance of electrical power output can be obtained by applying NAC than that of FLC . In Figure 5.34, the errors of system outputs controlled by FLC, and NAC are compared with each

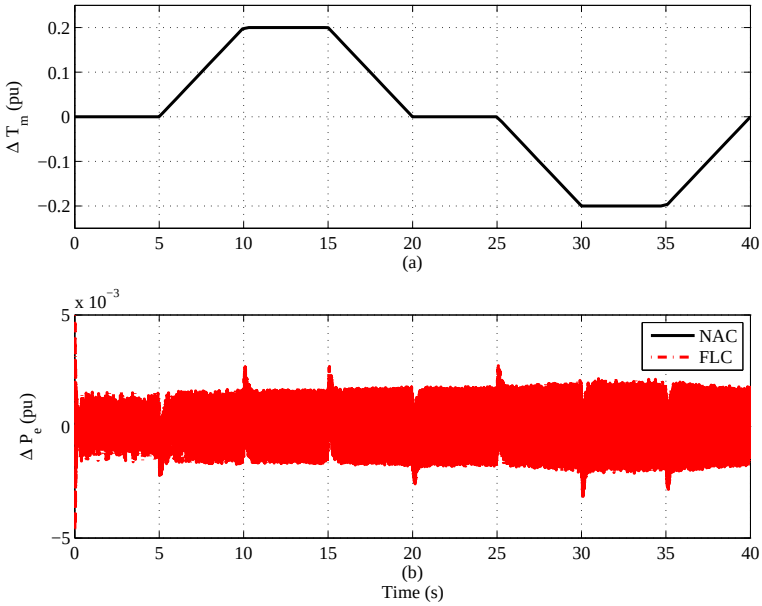

Figure 5.31: Electric power errors under tower shadow

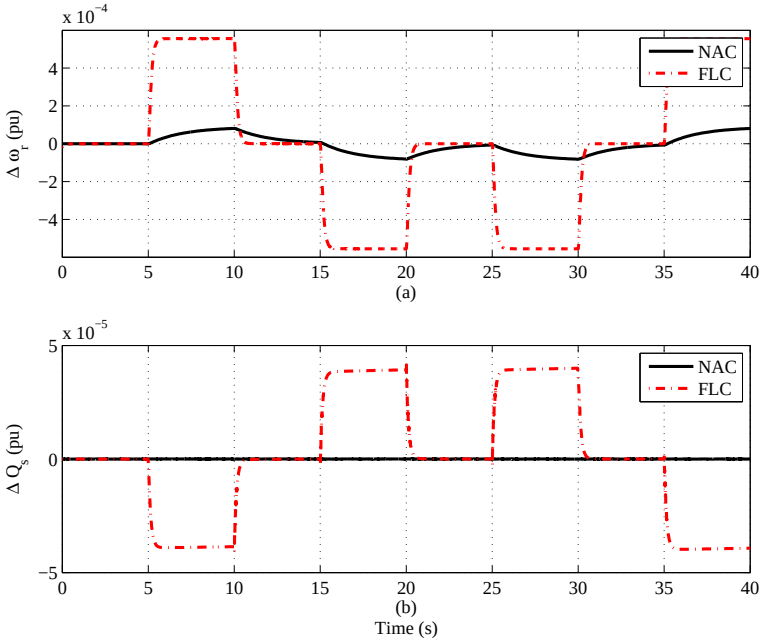

Figure 5.32: System outputs errors under tower shadow

other. The obtained results show that the proposed nonlinear adaptive controller can achieve the same performance during the parameter uncertainties as in normal parameters.

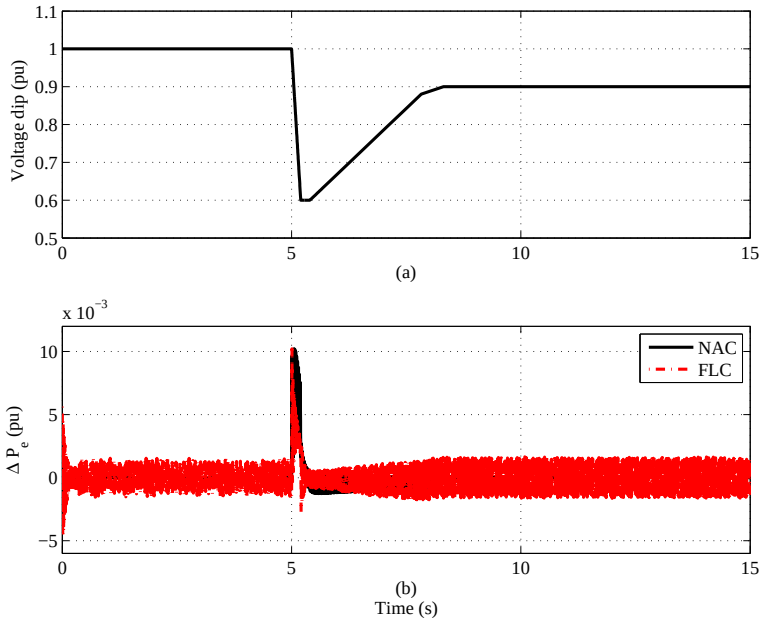

Figure 5.33: Electric power errors under grid voltage dips

5.6 Summary

This chapter investigated the nonlinear adaptive control for DFIG-WT in order to deal with the parameter uncertainties, uncertain wind power inputs and improve the robustness of the nonlinear controller proposed in Chapter 4. The proposed adaptive controller designed a perturbation observer to estimate the real time perturbation and used it to compensate the real uncertainties and disturbances. The design consisted of two cases: with and without wind speed measurement, are carried out, followed by simulation studies. The simulation results shown that the proposed nonlinear adaptive control can achieve better robustness than the FLC under conditions of parameter uncertainties and uncertainty wind power inputs.

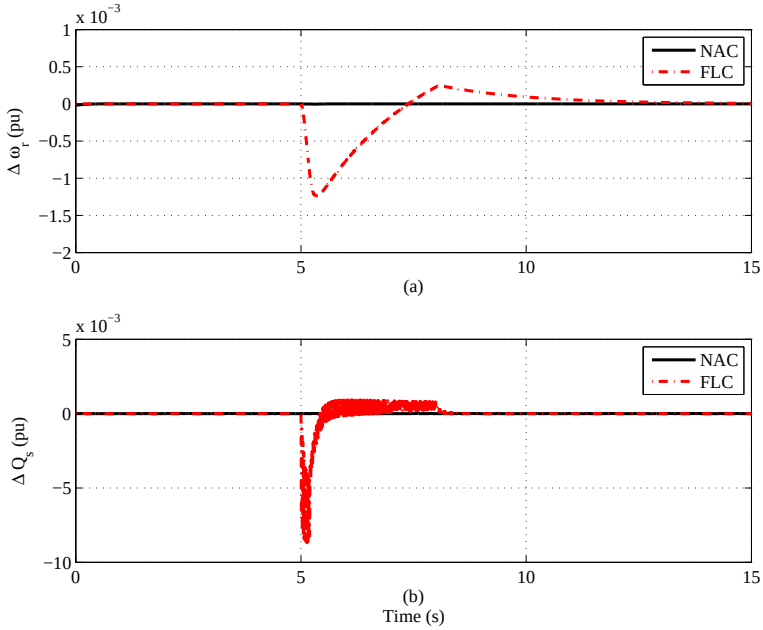

Figure 5.34: System outputs errors under grid voltage dips

Chapter 6

Conclusion and Future Work

6.1 Conclusion

Wind power, as one of the clean and alternative energy sources, is expect to become one one mainstream energy source and probably the largest renewable energy source in Europe in the next decades, researches on maximizing the power conversion coefficient, and improving the power quality are essential. In this thesis, the advanced control strategies of doubly fed induction generator based variable speed wind turbine have been investigated and developed.

This thesis focuses on improving the power conversion efficiency and transient dynamics of DFIG-WT. The DFIG-WT is a dynamic system with strong nonlinear coupled characteristics and time-varying uncertain inputs, and during voltage sags due to grid load disturbances or grid faults, DFIG-WT will operate far away from its normal operation point. For these requirements, the control strategies of DFIG-WT should be designed to operate at an operation envelope with a wide range during time-varying inputs, and maintain a robust transient response under grid disturbance or parameter uncertainties.

For the controller design, the modeling of DFIG-WT including wind turbine, drive train, DFIG and power electrical converters were investigated at first. As the dynamic response of the DFIG-WT's electrical part is faster than that of mechanical part, the model of drive train normally can be simplified as one-mass model for

the studies on the power regulation of DFIG-WT. The detailed dynamic model of DFIG has been obtained in the two-phase (d-q) rotating reference frame by applying Clarke and Park Transformations, for the method based on three-phase natural reference frame. This type transformation (via transforming variables to a special reference frame) resulted in the simple design of linear PI based vector controller, however, the PI based vector controller can only achieve partial linearization of the original nonlinear system. Moreover, the dynamic of the grid-side converter and DC-link capacitor were also investigated.

The conventional power control method, vector control, has been studied in chapter 3 at first. As the conventional control strategy can only achieve the asymptotical regulation of the stator active and reactive power of the DFIG, a fully decoupled nonlinear power control based on feedback linearization control has been designed for the direct power control of the DFIG. Moreover, a cascade nonlinear controller, which consisted of two stages, an outer loop provide rotor current reference from the stator active and reactive powers, and an inner loop applied the input/output feedback linearization control for current regulation. Two cases were studied to verify the performance of the proposed control strategy: (1) The operation points of system outputs were varying at the same time, thereby, the shortage of PI based vector control appeared. In other hand, it shows that the nonlinear control strategies can achieve fully decoupling control and global optimization; (2) Face to the sudden grid voltage drop, the proposed cascaded control strategy provided the best transient response during the disturbance.

The maximum power point tracking (MPPT) control of DFIG-WT focuses on improving the power conversion coefficient and dynamic response during the time-varying and uncertainty wind power inputs. In chapter 4, the nonlinear feedback control based maximum power point tracking (MPPT) has been studied. Both VC and FLC are applied for MPPT control under time-varying wind speeds, to achieve the maximum power extraction form the wind power. Modal analysis was used to analysis the dynamics of DFIG-WT provided by VC and FLC respectively, which show that the FLC can provide consistent dynamics with time-varying wind power inputs.

In order to deal with the parameter uncertainties and uncertain wind power inputs, Chapter 5 investigated the nonlinear adaptive control for MPPT of DFIG-WT. For improving the robustness of the nonlinear controller proposed in Chapter 4, The proposed adaptive controller designed a perturbation observer to estimate the real time perturbation and used it to compensate the real uncertainties and disturbances. The simulation results proved that the proposed NAC for MPPT of DFIG-WT can supply better robustness performance than FLC during the parameter uncertainties and uncertain wind power inputs.

6.2 Future Works

The possible future work is listed based on the following ideas.

I The zero-dynamic of the FLC-based power control and the FLC-based MPPT controller has not been investigated, though the stability of controllers have been studied via modal analysis (the FLC-MPPT) or simulation studies (the FLC-power & the FLC-MPPT). Future work will investigate the zero-dynamic of the FLC based controllers remained internal dynamic.

II NAC can be also applied on pitch control of WT to reduce the mechanical stress on the drive train and improve the energy conversion efficiency of the WT operating above the rated wind speed. The design will be based on the two-mass model of the WT, while simulation studies will focus on the detailed model provided by the FAST (Fatigue, aerodynamics, structures, and turbulence) software package. The designed NAC will work together with the NAC power control for DFIG.

III NAC for grid-side converter of DFIG-WT. This work is to design a NAC-based converter controller and applied for the grid-side converter of DFIG-WT to stabilize the DC-link voltage and maintain the unity power factor, and then for the grid-side converter of the WPGS with the full-rated converter to improve the FRT capability and robustness of the converter controller, respectively. The coordination and decoupling of the proposed NACs for DFIG-WT

will be verified by simulation studies.

References

[1] R. Swisher, C. R. De Azua, J. Clendenin, “Strong winds on the horizon: wind power comes of age,” *IEEE Proceedings*, vol. 89, no. 12, pp. 1757-1764, Dec. 2001.

[2] S. Heier, *Grid integration of wind energy conversion systems*. John Wiley and Sons, New York, 1998.

[3] M. Ahlstrom, L. Jones, R. Zavadil, and W. Grant, “The Future of Wind Forecasting and Utility Operation,” *IEEE Power and Energy Magazine*, vol. 3, no. 6, pp. 57-64, Nov./Dec. 2005.

[4] R. Piwko, D. Osborn, R. Gramlich, G. Jordan, D. Hawkins, and K. Porter, “Wind Energy Delivery Issues,” *IEEE Power and Energy Magazine*, vol. 3, no. 6, pp. 47-56, Nov./Dec. 2005

[5] J. Ekanauake, L. Holdsworth, and N. Jenkins, “Control of DFIG Wind Turbines,” *IEEE Power Engineer*, vol. 17, pp. 28-32, Feb. 2003.

[6] R. Pena, J.C. Clare and G.M. Asher, “Doubly fed induction generator using back-to-back PWM converters and its application to variable speed wind-energy generation,” *IEE Proceedings Electrical Power Applications*, vol. 143, no. 3, pp. 231-241, May 1996.

[7] S. Peresada, A. Tilli and A. Tonielli, “Power control of a doubly fed induction machine via output feedback,” *Control Engineering Practice*, vol. 12, no. 1, pp. 41-57, Jan. 2004.

[8] S. Muller, M. Deicke and R. W. De Doncker, "Doubly fed induction generator systems for wind turbines," *IEEE Industry Applications Magazine*, vol. 8, no. 3, pp. 26-33, May-Jun. 2002.

[9] A. Petersson, L. Harnefors and T. Thiringer, "Evaluation of current control methods for wind turbines using doubly-fed induction machines," *IEEE Transactions on Power Electronics*, vol. 20, no. 1, pp. 227-235, Jan. 2005.

[10] R. Datta and V. T. Ranganathan, "Direct power control of grid-connected wound rotor induction machine without rotor position sensors," *IEEE Transactions on Power Electronics*, vol. 16, no. 3, pp. 390-399, May 2001.

[11] L. Xu and P. Cartwright, "Direct active and reactive power control of DFIG for wind energy generation," *IEEE Transactions on Energy Conversion*, vol. 21, no. 3, pp. 750-758, Sep. 2006

[12] D. W. Zhi and L. Xu, "Direct power control of DFIG with constant switching frequency and improved transient performance," *IEEE Transactions on Energy Conversion*, vol. 22, no. 1, pp. 110-118, Mar. 2007.

[13] J. Hu, H. Nian, B. Hu, Y. He and Z. Q. Zhu, "Direct active and reactive power regulation of DFIG using sliding mode control approach," *IEEE Transactions on Energy Conversion*, vol. 25, no. 4, pp. 1028-1039, Dec. 2010.

[14] L. Shang and J. B. Hu, "Sliding-mode-based direct power control of grid-connected wind-turbine-driven doubly fed induction generators under unbalanced grid voltage conditions," *IEEE Transactions on Energy Conversion*, vol. 27, no. 2, pp. 362-373, Jun. 2012.

[15] A. Mullane, G. Lightbody and R. Yacamini, "Wind turbine fault ride-through enhancement," *IEEE Transactions on Power Systems*, vol. 20, no. 4, pp. 1929-1937, Nov. 2005.

[16] J. Niiranen, "Voltage dip ride through of a double-fed generator equipped with an active crowbar," In *Nordic Wind Power Conference*, pp. xx-xx, Sweden, Mar. 2004.

[17] P. Zhou, "Control strategy of an active crowbar for DFIG based wind turbine under grid voltage dips," In *Proceedings of 2007 International Conference on Electrical Machines and Systems*, pp. 259-264, Korea, Oct. 2007.

[18] S. R. Kalantarian, "A new crowbar protection method for improvement in performance of doubly fed induction generator under fault conditions," In *Proceedings of the 10th International Conference on Environment and Electrical Engineering*, pp. 1-4, Iran, May 2011.

[19] J. Morren and S. W. H. de Haan, "Ride-through of wind turbines with doubly fed induction generator during a voltage dip," *IEEE Transactions on Energy Conversion*, vol. 20, no. 2, pp. 435-441, Jun. 2005.

[20] D. Xiang, L. Ran, P. J. Tavner, and S. Yang, "Control of a doubly fed induction generator in a wind turbine during grid fault ride-through," *IEEE Transactions on Energy Conversion*, vol. 21, no. 3, pp. 652-662, Sep. 2006.

[21] J. Yao, H. Li, Y. Liao, and Z. Chen, "An improved control strategy of limiting the DC-link voltage fluctuation for a doubly fed induction wind generator," *IEEE Transactions on Power Electronics*, vol. 23, no. 3, pp. 1205-1213, May 2008.

[22] M. Rahimi and M. Parniani, "Grid-fault ride-through analysis and control of wind turbines with doubly fed induction generators," *Electric Power Systems Research*, vol. 80, no. 2, pp. 184-195, Jun. 2010.

[23] D. Gautam, V. Vittal, T. Harbour, "Impact of increased penetration of DFIG-based wind turbine generators on transient and small signal stability of power systems," *IEEE Transactions on Power Systems*, vol. 24, no. 3, pp. 1426-1434, Aug. 2009.

[24] F. M. Hughes, O. A. Lara, N. Jenkins and G. Strbac, "Control of DFIG-based wind generation for power network support," *IEEE Transactions on Power Systems*, vol. 20, no. 4, pp. 1958-1966, Nov. 2005.

[25] F. M. Hughes, O. A. Lara, N. Jenkins and G. Strbac, "A power system stabilizer for DFIG-based wind generation," *IEEE Transactions on Power Systems*, vol. 21, no. 2, pp. 763-772, May 2006.

[26] R. D. Fernandez, P. E. Battaiotto and R. J. Mantz, "Wind farm nonlinear control for damping electromechanical oscillations of power systems," *Renewable Energy*, vol.33, no. 10, pp. 2258-2265, Oct. 2008.

[27] Y. Mishra, S. Mishra, M. Tripathy, N. Senroy and Z.Y. Dong, "Improving stability of a DFIG-based wind power system with tuned damping controller," *IEEE Transactions on Energy Conversion*, vol. 24, no. 3, pp. 650-660, Sep. 2009.

[28] W. E. Leithead and B. Connor, "Control of variable speed wind turbines: dynamic models," *International Journal of Control*, vol. 73, no. 13, pp. 1173-1188, Sep. 2000.

[29] J. Lopez, P. Sanchis, X. Roboam and L.Marroyo, "Wind turbines based on doubly fed induction generator under asymmetrical voltage dips," *IEEE Transactions on Energy Conversion*, vol. 23, no. 1, pp. 321-330, Mar. 2008.

[30] W. E. Leithead and B. Connor, "Control of variable speed wind turbines: design task," *International Journal of Control*, vol. 73, no. 13, pp. 1189-1212, Sep. 2000.

[31] E. B. Muhando, T. Senjyu, A. Uehara and T. Funabashi, "Gain-scheduled H-infinity control for WECS via LMI techniques and parametrically dependent feedback part I: Model development fundamentals," *IEEE Transactions on Industrial Electronics*, vol. 58, no. 1, pp. 48-56, Jan. 2011.

[32] E. B. Muhando, T. Senjyu, A. Uehara and T. Funabashi, "Gain-scheduled H-infinity control for WECS via LMI techniques and parametrically dependent feedback part II: Controller design and implementation," *IEEE Transactions on Industrial Electronics*, vol. 58, no. 1, pp. 57-65, Jan. 2011.

[33] E. B. Muhando, T. Senjyu, A. Uehara, T. Funabashi and C. H. Kim, " LQG design for megawatt-class WECS with DFIG based on functional models' fidelity prerequisites," *IEEE Transactions on Energy Conversion*, vol. 24, no. 4, pp. 893-904, Dec. 2009.

[34] F. Valenciaga, P. F. Puleston, P. E. Battaiotto and R. J. Mantz, "An adaptive feedback linearization strategy for variable speed wind energy conversion systems," *International Journal of Energy Research*, vol. 24, no. 2, pp. 151-161, Feb. 2000.

[35] J. M. Mauricio, A. E. Leon, A. Gomez-Exposito and J. A. Solsona, "An adaptive nonlinear controller for DFIM-based wind energy conversion system," *IEEE Transactions on Energy Conversion*, vol. 23, no. 4, pp. 1025-1035, Dec. 2008.

[36] F. Wu and X. P. Zhang, "Decentralized nonlinear control of wind turbine with doubly fed induction generator," *IEEE Transactions on Power Systems*, vol. 23, no. 2, pp. 613-621, May 2008.

[37] L. Holdsworth, X.Wu, J. B. Ekanayake and N.Jenkins, "Comparison of fixed speed and doubly-fed induction wind turbines during power system disturbances," *IEE Proceedings Generation Transmission and Distribution*, vol. 150, no. 3, pp. 342-352, May 2003.

[38] T. Ackermann, *Wind power in power systems*. John Wiley and sons, England, 2005.

[39] S. N. Bhadra, D. Kastha and S. Banerjee, *Wind Electrical Systems*. Oxford University Press, New Delhi, 2009.

[40] N. W. Miller, W. W. Price, and J. J. Sanchez-Gasca, "Dynamic modeling of GE 1.5 and 3.6 wind turbine-generators," *GE-Power Systems Energy Consulting, General Electric International, Inc.*, 2003.

[41] F. Mei and B. Pal, "Modal analysis of grid-connected doubly fed induction generators," *IEEE Transactions on Energy Conversion*, vol, 22, no. 3, pp. 728-736, Sep. 2007.

[42] J. P. A. Vieira, M. N. A. Nunes and U. H. Bezerra, "Design of optimal PI controllers for doubly fed induction generators in wind turbines using genetic algorithm," In *Proceedings of the 2008 IEEE Power and Energy Society General Meeting*, pp. 1-7, Pittsburgh, Jul. 2008,.

[43] W. Qiao, G. K. Venayagamoorthy and R. G. Harley, "Design of optimal control PI controllers for doubly fed induction generators driven by wind turbines using particle swarm optimization," In *International Joint Conference on Neural Networks*, pp. 1982-1987, Canada, Jul. 2006.

[44] S. M. B. Wilmshurst, "Control strategy for wind turbines," *Wind Eng.*, vol. 12, no. 4, pp. 236-250, 1988.

[45] X. P. Zhang, K. Godfrey and P. Ju, "Small signal stability analysis and optimal control of a wind turbine with doubly fed induction generator," *IET Generation, Transmission & Distribution*, vol. 1, no. 5, pp. 751-760, Sep. 2007.

[46] R. G. Almeida, J. A. Pecas Lopes and J. A. L. Barreiros, "Improving power system dynamic behavior through doubly fed induction machines controlled by static converter using fuzzy control," *IEEE Transactions Power Systems*, vol. 19, no. 4, pp. 1942-1950, Nov. 2004.

[47] Z. Song, T. Shi, C. Xia and W. Chen, "A novel adaptive control scheme for dynamic performance improvement of DFIG-Based wind turbines," *Energy*, vol. 38, no. 1, pp. 104-117, Feb. 2012.

[48] L. Jiang, Q. H. Wu, G. P. Liu and D. Rees, "Robust adaptive control of induction motor based on perturbation observer," In *IEEE Electrical Machine and Drives Conference 2007*, vol. 1, pp. 101-106, Turkey, May 2007.

[49] B. Beltran, M. E. Benbouzid and T. Ahmed-Ali, "Second-order sliding mode control of a doubly fed induction generator driven wind turbine," *IEEE Transactions on Energy Conversion*, vol. 27, no. 2, pp. 261-269, Jun. 2012.

[50] R. Marino, S. Peresada and P. Valigi, "Adaptive input-output linearising control of induction motor," *IEEE Transactions on Automatic Control*, vol. 38, no. 2, pp. 208-221, Feb. 1993.

[51] F. K. A. Lima, A. Luna, P. Rodriguez, E. H. Watanabe and F. Blaabjerg, "Rotor voltage dynamic in the doubly fed induction generator during grid faults," *IEEE Transactions on Power Electronics*, vol. 25, no. 1, pp. 118-130, Jan. 2010.

[52] A. Tapia, G. Tapia, J. Ostolaza, , and J. S*á*enz, "Modeling and control of a wind turbine driven doubly fed induction generator," *IEEE Transactions on Energy Conversion*, vol. 18, no. 2, pp. 194-204, Jun. 2003.

[53] B. Chowdhury and S. Chellapilla, "Double-fed induction generator control for variable speed wind power generation," *Electric Power Systems Research*, vol. 76, no. 9, pp. 786-800, Jun. 2006.

[54] N. Mohan, T. Undeland, and W. Robbins, *Power electronics. Converters, applications and design*, 3rd ed. John Wiley and Sons, Inc., 2003.

[55] B. Bose, *Power electronics and ac drives*. Englewood Cliffs, New Jersey: Prentice-Hall, 1986.

[56] L. Chang, R. Doraiswami, T. Boutot, and H. Kojabadi, "Development of a wind turbine simulator for wind energy conversion systems," in *Canadian Conference on Electrical and Computer Engineering*, vol. 1, pp. 550-554, Mar. 2000.

[57] S. Bolik, "Modelling and analysis of variable speed wind turbines with induction generator during grid fault," PhD Thesis, Aalborg University, Aalborg, Denmark, Oct. 2004.

[58] A. Hansen and G. Michalke, "Voltage grid support of DFIG wind turbines during grid faults," in *Proc. European Wind Energy Conference and Exhibition 2007 (EWEC 2007)*, Milan, Italy, May. 2007.

[59] E. Tremblay, A. Chandra, and P. Lagace, "Grid-side converter control of D-FIG wind turbines to enhance power quality of distribution network," in *IEEE Power Engineering Society General Meeting*, pp. 6, Jun. 2006.

[60] V. Akhmatov, "Modelling of variable speed wind turbines with doubly-fed induc tion generators in short-term stability investigations," in *Proc. of International Workshop on Transmission networks for Offshore Wind Farms*, Stockholm, Sweden, Apr. 2002.

[61] J. Smajo, "Rotor power feedback control of wind turbine system with doubly-fed induction generator," in *Proceedings of the 6th WSEAS International Conference on Simulation, Modelling and Optimization*, pp. 48-53, Spain, 2006.

[62] S.H Li, R. Challoo, "Comparative study of DFIG power control using stator-voltage and stator-flux oriented frames," *2009 IEEE Power and Energy Society General Meeting, PES '09*, July 2009.

[63] L. Morel, H. Godfroid, A. Mirzaian, J.M. Kauffmann, "Double-fed induction machine: converter optimization and field oriented control without position sensor," *IEE Proceedings: Electric Power Applications*, vol. 145, no. 4, pp. 360-368, July 1998.

[64] B. Hopfensperger, D. Atkinson, and R. A. Lakin, "Stator flux oriented control of a cascaded doubly-fed induction machine," *IEE Proceedings: Electric Power Applications*, vol. 146, no. 6, pp. 597C605, Nov. 1999.

[65] P. C. Krause, O. Wasynczuk, S. D. Sudhoff, *Analysis of electric machinery and drive systems*, A John Wiley and Sons, UK, 2002.

[66] A. Arash, P. Mojtaba, M. Ali, "Analyzing vector control of a grid-connected DFIG under simultaneous changes of two inputs of control system," *European Journal of Scientific Research*, vol.45, no.2 , pp.221-231, 2010.

[67] H. Li, Z. Chen, "Overview of different wind generator systems and their comparisons," *IET Renew. Power Gen.*, vol. 2, no. 2, pp. 123-l38, 2008.

[68] S. Soter, R. Wegener, "Development of induction machines in wind power technology," *IEEE Intel. Elec. Mach. And Drives Conf*, pp. 1490-1495, 2007.

[69] J.A. Baroudi, V. Dinavahi, A.M. Knight, "A review of power converter topologies for wind generators," *IEEE International Conference on Electric Machines and Drives*, pp. 458-465, 2005.

[70] L.M. Fernandez, C.A. Garcia, F. Jurado, et aI., "Control system of doubly fed induction generators based wind turbines with production limits," *IEEE Intel. Conf. Electic. Mach. and Drives*, pp. 1936-1941, 2005.

[71] FA. Bhuiyan and A. Yazdani, "Multimode control of a DFIG-Based wind-power unit for remote applications," *IEEE Trans. Power Del.*, vol. 24, no. 4, pp. 2079-2089, Oct. 2009.

[72] X. Yuan, F Wang, D. Boroyevich, et aI., "DC-link voltage control of a full power converter for wind generator operating in weak-grid systems," *IEEE Trans. Power Electr.*, vol. 24, no. 9, pp. 2178-2192, 2009.

[73] L. Yang, G.Y. Yang, Z. Xu, et aI., "Optimal controller design of a doubly-fed induction generator wind turbine system for small signal stability enhancement," *IET Generation, Transmission and Distribution*, vol. 4, no. 5, pp. 579-597, 2010.

[74] L. Sun, Z. Mi, Y. Yu, et. aI., "Active power and reactive power regulation capacity study of DFIG wind turbine," *Inter. Conf. Sustain. Power Gen. Supply*, pp. 1-6, 2009.

[75] B. Shen, B. Mwinyiwiwa, Y. Zhang, et. aI., "Sensorless maximum power point tracking of wind by DFIG using rotor position phase lock loop," *IEEE Trans. Power Elec.*, vol. 24, no. 4, pp. 942-951, 2009.

[76] P. KUNDUR, *Power System Stability and Control*, Mc Graw Hill, 1994.

[77] M. Fei and B. Pal, "Modelling of doubly-fed induction generator for power system stability study," *Power and Energy Society General Meeting - Conversion and Delivery of Electrical Energy in the 21st Century*, pp. 1-8, Jul. 2008.

[78] R. Datta, VT. Ranganathan, "A simple position sensorless algorithm for rotor side field oriented control of wound rotor induction machine," *IEEE Transactions on Industrial Electronics*, vol. 48, no. 4, pp. 786-793, 2001.

[79] P. Ledesma, J. Usaola, "Doubly fed induction generator model for transient stability analysis," *IEEE Transactions on Energy Conversion*, vol. 20, no. 2, pp. 388-397, 2005.

[80] K. Tan, S. Islam, "Mechanical sensorless robust control of wind turbine driven permanent magnet synchronous generator for maximum power operation," *International Journal of Renewable Energy Engineering*, vol. 3, no. 2, pp. 379-384, 2001.

[81] B. Boukhezzar, H. Siguerdidjane, "Nonlinear control with wind estimation of a DFIG variable speed wind turbine for power capture optimization", *Energy Conversion and Management*, vol.50, no.4, pp. 885-892, April. 2009.

[82] A. Kumar, K. Stol, "Simulating Feedback Linearization control of wind turbines using high-order models", *Wind Energy*, vol. 13, no. 5, pp. 419-432, July 2010.

[83] A.F. Payam, B.M. Dehkordi, M. Moallem, "Adaptive input-output feedback linearization controller for doubly-fed induction machine drive", *International Aegean Conference on Electrical Machines and Power Electronics, 2007. ACEMP '07.*, pp. 830-835, Sep. 2007.

[84] W. Qiao, W. Zhou, J. M. Aller and R. G. Harley, "Wind speed estimation based sensorless output maximization control for a wind turbine driving a DFIG", *IEEE Trans. on Power Electronics*, vol. 23, pp. 1156-1169, 2008.

[85] A. F. Payam, "An adaptive input-output feedback linearization controller for doubly-fed induction machine drives," *Serbian Journal of Electrical Engineering*, vol. 5, no. 1, pp. 139-154, May 2008.

[86] L. Jiang, Q. H. Wu and J. Y. Wen, "Decentralized Nonlinear Adaptive Control for Multimachine Power Systems Via High-Gain Perturbation Observer", *IEEE Trans. on Circuits and Systems I: Regular Papers*, vol. 51, pp. 2052-2059, 2004.

[87] L.Jiang, Q.H. Wu "Observer-based nonlinear control of synchronous generator with perturbation estimation", *International Journal of Electrical Power and Energy Systems*, vol. 23, pp. 359-367, June, 2001.

[88] J. Carrasco, L. Franquelo, J. Bialasiewicz, E. Galvan, R. Guisado, M. Prats, J. Leon and N. Moreno-Alfons, "Power-electronic systems for the grid integration of renewable energy sources: A survey," *IEEE Transactions on Industrial Electronics*, vol. 53, no. 4, pp. 1002-1016, Aug. 2006.

[89] J. Arbi, M.-B. Ghorbal, I. Slama-Belkhodja, and L. Charaabi, "Direct virtual torque control for doubly fed induction generator grid connection," *IEEE Transactions on Industrial Electronics*, vol. 56, no. 10, pp. 4163-4173, Oct. 2009.

[90] B. Rabelo, W. Hofmann, J. da Silva, R. de Oliveira and S. Silva, "Reactive power control design in doubly fed induction generators for wind turbines," *IEEE Transactions on Industrial Electronics*, vol. 56, no. 10, pp. 4154-4162, Oct. 2009.

[91] S. Shao, E. Abdi, F. Barati and R. McMahon, "Stator-flux-oriented vector control for brushless doubly fed induction generator," *IEEE Transactions on Industrial Electronics*, vol. 56, no. 10, pp. 4220-4228, Oct. 2009.

[92] J. Niiranen, "Voltage dip ride through of doubly-fed generator equipped with active crowbar," presented at the Nordic Wind Power Conf., G*ö*teborg, Sweden, Mar. 1-2, 2004 [Online]. Available:

http://www.elteknik.chalmers.se/Publikationer/EMKE.publ/NWPCO4/papers/NIRRANEN.pdf, Chalmers Univ. Technol.

[93] K. Rothenhagen and F. Fuchs, "Current sensor fault detection, isolation, and reconfiguration for doubly fed induction generators," *IEEE Transactions on Industrial Electronics*, vol. 56, no. 10, pp. 4239-4245, 2009.

[94] J. Lopez, E. Gubia, E. Olea, J. Ruiz and L. Marroyo, "Ride through of wind turbines with doubly fed induction generator under symmetrical voltage dips," *IEEE Transactions on Industrial Electronics*, vol. 56, no. 10, pp. 4246-4254, Oct. 2009.

[95] R. Fadaeinedjad, G. Moschopoulos and M. Moallem, "Voltage sag impact on wind turbine tower vibration," *Proc. IEEE Power Eng. Soc. Gen. Meeting*, pp. 1-8, 2007

[96] S. Papathanassiou and M. Papadopoulos, "Mechanical stresses in fixed-speed wind turbines due to network disturbances," *IEEE Transactions on Energy Conversion*, vol. 16, no. 4, pp. 361-367, 2001.

[97] I. Canay, "Calculation of negative-sequence losses and negativesequence resistance of turbogenerators," *IEEE Transactions on Power Apparatus and Systems*, vol. PAS-94, no. 3, pp. 764-773, May-Jun. 1975.

[98] A. Petersson, L. Harnefors and T. Thiringer, "Modeling and experimental verification of grid interaction of a DFIG wind turbine," *IEEE Transactions on Energy Conversion*, vol. 20, no. 4, pp. 878-886, Dec. 2005.

[99] T. Brekken and N. Mohan, "A novel doubly-fed induction wind generator control scheme for reactive power control and torque pulsation compensation under unbalanced grid voltage conditions," *Proc. IEEE 34th Annu. Power Electron. Spec. Conf.*, vol. 2, pp. 760-764, 2003.

[100] L. Shi, S. Dai, Y. Ni, L. Yao, and M. Bazargan, "Transient stability of power systems with high penetration of DFIG based wind farms," *Proc. IEEE Power Electron. Spec. Gen. Meeting*, pp. 1-6, 2009.

[101] R. Cardenas, R. Pena, G. Tobar, J. Clare, P. Wheeler, and G. Asher, "Stability analysis of a wind energy conversion system based on a doubly fed induction generator fed by a matrix converter," *IEEE Transactions on Industrial Electronics*, vol. 56, no. 10, pp. 4194-4206, 2009.

[102] Y. Wang and L. Xu, "Control of DFIG based wind generation systems under unbalanced network supply," *IEEE International Electric Machines and Drives Conference (IEMDC 2007)*, pp. 430-435, 2007.

[103] L. Xu, "Coordinated control of DFIG's rotor and grid side converters during network unbalance," *IEEE Transactions on Industrial Electronics*, vol. 23, no. 3, pp. 1041-1049, May 2008.

[104] G. Abad, "Direct power control of doubly-fed-induction-generator-based wind turbines under unbalanced grid voltage," *IEEE Transactions on Power Electronics*, vol. 25, no. 2, pp. 442-452, Feb. 2010.

[105] J. P. da Costa, J. R. Massing, and H. Pinheiro, "Control of doubly fed induction generator during disturbances in the grid: Crowbar active and reactive support," *Proc. XVII Brazilian Conf. Automatica*, pp. 1-7, 2008.

[106] A. Luna, F. K. A. Lima, P. Rodriguez, E. H. Watanabe and R. Teodorescu, "Comparison of power control strategies for DFIG wind turbines," *Proc. 34th IEEE IECON*, pp. 2131C2136, 2008.

[107] S. Karimi, A. Gaillard, P. Poure, and S. Saadate, "FPGA-based real-time power converter failure diagnosis for wind energy conversion systems," *IEEE Transactions on Industrial Electronics*, vol. 55, no. 12, pp. 4299-4308, 2008.